



INTERNATIONAL ATOMIC ENERGY AGENCY
UNITED NATIONS EDUCATIONAL, SCIENTIFIC AND CULTURAL ORGANIZATION
INTERNATIONAL CENTRE FOR THEORETICAL PHYSICS
I.C.T.P., P.O. BOX 586, 34100 TRIESTE, ITALY, CABLE: CENTRATOM TRIESTE



INTERNATIONAL
COMMITTEE FOR
FUTURE ACCELERATORS

ISTITUTO
NAZIONALE
DI FISICA NUCLEARE **INFN**

H4.SMR. 394/4

SECOND ICFA SCHOOL ON INSTRUMENTATION IN
ELEMENTARY PARTICLE PHYSICS

12- 23 JUNE 1989

Detectors for Astroparticle Physics

G.L. CASSIDAY

University of Utah, Salt Lake City, U.S.A.

These notes are intended for internal distribution only.

1 INTRODUCTION

1.1 Description of Problem

The primary reason for the explosion of experimental activity in the VHE (very high energy; $1 \text{ TeV} < E < 1 \text{ PeV}$) and to a lesser extent the UHE (ultra high energy; $1 \text{ PeV} < E < 1 \text{ EeV}$) and EHE (extremely high energy; $E > 1 \text{ EeV}$) regions stems from recent hints¹ that naturally occurring particle accelerators exist in our galaxy. Such reports, coming at a time when man-made accelerators and the opportunities to carry out accelerator experiments are suffering a decline in numbers, have quite naturally engendered excitement throughout the high energy physics community. The recent flurry of activity is thus seen as a logical and desirable infusion of energetic blood into a hitherto somewhat laconic field of endeavor. The fundamental goal of astroparticle physics has been, since their time of discovery by Victor Hess² in 1912, to discover the sources of these particles. Much has been learned about their nature since that time but the fundamental mystery still remains, particularly for astroparticles of the highest energies. These lectures will focus primarily on the techniques commonly invoked to address this problem, namely the unmasking of the sources of these extremely energetic astrophysical sources as well as the mechanism by which these sources manage to accelerate particles to such high energies.

Extensive air showers (EAS), those great cascades of particles spreading over more than 10^5 m^2 or more at ground level, were first discovered back in 1927 by Skobel'tzyn³ and soon it was realized that they were initiated by the interaction in the upper atmosphere of individual particles carrying prodigious energies. Indeed, by 1963 it was realized⁴ that some of these EAS might be due to single astroparticles carrying as much energy as 100 EeV or about 16 Joules! Most of these particles are charged bare nuclei ranging from protons up to iron nuclei and perhaps heavier. The exact percentages of these primaries is not known at energies exceeding about 100 TeV. If most of the astroparticles were neutral then location of the sources could be carried out quite simply in a fashion analogous to conventional astronomy, namely just look with a "telescope". More remote sources could be seen simply by building another telescope with larger "gathering power". Unfortunately, the fact that most of the particles are charged means that they get all scrambled up within the galaxy's magnetic field on their way to earth. Hence, their source direction is almost entirely lost. Luckily though there are some neutral particles present in the astroparticle flux and the trick for locating sources becomes one of primarily sharpening one's angular resolution and increasing detector size such that the directly beamed neutrals stand out above the isotropically distributed "charged" noise. The situation is quite analogous to attempts to see astronomical sources during the daytime. The sun is obvious because it's such a strong source. However, it lights up the sky and creates an almost isotropic photon backdrop in all other viewing directions. The moon is sometimes directly visible even in the presence of this backdrop but our view of planets and stars is completely obliterated. The use of a telescope will allow us to see some planets and stars even in daytime by eliminating most of this background flux. A view of ever dimmer

and dimmer stars however requires the use of even larger and larger aperture telescopes with finer and finer angular resolution. This, in a nutshell, is the fundamental problem facing experimenters wishing to locate astroparticle sources on the celestial sphere. Neutral particles coming directly from those sources are bathed in a sea of isotropic charged particle background.

1.2 Astroparticle Sources

Very general arguments can be made which severely limit one's choices of possible sites for acceleration of astroparticles particularly for those with energies approaching 100 EeV.⁵ Sites which have been proposed include supernovae, supernovae remnants, giant molecular clouds, binary x-ray systems, sporadic explosive events in the galactic center,⁶ galactic wind shocks,⁷ active galactic nuclei, and sites of colliding galaxies.⁸ Essentially, the sites must be large enough to house the accelerator and the acceleration process must operate over a short enough time scale to overcome energy losses. Almost all acceleration models (statistical acceleration such as Fermi or shock wave varieties --- or direct acceleration by e&m fields generated by rapidly rotating neutron stars etc.) lead to the requirement that the size L should obey the inequality

$$L > 2R_L/B$$

where R_L , the Larmor radius of a particle of charge ze in a magnetic field B , is

$$R_L(\text{pc}) = 1.08 E(\text{PeV})/B(\text{uG})z$$

and B_c is the characteristic velocity of scattering centers or the moving field elements which are responsible for the acceleration. This inequality arises either from the requirement on the space occupied by the diffusive spread of the particles during statistical acceleration or from the physical extent of the field necessary to generate the potential difference in direct acceleration mechanisms. The size requirement can thus be written as

$$L(\text{pc}) > 2 E(\text{PeV})/(B(\text{uG}) \cdot z \cdot B)$$

Figure 1 shows a number of potential acceleration sites plotted according to their estimated sizes and probable field strengths. Each diagonal line corresponds to a proton of the quoted energy and an object must be above a particular diagonal line for it to have any hope of accelerating a particle to that energy. The shaded band for a 100 EeV proton represents the size and/or field variation encompassed by the velocity range 1000 km/s (appropriate for non-relativistic shocks; top of band) to 300,000 km/s (for relativistic shocks or field lines tied to a rapidly rotating neutron star; the bottom of the band). Lesser energy particles are represented by similar bands but only the lower one is shown. Note also that bands for, say, iron nuclei would be about 26 times lower for each energy. We can easily see that all of these objects could potentially accelerate VHE and UHE astroparticles but there are only a few candidates for EHE ($E > 1 \text{ EeV}$) acceleration.

A simple consideration of observed energetics also leads us to conclude that many of the sources listed above can be considered as possible candidates for astroparticle acceleration. The local energy density of cosmic rays (1 eV cm^{-3}) is almost identical to that of starlight, galactic magnetic fields and gas motion. The similarity to starlight is probably fortuitous but the other near coincidences have been considered by some to indicate local acceleration and thus, that the bulk of the astroparticles are of galactic origin. For example, the energy input in the form of astroparticles from supernovae is estimated to be about 10^{41}

ergs/s very similar to the energy input of between $3 \cdot 10^{40}$ and $6 \cdot 10^{41}$ ergs/s required to maintain the local astroparticle energy density. Moreover, collapsing molecular clouds, pulsars, binary x-ray systems as well as periodic explosions in our galactic center every 10^7 years give about this same value. However, it must be admitted that, since the energy density of the $2.7 \text{ }^\circ\text{K}$ blackbody radiation, of extragalactic origin also has an energy density close to that of the locally observed astroparticles, simple energy arguments do not lead to the unequivocal conclusion that the bulk of the observed high energy astroparticles are galactic objects. Nonetheless, the existence of naturally occurring objects in our own galaxy possessing conditions possible for the "construction" of accelerators capable of boosting particles up to 1 PeV and possibly even about 10 EeV leads us to focus our attention there first before attempting to investigate potentially more powerful albeit more remote systems.

1.3 Binary X-Ray Systems

Out of all the possible sources listed above, most recent detection effort has been devoted to binary x-ray systems such as Cygnus X-3 or Hercules X-1. The reason for such emphasis is straightforward; such systems exhibit periodic behavior which can be exploited in order to enhance detection signal to noise ratios. And since most existing astroparticle detectors operating in the TeV energy region or above are doing so at their limits of sensitivity to purely directional signals, existence of periodicity is an absolute necessity if one is to have any hope at all of obtaining a positive signal. In fact, many physicists believe that even after invoking periodicity, all previously reported positive observations are basically artifacts of detector systems whose sensitivity limits have been pushed to the utmost. Be that as it may, here we will discuss the characteristics of such systems since we believe that they are the ones whose unequivocal positive detection is most likely to be made by the newer astroparticle installations currently under construction.

The system we choose to discuss is Hercules X-1 for a variety of reasons. (1) It has been one of the most extensively studied systems at a wide variety of wavelengths since its discovery in the x-ray region in 1972 with the Uhuru satellite.⁹ (2) The presence of an accretion disk is problematical for most binary systems, but it is almost a certainty in the case of Her X-1 for which many intricate details are known about its time variations in both the optical and x-ray regions. (3) Moreover, many positive detections at energies up to about 1 PeV have been reported.¹⁰ Shown in figure 2 is the 1st observation of X-ray pulsation detected from Her X-1. Its period at that epoch was measured to be $1.2368 \pm 0.0006 \text{ sec}$. It was also found that this pulsation exhibited a periodically repeating set of

two gross intensity states separated by sharp transitions, a high state during which the source was "on" and a low state during which it was essentially "off". The implication was that the rapidly pulsating source was a member of a binary system which was occulted once every 1.7 days by its companion. This conclusion was greatly strengthened by the observation of sinusoidal variations of the pulsation period with the same 1.7 day period, precisely the sort of observation that one would get if the x-ray pulses were doppler shifted according to orbital phase. Shown in figure 3 is a phasing analysis of 3 days of data in Jan, 1972. Also shown is the sine function fit to the data. Note, that the zeros of the period variation correspond precisely with the centers of the highs and lows of the intensity variation, again exactly what we would expect if the pulsations at that time corresponded to the source being directly in front of and behind the occulting companion star. If we assume that the observed arrival time differences of the x-ray pulses are due to orbital motions of the source, the amplitude of the sine curve corresponds to a projected radius of the orbit of $13.19 \pm 0.03 \text{ light seconds}$. The projected velocity computed for this radius using a period of 1.700 days is $169.2 \pm 0.4 \text{ km/s}$. These values imply that what we are dealing with here is a close binary system in which matter from the companion star fills its Roche lobe and is spilling over onto the surface of a 1.24 second spinning neutron star. The matter crashing down to the surface of the neutron star is probably generating the x-rays.

Evidence for the existence of an accretion disk is based on several different types of observations. Further x-ray data for Hercules X-1 from Uhuru¹¹ indicate that the main 1.24 sec pulsation period decreases with time at the rate of about $4 \text{ } \mu\text{sec/yr}$. However, this spin up rate suffers frequent glitches and is slowing down. Such is the case for a rapidly spinning neutron star being fed angular momentum from a dynamic accretion disk. Further evidence is depicted in figure 4 which shows that the x-ray intensity turns on, builds up and slowly dies out during a 11-12 day ON state followed by about 23 to 24 days of inactivity at which point the cycle more or less repeats. The mechanism responsible for this variation is probably an accretion disk which precesses about the Her X-1 neutron star with a period of $34.88 \pm 0.12 \text{ days}$. This point of view was adopted after the discovery¹² of optical brightness variations in HZ Herculis, the optical companion of Her X-1. The B light curve (amplitude $\sim 1.5 \text{ mag}$) shows a single minimum per 1.7 day orbital cycle. B-V and U-B are also variable with amplitudes ~ 0.3 and 1.0 magnitudes respectively, the star being bluest when the x-ray source is in front of it. The optical variability is mainly due to x-ray heating of its surface. This also causes its spectral class to change with a 1.7 day period. In spite of the large variation of the x-ray flux over the above 35 day period, the optical brightness averaged over an orbital cycle changes only a little. Also, a feature is present in the light curve which drifts continuously toward earlier orbital phase throughout the 35 day on-off cycle, reappearing at the same orbital phase one on-off cycle later. These variations can best be explained by the presence of a tilted accretion disk acting also as a source of optical radiation, which gives variable shielding of the x-ray source, and occults part of the x-ray heated surface of the companion star.

In addition to the 1.24 sec pulsation period, itself, evidence that the primary star is a neutron star come from using the orbital

parameters of the system to determine its mass function and the spectral data and optical pulsations of HZ Herculis. The result is that the companion's mass is $2.35 \pm 0.20 - 0.40 M_{\odot}$ while that of Her X-1 is $1.45 \pm 0.25 - 0.40 M_{\odot}$. This mass is strongly suggestive of a neutron star. Also, in 1976, the Tübingen group¹² observed a strong x-ray peak at 58 KeV as well as a possible 2nd one at about 110 KeV for Her X-1. This corresponds precisely to an electron cyclotron resonance (and its 2nd harmonic) in a magnetic field of $5 \cdot 10^{12}$ Gauss the value expected for electrons spirally down onto the magnetic pole of a neutron star.

The above description, I hope, gives some flavor of the enormous amount of x-ray and observational data that have been accumulated for the Her X-1 system and how that data leads to a very convincing self-consistent model for Her X-1 as a low mass, close x-ray binary system in which the rapidly rotating neutron star possesses a large magnetic field and is fed by a dynamic accretion disk. Shown in figure 5 is an artist's conception of this model. Verification that objects in nature such as this also behave as extremely energetic particle accelerators is one of the primary goals of high energy astroparticle physics.

2 HIGH ENERGY GAMMA RAYS

Many advances in astronomy have come as a result of the development of a new generation of detectors. An order of magnitude increase in sensitivity is usually enough to reveal a multitude of new sources. Most dramatic advances, however, have not come by merely "scaling up" existing detectors. Instead, completely unsuspected phenomena have occurred with the advent of detectors capable of exploiting a hitherto unexplored region of the frequency spectrum, for example, the radio, infra-red and x-ray regions as opposed to the visible. Such has not been the case for high energy gamma ray astronomy probably because past and existing detectors have lacked the necessary sensitivity and probably because most (if not all) of the potential high energy astroparticle sources are also either emitters in one of the previously explored regions. In other words, the high energy astroparticle generators are probably only a subset of sources already known. Nonetheless, one would clearly like to understand the mechanism by which they work.

Currently, most physicists believe that the sources, presumably detected so far in the very high energy regime, have been "seen" via high energy gamma rays. There are, however, some strange anomalies in that some of the reported detections have been via muons¹³, a process which seems to defy the conventional viewpoint that high energy gamma rays are the most likely astroparticles that could travel in straight lines from the source in question and thus be responsible for the detection. Here we will adopt the conventional viewpoint that gamma rays are the likely progenitors of high energy behavior except in the cases of extremely high energies where neutrons could in fact survive even galactic travel distances and thus carry information to the earth about galactic sources. Neutrinos could obviously work too and many groups are trying hard to exploit that particular detection possibility.¹⁴ The only positive neutrino detections of which I'm

aware are solar neutrinos¹⁵ and those from SN1987A.¹⁶⁻¹⁸ Here, we will neglect that activity (It's likely to require an experimenter of an extremely patient temperament) and focus, instead, on gamma rays.

The vertical atmosphere is about 1033 g cm^{-2} thick and the interaction length (radiation length) for a high energy gamma ray is about 38 g cm^{-2} while that of a high energy proton is about 70 g cm^{-2} . Consequently, the earth's atmosphere is opaque to "stable" high energy astroparticles (save neutrinos) which are likely to make it to earth from distant sources and thus it is an essential ingredient of any detector of high energy astroparticles. There are several ways in which an incident high energy astroparticle can be detected and all of them are indirect. (Up to about 100 TeV the isotropic hadron flux can be measured directly via balloons or satellites but the flux of gamma rays from any source is so small that this technique will not work) Roughly speaking, in the VHE energy region, the only known measurement technique exploits the use of Cherenkov light generated by the EAS initiated by the interaction of the primary particle in the upper atmosphere (or by detecting the muons in buried underground detectors, but muons are not supposed to be produced very efficiently by primary gamma rays). In this case the shower must strike within about 100-200 meters of the detector in order to be visible. In the UHE regime, the EAS is penetrating enough that many secondary electrons (and low energy muons from hadronic showers) strike the surface of the earth which thus opens up the possibility of another detection mechanism by an array of conventional particle detectors. Again, the shower must strike within 100 or so meters of a large number of particle detectors in order to register. Finally, in the EHE region, enough of the ionization energy liberated by the passage of EAS through the atmosphere appears in the form of scintillation light that such showers can be detected at distances up to 30 km away from an appropriate light receiver. For now, we will focus on the TeV regime where only the atmospheric Cherenkov technique can be employed.

2.1 The Extensive Air Shower (EAS)

A purely electromagnetic shower can be simply visualized in the following way. After each interaction length a photon disappears, creating an electron-positron pair which shares the energy about equally and each electron radiates about half its energy as a bremsstrahlung photon. The number of particles in the shower thus grows exponentially until the energy of each one on the average drops to the critical energy in air at which point ionization energy losses dominate radiative losses. Thereafter, the number of particles falls off exponentially. Clearly, this picture is a gross simplification of a real shower but it's not too far off the mark.

A hadronic shower is more complicated. A schematic is shown in figure 6. The first interaction is a hadron-air nucleus interaction which produces mostly pions and secondary nucleons. The nucleons continue on and undergo subsequent interactions, while the charged pions either decay to muons (if their energy is low enough, typically 10^5 to 100^5 of TeV in the earth's atmosphere) or also subsequently interact. For primaries in the VHE range, pion decay to muons tends to dominate. Clearly, the efficiency of this process is both energy and atmospheric density dependent. The neutral pions decay to gamma rays which initiate electromagnetic cascades. The hadronic shower can thus be

thought of as a shower which continually initiates small electromagnetic cascades.

In the UHE and EHE regime, the charged pions, due to their long lifetime, don't have a chance to decay into muons until the EAS has gone through many generations. Since each generation makes more neutral pions which immediately decay into gammas, a UHE or EHE hadron shower looks almost identical to a purely electromagnetic shower. However, a VHE hadronic shower has fewer electrons, is much more enriched with muons and is more penetrating than a comparable electromagnetic shower. In all energy regimes, the nucleonic core is not very useful for distinguishing primary gamma rays from hadrons. It is so compact that it has low probability of striking a ground-based. Shown in figure 7 are the lateral distributions of the non-hadronic components of a typical EAS. Note that Cherenkov light has the broadest lateral distribution (primarily due to multiple Coulomb scattering of the relativistic electrons producing the light) implying that larger active collecting areas are feasible as compared to detectors of the other components. Also note that muons are spread out more than electrons. This is because they are produced higher in the atmosphere, on the average. The difference in development of a hadronic and comparable electromagnetic shower is illustrated in figure 8.

Finally, note that electrons from showers with energy below about 100 TeV never make it to the ground. They are completely absorbed by the atmosphere. Thus, the use of ground based electron arrays to detect such showers is ruled out.

2.2 Gamma Ray-Hadronic Discriminators

There are several characteristics of gamma ray induced EAS which can be used to discriminate them from hadronic induced EAS. The first and most obvious is that gamma ray EAS point back toward the source while hadronic ones are isotropically distributed. Thus, decreasing angular resolution can be employed to eliminate more and more of the hadronic showers while preserving those due to gamma rays. A second characteristic that can be exploited is the difference in Cherenkov light image for the two types of showers.¹⁹ A third is the difference in UV light content.²⁰

Unfortunately, these differences are significant only for showers in the VHE regime. A fourth difference is a shower's muon content and since the muons spread out reasonably far from the shower's axis, this potential discriminant can be and is being exploited by a number of existing detectors as well as those under development. A final discriminant which has been used not terribly successfully in the past involves differences in electron lateral distribution and "age" of shower development. These latter techniques prove most useful for showers whose energies are in or above the UHE region. Other potential discriminants certainly exist but these are the ones which have been invoked and are the ones expected to be of greatest sensitivity.

3 THE ATMOSPHERIC CHERENKOV TECHNIQUE

3.1 Sensitivity

The index of refraction in air at sea level is 1.00029 so that the Cherenkov emission angle is about 1.3°. The angle decreases with altitude. The threshold energy is 21 MeV for electrons and 4.4 GeV for muons. The light yield in the spectral region 3500 - 5000 Å is about $8 \cdot 10^3$ per radiation length or about 30 photons m^{-1} at sea level. A 1 TeV shower produces an optical photon flux of about 50 photons m^{-2} within 100 m of the shower axis. The night sky photon background in the above spectral region is about 10^{12} photons $m^{-2} sr^{-1} s^{-1}$ and it is this light which creates the noise in photomultipliers with which the Cherenkov induced signal must compete. The Cherenkov pulse can be picked out of this noise basically because of its short duration, typically ~3-5 nsec. If the time constant of the detector is matched to this figure, Cherenkov light dominates the night sky. There is no known atmospheric or astrophysical background on these time scales, thus the ability to extract the weak Cherenkov pulse is limited only by noise fluctuations in an electronic sensor induced by the general night sky background. Assuming Poissonian fluctuations, the noise figure is

$$N \sim (e B A \Omega t)^{1/2}$$

where e is the efficiency for converting photons into cathode electrons (quantum efficiency, mirror reflectivity factors, etc), B is the background light intensity, A is the mirror area, Ω is the detector solid angle and t is the integration time. The signal is proportional $e A$ so that the signal to noise ratio is

$$S/N \sim (e A / B \Omega t)^{1/2}$$

The minimum detectable Cherenkov light pulse, hence the minimum detectable energy, is inversely proportional to this

$$Et \sim (B \Omega t / e A)^{1/2}$$

The minimum detectable flux sensitivity in terms of numbers of standard deviations can be determined by noting that

$$S_g = F_g A t \sim E_g^{-\Gamma} A t$$

where S_g is the number of gamma events detected within a fiducial area A during time t from a source whose flux is F_g (proportional to $E_g^{-\Gamma}$) and that

$$S_b = I(>E_b) A \Omega t / r \sim E_b^{-1.55} A \Omega t / r$$

where S_b is the number of cosmic ray background events detected within fiducial area A and solid angle Ω during observation time t due to the isotropic cosmic ray background intensity $I(>E_b)$ and *disguised as gamma ray events after surviving a cut made on the basis of a discriminating rejection factor r* . Also, note that in the VHE regime, $E_g \sim 0.3 E_b$ since electromagnetic cascades initiated by gammas produce Cherenkov light more efficiently than do those initiated by protons, the main source of the cosmic ray background. (In the UHE regime and above, $E_g \sim E_b$) Thus, the number of standard deviations of the detection is approximately

$$N_{sig} = F_g (r A t / I(>E) \Omega)^{1/2}$$

$$E^{0.8-\Gamma} (r A t / \pi)^{1/2} / \delta \theta$$

where we have assumed equality of the gamma ray and hadronic background energy thresholds, calling it simply E and where the solid angle has been written as $\Omega = \pi \cdot 60^2$ with 60 being the linear angular resolution. Note that for relatively flat gamma spectra ($\Gamma \sim 1$) the signal to noise figure is only weakly dependent on energy. Also, note that it is proportional to the root of the rejection factor r , the fiducial area A and the observation time t while it is inversely proportional to the angular resolution α . This can be a misleading for cases in which the gamma flux is not steady (or near steady) in time, ie, if it's sporadic. In that case, the fiducial area A has to be large enough to insure that the detector is not rate limited for a short burst low flux signal.

A useful figure of merit for comparing the sensitivities of various detectors over a very wide energy range is the energy flux $E \cdot F_g$. This figure is also useful for assessing how good a detector has to be in order to have a good likelihood of capturing a real gamma ray signal. F_g can be rewritten in terms of the signal to noise as

$$F_g = 60 \cdot N_{sig} \cdot (I(>E) \cdot \pi / r \cdot A \cdot t)^{1/2}$$

$$\text{hence} \quad \Sigma = E F_g = E \cdot 60 \cdot N_{sig} \cdot (I(>E) \cdot \pi / r \cdot A \cdot t)^{1/2}$$

and normalizing to 2 PeV where we note that

$$I(>E) = 10^{-10} \cdot (E/2 \text{ PeV})^{-6} \text{ cm}^{-2} \text{ sr}^{-1} \text{ s}^{-1}$$

with $\delta = 1.55 @ E < 2 \text{ PeV}$ and $\delta = 2.1 @ E > 2 \text{ PeV}$. Thus

$$\Sigma (\text{eV cm}^{-2} \text{ s}^{-1}) = 3 \cdot 10^{10} \cdot 60 \cdot N_{sig} \cdot E^{0.23} \cdot (r \cdot A \cdot t)^{-1/2}$$

For example, Cygnus X-3 has supposedly been detected over a very wide range of energies at about the 3-5 level at an energy flux value of about $100 \text{ eV cm}^{-2} \text{ s}^{-1}$. This implies that any new detectors should achieve an energy flux sensitivity of about $1-10 \text{ eV cm}^{-2} \text{ s}^{-1}$ if a convincing detection is the goal. As an example of this figure of merit for existing and typical PeV EAS arrays we have for the University of Utah array: $E \sim 0.5 \text{ PeV}$, $A \sim 3 \cdot 10^6 \text{ cm}^2$, $\alpha \sim 1^\circ$, $t \sim 90$ days (1 year on time) or $\Sigma = 46 \text{ eV cm}^{-2} \text{ s}^{-1}$ for a 5 detection. This is with no rejection factor cut applied ($r = 1$).

3.2 Rejection Factors for Cherenkov Detectors

The largest system expressly built for VHE gamma ray astronomy is the 10 m optical reflector at Whipple Observatory in Arizona (see figure 9).²⁰ It consists of an array of 248 hexagonal, spherically figured, mirror facets each with a focal length of 7.3 m. Each facet functions as an off-axis spherical mirror focusing light to the center of a 7.3 m sphere. Its point spread function is about 0.15° . The detecting elements consist of a 37 element array of hexagonal packed RCA 6342/V1 bialkali 5 cm photomultipliers mounted in the focal plane. The full aperture is 3.5° and the center of each tube is separated by 0.5° . The advantages of phototubes of other optical detecting elements are their combination of high gain and speed, as well as modularity and

high quantum efficiency at blue wavelengths. Note, that the Cherenkov emission spectrum scales as $(\text{wavelength})^{-2}$ although this is distorted by atmospheric attenuation particularly below 330 nm. Thus it is well suited to the use of bialkali tubes. Given the current estimates of the fineness of the differences between gamma ray and nucleon Cherenkov images the use of a "camera" with finer granularity is warranted.

Cherenkov light images have dimensions on the order of 1° to 2° . According to Monte Carlo calculations of Hillas²¹⁻²² the scale of structure within the image is on the order of several arc-minutes. For example, shown in figure 10 is the result of simulations for 320 GeV gamma ray and 1 TeV nucleon induced showers. (Remember, in this energy region, gamma EAS generate about 3 times more Cherenkov light than nucleon showers.) The differences in structure are clearly evident, the nucleon showers being more diffuse and exhibiting secondary maxima (in azimuthal strips) due to local muons. Shown in figure 11 are 4 gamma ray images due to 4 parallel, vertical showers striking the ground at 4 corners of a square centered on an optical detector 100 meters from each corner. Note how each image points directly toward the center of the detector. Clearly, if 2 detectors separated by about 100 meters were used to detect a single shower, this "pointing" could be used to both augment angular resolution as well as the gamma-hadron discrimination ability.

The Monte Carlo images predict (1) inherent differences in angular size and shape between the 2 classes of showers (an effect essentially due to differences in shower structure, eg, figure 8) and (2) differences in image orientation based upon point of shower origin (ie, on axis discrete source or isotropic background). Basically, the distribution of images from an on-axis source should appear to radiate from the center of the camera field of view (eg, figure 10) with the displacement of the image centroid and its "ellipticity" a function of the impact parameter between the shower and detector axes. Optimum discrimination between the gamma and hadronic showers utilizes a combination of these two types of differences (which are essentially independent).

The Whipple group has found that its most effective discriminator is a single parameter, the azimuthal width (abbreviated *azwidth*), which combines the size/shape and orientation criteria. This is a width measured perpendicular to the radius passing thru the shower image centroid. It is, in essence, a combination of the width of the image (rms extent along the image minor axis) and its miss (the distance in degrees by which the major axis of the image misses the center of the camera's field of view, ie, the location of the source being scanned). These parameters, along with their definitions, are schematically pictured in figure 12.

Hillas has carried out Monte-Carlo simulations using the Whipple detector properties which predict the distributions of the above listed parameters for both an on-axis gamma ray source as well as the isotropic hadronic background. The detector was assumed to point toward a source at zenith and its differential spectral index Γ was taken to be 2.25 while that of the background was 2.65. The results are shown in figure 13 for equal numbers of events. (In practice, the number of hadrons swamp the gamma rays by, perhaps, several orders of

magnitude!) Shown in figure 14 is a comparison of the background parameters with those actually measured by the detector during an off-source scan, ie, no known or suspected gamma source within the field of view. The agreement is good.

It would be nice, of course, to make a similar comparison for the on-source gamma induced showers. Unfortunately, no sufficiently strong source exists. Hence, the Whipple group has chosen cuts based completely on the simulations of the domain in which the gamma ray induced showers are expected to be. They thus do not try and optimize signal to noise by moving the cuts around after collecting their data.

As an example of an application of this technique, the Whipple group reports the following results for a scan of the crab pulsar.²³ During 210 pairs of on-source off-source scans from Dec. 1986 through Feb. 1988, they obtained an on-source total of 652,974 and an off-source total of 651,801 showers for an excess of +1173 during 81 2/3 hours of actual observation. This amounts to a 1.03 excess using the statistic of Li and Ma.²⁴ Applying an azimuth cut to both the on-source and off-source distributions, ie, selecting only events which are $< 0.35^\circ$ in the parameter azimuth, which should contain virtually all gamma showers and eliminate most hadronic ones, they obtain 9092 on-source and 7929 off-source showers for an excess of +1,163. This represents an 8.91 excess. Note that the rejection factor is about 80:1.

The overall distribution of the azimuth parameter is shown in figure 15. The small insert shows the on-off difference in detail for azimuth $< 0.35^\circ$. In fact there is pretty good agreement between this distribution and that of the simulations. Finally, shown in figure 16 is the distribution of on-off azimuth differences in terms of standard deviations. It appears as though the signal is indeed at small azimuth as expected for gamma induced EAS.

It should be mentioned that, in order to decrease angular resolution, the Whipple group has recently installed a 109 element photomultiplier array at the focal plane of their telescope with 91 of them consisting of 29 mm diameter tubes hexagonal close packed in a 1.25 degree/tube full fov and surrounded by 18 of their 5 cm tubes. They now report a 5 DC excess from the Crab which turns into a 15 excess upon application of the azimuth cut. This preliminary result was reported at the May, Arkansas Gamma Ray Conference.²⁵

3.3 Problems

As discussed earlier, gamma showers in the TeV range should be more compact than hadronic showers --- shorter and narrower. The Cherenkov shower images should reflect this as was apparently demonstrated by the Whipple observation of the Crab nebula. However, these features have not been found in the Whipple observatory images of showers from either Her X-1 or 4U0115+63 even though images of background hadronic showers have size distributions very close to predictions. Showers from these sources look very similar to hadronic showers. This result is not understood at this time.

4 UHE TECHNIQUES

UHE Gamma Ray Astronomy permits the use of techniques other than that of the atmospheric Cherenkov technique because of the more penetrating nature of the EAS, ie, their secondaries strike the ground in sufficient particle density that ground based detectors deployed rather sparsely over a sizeable area have a significant chance of being struck. This opens up the possibility of sensing both the electron and muon component of the EAS.

4.1 The Utah-Michigan-Chicago EAS Facility

The most extensive and sensitive facility currently under construction is that being assembled at Dugway, Utah by the Universities of Chicago and Michigan which will operate in concert with the existing University of Utah Fly's Eye detectors, tracking Cherenkov telescopes and ground based electron array. The final installation as currently envisioned is shown in figure 17. This facility is capable of measuring the electron, muon (muon energy > 1 GeV) and Cherenkov components of an EAS at a joint threshold in excess of about 300 TeV with an angular resolution of about 0.7° . The CASA electron sampling density is about 1/200 which makes it the largest, most dense electron array in the world. It is this feature plus its attention to fast timing that gives it its outstanding angular resolution capability, unprecedented in the PeV region. The muon array presents an active area of 2048 m² making it the largest (by more than an order of magnitude) such array in existence. It is this feature which gives the facility its outstanding hadronic shower rejection ratio (ranging from 100:1 for small showers, $E \sim 300$ TeV, to in excess of 1000:1 for large showers, $E > 1$ PeV). The tracking Cherenkov telescope system has an energy threshold of 50 TeV, a full fov of about 6° and an angular resolution of about 0.7° but can only view selected targets within its fov. The Fly's Eye II detector, in Cherenkov mode, has an energy threshold of about 100 TeV, an angular resolution $\delta\theta$ of about 3.5° but it views the entire sky and, thus, is useful for measuring event energies ($\pm 20\%$).

4.2 The CASA Array

4.2.1 Shower Calculations

The CASA array was designed from the start with the goal in mind of optimizing angular resolution for gamma showers. The Chicago group adopted an electromagnet shower program written by Pierre Darriulat at CERN in order to ascertain the required optimized design criteria. The program follows all electrons and photons with energies > 2 MeV and moving at angles $< 45^\circ$ relative to the incident primary. It ignores bremsstrahlung for electrons below the critical energy where only ionization loss and multiple scattering are included. The bremsstrahlung energy loss is approximated by $dN/dE \sim E^{-1}$ and, in pair production, the energy division is assumed uniform. Comptons follow the Klein-Nishina formula. An exponential atmosphere with a 7 km scale height is assumed. Electrons and photons having less than a 1% chance of producing an electron on the ground at Dugway (850 g cm^{-2}) are ignored. These approximations speed up computer time and have only minimal effects on the results.

These calculations have been used in several ways. First, the shower lateral distribution was calculated to estimate particle numbers in

the detectors, etc. Secondly, and more importantly, the time of arrival distribution of electrons in the shower was calculated. This information is most crucial for determining detector angular resolution.

Shown in figure 18 is the calculated distribution of the number of electrons striking the ground for vertical showers of 100 TeV. The fluctuations are large and demonstrates the difficulty of measuring primary energy by an electron size measurement. (Note, in a sparse array, the size measurement itself may exhibit large error.) $\langle N_e \rangle = 2.7 \cdot 10^4$ and $\langle N_e \rangle = 1.1 \cdot 10^4$. Clearly, the existence of the Fly's Eye detector greatly aids this measurement. The average size agrees well with the result of Snyder.²⁶

Shown in figure 19 is the calculated lateral distribution which is compared with the NKG calculation.²⁷ Agreement is not perfect but the deviations do not effect estimates of angular resolution.

The motion of every particle striking the ground relative to a particle travelling at the speed of light along the core is traced as a function of distance from the core. Figure 20 shows the particle density ($m^{-2} \text{ nsec}^{-1}$) vs arrival time delay parameterized by core distance. Particle delays are characterized by a very sharp front, particularly within 15m of the core. In no way is the distribution Gaussian or Poissonian. Thus, arguments of angular resolution limitations based on either such assumption is likely to be fallacious. This result suggests that it is desirable to simply use leading edge electronics and to insure that enough area is covered that most hits are due to the earliest particles in order to accurately measure shower direction.

4.2.2 Estimation of Angular Resolution

Each station of the 1000 station array of CASA detectors consists of 4 scintillation counters of 0.37 m² each making a total area of 1.48 m²/station with each station separated by 15m. One can think of the shower as a plane wave front perpendicular to the shower axis which passes by the array of stations, striking them at different arrival times depending on direction of travel. The time of firing of each station is determined from the arrival time distribution of figure 20 and including a variable station experimental time resolution. The station time resolution determined from measurements is 1.4 nsec. Earliest arrival triggering is assumed and the time of arrival is varied by a Gaussian distributed error. The electron density at each station is given by the curve of figure 19, scaled to the electron shower size.

The time that a shower hits a station is taken to be the earliest time of the 2 to 4 scintillators which fired. Quantities measured are the *time differences between nearest neighbor stations*. The set of time differences between stations along the x-axis are called tx_i and along the y-axis ty_j . The shower direction cosines can be found by performing a weighted average over the measured time differences as

$$n_x = (c/d) \cdot \sum tx_i \cdot w_i / \sum w_i$$

$$n_y = (c/d) \cdot \sum ty_j \cdot w_j / \sum w_j$$

where c is the speed of light and d is the station separation. The w_i and w_j are weights associated with each station pair i and j taken to be the sum of all scintillator pulse heights in the 2 linked stations. Shower cores have been taken to fall within the array perimeter. All calculated properties of the array have been parameterized according to shower size.

Figure 21 shows the calculated angular resolution vs array timing precision for showers of two different sizes. For less than 1 nsec the angular resolution is dominated by shower fluctuations. The effective shower time spread is shown in the inset of figure 21 vs shower size.

Figures 22 and 23 show angular resolution vs station area and shower zenith angle respectively. The timing precision for a fixed shower size is not strongly dependent on zenith angle for angles $< 30^\circ$. However, due to the steeply falling spectrum and the strong dependence of size on slant depth, the maximum effective observing angle is about 30° . (At 30° zenith angles, an incident cosmic ray of ~ 300 TeV produces on average about the same shower size at ground level as a vertical 100 TeV shower. Due to the steeply falling spectrum, there is about a factor of 6 less of these showers.) Thus, useful observations are restricted to a cone of $1/2$ angle 30° .

Angular resolution can be enhanced by placing a 1 r.l. lead converter on top of each counter. There are many gamma rays near the 84 MeV critical energy in air which can readily convert to e^+e^- pairs in lead whose critical energy is only 7 MeV. Shown in figure 24 is the density of gamma rays vs arrival time for various core distances. The gamma ray density near the shower front peak is nearly twice that of the electrons, thus these gamma rays carry good shower timing information. When they convert they produce about 1.7 e^+e^- pairs on average and the shower front timing is greatly sharpened. This is illustrated in figure 25 where the density of electrons, *after passing through 1 r.l. of lead*, is vs arrival time is plotted for different core distances. This figure does not reveal, however, the correlation in distance between the e^+e^- produced by the gamma conversion, a fact needed to properly calculate the effect of the lead converter.

Counter prototype studies indicate that the converter increases the effective shower size by 1.35 and reduces the timing spread by 1.25. The energy threshold is reduced by about 0.8 and the angular resolution is improved by about 1.4. These effects increase signal to noise by about 1.4.

4.2.3 Optimization

A number of authors have argued that unless the gamma flux falls faster than $E^{-0.8}$ (see Section 3.1 on sensitivity) that the lower one can push the energy threshold the more optimum the signal to noise. We will show that such a conclusion is unwarranted since it neglects the growth of acceptance area that can be realized by separating detectors at increased spacing, a process which is an option for designers of ground arrays where the basic constraint is financial which usually translates to fixed numbers (within rather narrow limits) of detectors. There are several competing effects, however, and the final optimization, even after careful analysis, ultimately

ends up as more or less a matter of one's bias and taste eg. how is the gamma spectrum likely to behave with energy? Does it fall as E^{-1} or faster? Does it terminate at 1 PeV? Is the region between 100 TeV and 1 PeV unlikely because of a short gamma ray mean free path through the galaxy, etc.?

For example, decreasing detector spacing would certainly lower the energy threshold, decrease the fiducial area (given a fixed number of detectors, more or less) until ultimately the area was so small that no events would be detected. It's not clear what would happen to the angular resolution. On the other hand spreading the detectors too far apart, although gaining area would ultimately eliminate the possibility of even triggering at all due to the rapid fall off of the electron lateral distribution. A reasonable guess might be about 15m where the radial electron density drops by a factor of 10 from that at the core. A somewhat more quantitative estimate can be made by calculating the number of days required to establish a 6σ signal assuming a gamma flux level of the value where detection has been claimed. An examination of the literature¹ shows that at 100 TeV (discounting possible sporadic bursts) the detectable energy flux Σ for Cygnus X-3 is $100 \text{ eV cm}^{-2} \text{ s}^{-1}$. We will take this value as our point of normalization and perform the optimization calculations for 2 different choices of gamma ray spectra, one which falls as E^{-1} (what a lot of investigators say (and hope) and $E^{-1.55}$ or one which behaves like the cosmic ray background in the VHE region.

The calculations have been parameterized by shower size rather than energy for ease of calculation. They can be related by noting that $N_a \sim E^{1.13}$ and $N_e = 2.7 \cdot 10^4$ at 100 TeV for Dugway. The integral size spectrum is given by $N(>N_e) \sim N_e^{-1.35}$. Figures 26 and 27 show the array efficiency and angular resolution vs shower size for different detector spacing. Obviously, tighter spacing lowers energy threshold and improves angular resolution (at a fixed shower size). We define the size threshold to be the size at which triggering is 50% efficient and then use those sizes (determined from figure 26) to estimate the array angular resolution (from figure 27) as a function of detector spacing. Furthermore, we convert those sizes to energy thresholds using the relations above. Finally, we note that from the sensitivity analysis of section 2.1

$$\Sigma(\text{eV cm}^{-2} \text{ s}^{-1}) = 3 \cdot 10^{10} \cdot 60 \cdot N_{\text{sig}} \cdot E^{0.23} \cdot (r \cdot A \cdot t)^{-1/2}$$

and setting $N_{\text{sig}}=6$, $r=1$, $A=1000 \cdot x^2$ (where x is the detector spacing), $\Sigma=E \cdot F_g$, and $F_g \sim E^{-1.55}$ or E^{-1} we get

$$t_{1/2} = .55 \cdot 10^{10} \cdot 60 \cdot E^{0.23} / (x \cdot E \cdot F_g)$$

the time required to capture a 6σ signal for Cyg X-3 which we plot in figure 28 as a function of detector spacing x . Note, that in both spectral cases, the time actually drops with increasing detector separation as does the angular resolution. It appears as though one is better off by going to higher energies and greater detector spacing! Clearly though, a gamma spectrum much harder than the ones chosen above would lead to the opposite conclusion.

4.2.4 Technical Details

The parameters of the CASA are given below:

Number of stations	1089
Scintillation area	1.48 m ²
Scintillator thickness	1/2"
# scintillators/station	4 @ 0.37 m ² (2' x 2')
Lead cover	4' x 4' x 0.22" (1 r.l.)
Time resolution	1.4 nsec
Spacing on square grid	15 m
Angular resolution	< 0.011 rad for $N_e > 2.7 \cdot 10^4$

An exploded view of each station is shown in figure 29. A 2" diameter pmt is attached by means of an electrolytic capacitor clamp to the center of each scintillator. Four such scintillators are mounted in a watertight .187" ABS plastic box with UV resistant additives. The scintillators are held in place by a thin plywood sheet and styrofoam spacers. Local electronics are mounted in each station thru a slot in the side.

Perhaps the cleverest feature of this array is the fact that it measures differences in time of arrival between each contiguous station rather than absolute times. This measurement is performed locally at each station rather than at a central electronics trailer. This feature means that long, costly high quality cable runs to each station from a central hut are unnecessary and each station's TDC system needs a full range of no more than 100 nsec. Thus, it's easy for the TDC to achieve 1 nsec resolution as compared to the difficulty which would be incurred if that resolution figure had to be maintained over a full range of about 2 microseconds, the range required for recording absolute arrival times over the entire array. In addition, the pulse heights from each scintillator are locally digitized. Thus, 8 times (4 "internal" times for 4 counters/each station and its 4 "external" times for the 4 neighboring stations) and 4 pulse heights are recorded for each event. The data for several events are stored in local buffers. Eventually the data is dumped via ethernet to a central computer (once every 30 sec). An on-board microprocessor manages data acquisition, local electronics diagnostics and calibration, and ethernet communication.

A station is alerted when at least 2 scintillators are struck within 30 nsec; single station counts are ignored. Thus, local shower densities of about 1.5 m^{-2} are required for a station hit. Single station count rate is about 6 hz.

A station trigger pulse is sent to central control if all 4 scintillators are hit. Upon receipt of a specified number of such hits within $\sim 0.5 \text{ } \mu\text{sec}$ an array trigger condition is broadcast by central control. All alerted stations digitize TDC and ADC sample and hold voltages and store them in local buffers. If an alerted station does not receive an array trigger within 5 μsec , its sample and hold circuits are reset. At an alert rate of 6 hz, dead time is $3 \cdot 10^{-5}$. A typical trigger will involve about 45 stations so the probability that any one of these is dead during an event is about $1.5 \cdot 10^{-3}$.

A schematic of the electronics is shown in figure 30. It uses a dual high/low discriminator technique to insure good timing accuracy. The high level discriminator is fully efficient for minimum ionizing

particles and the low level discriminator is set to about 25% of the high level value, corresponding to about 2 photoelectrons. The measured time resolution is shown in figure 31. Typically, it is about 1.4 nsec for through going muons, a figure which can be improved to about 1.1 nsec if pulse height information is used to correct for slewing.

4.2.5 Reconstruction of Real Showers

To date, the CASA array consists of 49 stations laid out on a square grid. These stations have been operational for several months so many of the design features have been checked in a preliminary way with real data. The discussion that follows will be based upon a preliminary analysis of data accumulated between Feb. 2 and Feb. 6, 1989 during 13 6-8 hour runs of about 20000-30000 events each (295400 total events).²⁸

The technique of shower reconstruction is simply illustrated for the one dimensional simplified case shown in figure 32. A shower is shown striking 3 detectors on the ground at a zenith angle θ . The shower front is a plane wave advancing at speed c . Hence, $\sin(\theta) = c \cdot \delta t / d$. The generalization to 3 dimensions is straightforward. The terrain upon which the stations reside at the Fly's Eye II site is not quite flat. Height differences can be as much as 2.5m. Shower reconstruction has to take this into account. The unit vector \mathbf{n} denoting shower direction can be calculated from the timing data in the following way

$$\mathbf{n} = n_x \mathbf{i} + n_y \mathbf{j} + n_z \mathbf{k}$$

and a plane perpendicular (basically, the shower front) to that vector is given by

$$n_x(x-x_0) + n_y(y-y_0) + n_z(z-z_0) = 0$$

where (x_0, y_0, z_0) is any point in the plane. If at $t=0$, the shower passes through this origin then

$$n_x x + n_y y + n_z z = 0$$

Since the shower front moves at velocity $\mathbf{v} = c\mathbf{n}$, at some time t its geometry is described by

$$n_x(x-n_x ct) + n_y(y-n_y ct) + n_z(z-n_z ct) = 0$$

and noting that $n_x^2 + n_y^2 + n_z^2 = 1$ we obtain

$$n_x x + n_y y + n_z z = ct$$

which is the equation of a shower front moving in the direction \mathbf{n} having passed through some arbitrary origin at some time $t=0$. If, at time $t=t_i$, the shower front strikes station i at $(x_i, 0, h_i)$ then

$$n_x x_i + n_z h_i = ct_i$$

and similarly for station j . Subtracting the above equation for box i and j gives

$$n_x = [c(t_i - t_j) - n_z(h_i - h_j)] / (x_i - x_j)$$

Similarly, if the shower strikes station i at $(0, y_i, h_i)$ at time t_i and station j at $(0, y_j, h_j)$ then

$$n_y = [c(t_i - t_j) - n_z(h_i - h_j)] / (y_i - y_j)$$

If boxes i and j are neighbors, then $(x_i - x_j) = (y_i - y_j) = d$, the box separation. Note that $(t_i - t_j)$ are simply the arrival time differences t_{ij} between stations. Thus

$$\begin{aligned} n_x &= [ct_{ij} - n_z(h_i - h_j)] / d \\ n_y &= [ct_{ji} - n_z(h_i - h_j)] / d \end{aligned}$$

Let's consider in detail how the actual timing measurements yield the best estimates for the arrival time differences t_{ij} between 2 adjacent boxes (either in the x or y direction). When the first counter in station i is struck its low level discriminated signal is sent through a delay to its TDC. When a 2nd counter in the station is hit, the AND of the corresponding high level discriminators signify a station alert and start all 8 TDC's in the station. All delayed low level discriminator hits will stop their respective TDC. The resulting time recorded is the "internal" arrival time for that counter relative to its station alert condition plus a fixed offset. If T_i is the absolute time of the earliest counter hit in station i , A_i is the absolute time that the station alert condition occurred, then the internal time measured is

$$T_i = T_i - A_i + \delta_i$$

where δ_i is an offset which, we will see, will enter into the final reconstruction in the form of offset differences that can be determined from the data. When station i is alerted, it sends out pulses to each of its 4 neighbors. These signals will stop the appropriate TDC in each of these neighbors. If the neighbors are alerted, then each one will stop the TDC in the other giving the "external" times τ_{ij} and τ_{ji} . Each of these times is the time that one station was alerted relative to the other again plus a fixed offset. If A_i is the absolute time that station i was alerted and δ_{ij} is the fixed offset from station j to station i , then the external time measured in each station is

$$\tau_{ij} = A_j - A_i + \delta_{ij}$$

We can now calculate the station arrival time differences using these recorded times:

$$t_{ij} = (T_i - T_j) + (\tau_{ji} - \tau_{ij})/2 - O_{ij}$$

where $O_{ij} = (\delta_i - \delta_j) + (\delta_{ji} - \delta_{ij})/2$

are offset differences, expected to be small, but which can be determined from the data.

The best value for the event direction cosines has been determined by taking a weighted average of each component above, weighting each

projection by the total number of particles estimated to have passed through each station in the linked pair which contribute to that particular t_{ij} . An obvious difficulty with the above equations is that they depend on knowing n_{ij} . Two approaches have been tried. One is to use $\langle n_z \rangle$, the average over all events (≈ 0.91), or an method which first uses $\langle n_z \rangle$, then upon obtaining n_x and n_y , recalculating n_z and then iterating until convergence. The first approach, utilizing $\langle n_z \rangle$ in a single pass has been found to be as accurate as the more computationally intensive iterative method.

The number of particles passing through each station can be estimated by using the pulse height data in the following way. First, pedestals must be subtracted. Secondly, the pedestal corrected pulse height corresponding to a single particle was estimated by averaging pulse heights obtained when only 2 of 4 counters in each station fired, the assumption being that the most likely situation was that a single particle had passed through each counter. This method, though crude, is probably adequate to generate weighting factors (if the value obtained is proportional to the pulse height appropriate to a single minimum ionizing particle, then the proportionality factor will drop out of the weighting anyway).

The measured "internal" time differences require several corrections. Pulse slewing effects are the most important. Slewing corrections have been determined by examining discriminator firing time vs pulse height and finding an empirical relation between the two. Every firing time is then corrected accordingly.

Finally, the relative offsets O_{ij} can be found by noting that both $\langle n_x \rangle$ and $\langle n_y \rangle$ for all the data should be zero. Thus, combining the expressions for t_{ij} and $\langle n_x \rangle$, we get

$$O_{ij} = \langle (t_i - t_j) + (t_{ji} - t_{ij})/2 - n_z(h_i - h_j)/c \rangle$$

where the right side is averaged over a large number of events.

4.2.6 Angular Resolution Results

Ultimately, when the full 33 x 33 station array is operational, data will be cut to insure that the core is within the 500m x 500m array perimeter. For the small portion of the array now operational, that criterion has been relaxed. Instead, it has been demanded that the core fall within 25m of the 7 x 7 array center. Even still, core locations are accurate to no worse than about 8m.

Angular resolution has been assessed by dividing the array into 2 parts, each part consisting of 2 of the diagonal counters in each station. Thus, each sub-array covers the entire fiducial area of the undivided array. Reconstruction of angles for each sub-array can then be compared against each other. The resultant angular resolution is then divided by a factor of about 1.54 (according to Monte Carlo) to estimate the full 7 x 7 array resolution. The result is shown in figure 33. Leaving out the pulse slewing correction worsens resolution by about 40%. Other possible factors have minimal impact. Indeed, weighting the direction cosine estimate by raw pulse height instead of by "numbers of particles" as explained previously worsens

resolution by only 2% and is computationally a much easier procedure to carry out.

Possible systematic errors in the reconstruction procedure have been studied by examining the data azimuthal distributions. They are shown in figures 34 and 35 for different zenith angle cuts. All are uniform, within statistics, except the azimuthal distribution of events whose zenith angles exceed 40°. Shown in figure 35 is a Fourier expansion (1st 8 sine and cosine terms) of that distribution; the solid line is the mean of the constant a_0 term and the dotted lines are its standard deviation. The two excesses $\sim 1.8\sigma - 2.5\sigma$ at $\pm 135^\circ$ and $\pm 137^\circ$, if real, are not understood. Possibly, it might be due to the assumption that the shower is a plane wave and curvature of the wave front has so far been neglected in the fitting algorithm. This effect is now under investigation. At any rate, no such problems exist in the data at zenith angles $< 40^\circ$. It is concluded then that the shower reconstruction process correctly orients the z-axis to within about 0.5° .

Figures 36a through 36h show how the angular resolution depends on various parameters of interest, eg, azimuthal angle, core distance, zenith angle, # of particles detected, # box links, # boxes alerted and shower size. Of particular interest is figure 36d which shows resolution vs zenith angle for $N_e > 2 \cdot 10^4$ particles. Note for zenith angles $< 30^\circ$ that the angular resolution is about 1° and as larger shower sizes are demanded (see figure 36h) the resolution saturates at about $0.4^\circ - 0.5^\circ$ which is close to the Monte Carlo prediction for this limited array. Also, note that the resolution scales as the $\sec(\theta_z)$ as can be easily understood (left as an exercise for the reader).

The relationship of resolution to # of station alerts shown in figure 36g is particularly useful since the # of station alerts is a number available to the software that requires no computation. Thus, this number could be quickly used on line in real time to eliminate showers with poor resolution in precise quantitative way.

There is great virtue in building an array with large numbers of small counters. Most arrays in the past have consisted of small numbers of detectors using some for timing measurements only and some for amplitude measurements. Conventional folklore in this field has always been that accurate amplitude measurements from a detector built for constant light output regardless of where the particle struck the detector was necessary in order to measure shower size and core location. The CASA array flies in the face of this mind set. Indeed, shown in figure 37a is the Monte Carlo scatter plot of the number of CASA station alerts vs shower size N_e calculated on the basis of amplitude measurements in the conventional way. Clearly, there is a strong correlation. This is further depicted in figure 37b where the size distribution for 45-48 station alerts (a typical shower for CASA) is shown. It can easily be seen that just a knowledge of the number of station alerts is anticipated to give the size to about $\pm 20\%$. The actual data distributions of figures 38a-38c, in essence showing the strong correlation between number of particles detected, number of station alerts, and shower size verify this prediction, namely if an array consists of a large number of essentially *fiducial* counters without analog capability, one could still locate shower cores and calculate shower size.

4.2.7 Preliminary Size Estimates

An additional check on the CASA array performance can be made by comparing the lateral distribution of showers determined from the data with the well known NKG function. In addition, a size spectrum can be obtained which can be compared with previous measurements in the relevant size region. The NKG function relates the density of particles at a particular perpendicular radius r_p from the core of the shower to the total size of the shower N_e and the shower age parameter s . The shower age parameterizes the relative development of the shower; $s = 1$ at $dN_e/dt = 0$, ie, at shower maximum. It also parameterizes shower diffuseness; older showers (large s) have flatter lateral distributions.

The classical analysis technique for determining a shower's size from the data is carried out as follows: (1) The shower core is found, typically from pulse height information contained in all alerted stations and used to calculate the number of particles which passed through each station. The location of the core is given by

$$X = \sum x_i \cdot n_i \quad \text{and} \quad Y = \sum y_i \cdot n_i$$

where n_i is the relative fraction of particles detected in the i th station. An example of data used for locating the core is shown in the histograms of figure 39. Average core location error is about 8 meters for showers within 25m of the array center.

(2) The perpendicular distance r_p of each station from the core is calculated and the particle density $\rho(r_p)$ is found

$$\rho(r_p) = (\# \text{ particles detected} / \text{area/station}) / \cos \theta$$

(3) A lateral distribution function (the NKG) is fit to $\rho(r_p)$ and the shower size estimated as

$$N_e = \int 2\pi \cdot \rho(r_p) \cdot dr_p$$

Note that the NKG function for $\rho(r_p)$ is

$$\rho(r_p) = N_e \cdot f(s, r_p/r_1) / r_1^2$$

where r_1 is the Moliere radius and is 94m at Dugway (79m at sea level). The function f is

$$f = (r_p/r_1)^{s-2} \cdot (1+r_p/r_1)^{s-4.5} \cdot \Gamma(4.5-2s) / (2\pi \cdot \Gamma(s) \cdot \Gamma(4.5-2s))$$

An approximate NKG function which works just as well is given by

$$\rho(r_p) = A_1 \cdot \exp(-A_2 \cdot r_p) / r_p$$

where $N_e = 2\pi \cdot A_1 / A_2$.

So far, this technique has only been applied to "composite" showers, ie, average showers whose lateral distribution has been built up from a large number of showers of similar characteristics, primarily common values of numbers of total detected particles, the assumption being that, lacking other information, such showers should have similar

radial densities and, hence, total sizes. An example of the resultant data and NKG fits is shown in figure 40. In the case of small numbers of detected particles the fit is not so good at large core distances probably because of the poor estimate at low particle densities (All stations that were not alerted were included as "zeros". This artificially depressed the low particle density estimates. Remember, 2 counters per station must fire in order to generate a non-zero). Conversely, at large numbers of detected particles, the fit is not so good at small radii, probably because of errors in core location (which translate to large inaccuracies in particle densities) along with possible counter pulse height saturation. All in all, though, for a 1st pass analysis effort with this limited array the fits are pretty good.

Finally, the resultant size spectrum is shown in figure 41. It was determined from fits where the shower age was a free parameter and by fixing the age to 1.3, close to the average value of 1.33 as determined from the data a consistent with expectations for showers measured in this size region. The result is that

$$dN/dN_e \sim N_e^{-1.05 \pm 0.08} \quad (20,000 \leq N_e \leq 250,000)$$

$$dN/dN_e \sim N_e^{-2.15 \pm 0.12} \quad (250,000 \leq N_e \leq 800,000)$$

The change in slope probably corresponds to the well-known "knee" in the cosmic ray spectrum at $E \approx 2$ PeV.

All in all, at this stage of operation, it looks as though the CASA array is performing reasonably close to expectations.

4.3 The Michigan Muon Array

The primary purpose of the shallow (detectors buried 10' underground) Michigan muon array is to reduce the background of hadronic showers which fall within any particular solid angle under consideration. A rough example of how well any proposed muon detector must function is given by the following argument: the solid angle Ω which contains 63% of the showers from a point source is $\theta = 0.2$, $\theta_0 = 0$, is the angular resolution. At 100 TeV, $\theta_0 = .011$ rad and the solid angle Ω is $3.8 \cdot 10^{-4}$ sr. The CASA fiducial area A is 10^5 m² and the integral cosmic ray flux $I(>E) \sim 8 \cdot 10^{-9}$ cm⁻² sec⁻¹ sr⁻¹ giving $B = I \cdot \Omega \cdot A \cdot d \sim (d$ is the duty cycle, about 0.25) $2.5 \cdot 10^4$ background events/year. The signal from source with an integral flux of $F_g \sim 10^{-13}$ cm⁻² sec⁻¹ is $0.63 \cdot F_g \cdot A \cdot d \sim 500$ /year. The signal to noise is then $500 / (2.5 \cdot 10^4)^{1/2} \sim 3$. Suppressing the background by a factor of 100 would increase the signal to noise to about 30. This suppression factor would be crucial if the source were transient, ie, say in the case of Cyg X-3 it were to turn on for only 1 day. The above signal to noise would be $(500/360) / (2.5 \cdot 10^4/360)^{1/2}$ or about .16 and the muon rejection would increase that to a respectable 1.6. (Note, however at this low gamma flux level, a 1 day burst would generate only 1.6 events anyway, ie, the detector would not be signal to noise limited -- it would be rate limited. It would only be sensitive to somewhat larger fluxes than 10^{-13} cm⁻² sec⁻¹ regardless of the muon rejection capability.)

Hadron showers are expected to have a high muon content relative to gamma ray showers. This expectation is based on the notion that the

hadronic component of gamma ray showers (responsible for the muons) arises from photoproduction. Typical photonuclear cross sections are $\sim 0.5\%$ of hadronic cross sections. Detailed Monte-Carlo analysis indicate that muon yields from gamma showers are typically 20 times less than that of hadronic showers.²⁹ This is shown in Figure 42 where the numbers of muons (R_{μ} 1 GeV) vs electrons are plotted for proton and gamma ray EAS. Heavy nuclei collisions are even more efficient producers of muons. At a primary energy of 1 PeV, it can be seen that there are about 10^5 electrons and $7 \cdot 10^3$ muons in a typical proton initiated shower but only $2 \cdot 3 \cdot 10^2$ muons in a gamma shower. It is clear that it should be feasible to discriminate between the two classes of showers *if the muon number is measured with good statistics*. This has been the problem with all past attempts at using muons as an effective discriminator --- the muon detectors have simply been too small.

The problem of course is to cover a lot of active area cheaply. And to avoid the problem of electron punch through which would make a gamma shower look like a hadronic one, the muon detector has to either be buried or covered with absorber. This means that detector serviceability becomes a problem. It is just this sort of "mental hang-up" which the Michigan group rather brilliantly circumvented. Their idea was simply to build lots of cheap, reliable detectors, more than you think you need, dig a hole in the ground about 10' deep, bury the detectors and then completely cover the hole with the dirt you just removed, with only the cable carrying both signal and HV coming out of the ground. In other words, forget about detector servicing; if one dies, so be it.

Shown in figure 43 is a schematic of one of the Michigan counters. It consists of a single 5" pmt mounted to a 6' x 4' x 1/4" scintillator. The pmt is clamped inside a PVC watertight housing and the scintillator is housed in a polyethylene watertight wrapper. The design was driven by the availability of the 5" hemispherical pmt from the original IMB proton decay experiment. The counter is about 90% efficient. The counters are arranged in groups or "patches" of 8 x 8 = 64 counters and buried together in a large hole 20m x 20m x 10'. The bottom of the hole is first filled with gravel and sand to provide a flat, soft surface on which to lay the counters. They are then covered with about a foot of sand and finally completely refilled with the original ground. Only 8 cables (8 bundles of 8 conductor RG 58 coax) emerge from each patch where they are routed to the central electronics trailer. So far 512 counters (about 1200 m² active area) in the 8 "inner" muon patches (see figure 17) are operational. 4 patches have operated for almost 2 years and only 1 counter has failed!

The most important feature of a muon array is to identify hadronic showers with good efficiency. One must also take care to insure that gamma showers don't veto themselves. (All vetos, by the way are not hardware vetos. They are instituted, after the fact, in software.) If this probability is less than 10% the problem is not serious.

The mean number of muons accompanying a hadron shower has been estimated in a variety of ways: (1) Muon densities have been measured at the Akeno array³⁰ for showers with $N_e > 10^6$ at an altitude of 950 m cm⁻². These have been fit to a mean lateral distribution of the form

$$r_{\mu} = (1.75 \cdot 10^{-4}) \cdot N_e \cdot R^{-0.75} / (1 + R/R_0)^{2.5}$$

with $R_0 = 350$ m. This lateral distribution (muons m⁻²) is shown in figure 44. The muons are broadly distributed with about 1/2 of them in an area of $\pi \cdot R_0^2 = 4 \cdot 10^5$ m². Extrapolating to Dugway, Utah, we obtain $N_{\mu} = 2000 \cdot (N_e/3 \cdot 10^4)^{0.8}$. Similarly, an MIT group³¹ found at sea level $N_{\mu} = 10^5 \cdot (N_e/10^6)^{0.75}$. This latter relationship must be extrapolated to Dugway (850 g cm⁻²) from sea level (1030 g cm⁻²). We assume that the muons are little attenuated but in contrast, the extra 4.9 r.l. (180 g cm⁻²) of air attenuates the electrons by about 4.7 (for showers in the range $N_e \sim 3 \cdot 10^4$). We get $N_{\mu} = 2270 \cdot (N_e/3 \cdot 10^4)^{0.75}$ in good agreement with the Akeno extrapolation. Finally, from our own Monte Carlo (see figure 42) at $N_e \sim 3 \cdot 10^4$ we get $N_{\mu} = 2000$.

As a rough estimate that things are working right we note that integrating over the above radial distribution, we anticipate that a shower of size 10^5 would yield a mean number of detected muons on the order of 10 - 20 in 8 patches of the muon array. Shown in figure 45 is the raw data on number of muon counters fired/event for about an 8 hour run with only 4 patches operational. The mean number of counters fired is about 11 (corrected to 9.5 for accidentals within the trigger gate of 1 μ sec) which is consistent with expectations.

The mean singles rate in the muon counters is about 0.1% due mostly to background radioactivity. The accidental number of muon counter triggers (for 8 patches or 512 counters) is about $512 \times 6000 \times 10^{-6} = 3$. However, the chance that one of those falls within a 50 nsec window around the real event is only 1/20. Therefore, on the average, there will be only 0.3 counts per event with a mean expected real value of about 10 detected muons at threshold. The chance of 2 coincident counts is even less, about .044.

The veto inefficiency was originally estimated to be about .003 or .016 for assuming that either a single or double muon count could be used to veto gamma rays. These values were calculated by assuming that 512 individual 2.23 m² muon counters were spread uniformly over the $2.5 \cdot 10^5$ m² area enclosed by the CASA array and also assuming showers of a constant size of $3 \cdot 10^4$. It is not practical to bury muon detectors this way. Instead, they are clumped into 160 m² patches and the spacing between patches optimized for minimal veto inefficiency. The result of this calculation is shown in figure 46.

Shown in figures 47a and 47b are the actual distributions of total numbers of muons in a shower whose electron size exceeds 10^4 (figure 46a) and 10^6 (figure 46b). The muon number was obtained by integrating over the muon lateral distribution above on an event by event basis. The shower core location and electron size was determined by the fully operational Utah surface electron array whose details were not described but whose angular resolution is about 1.5° 2 σ and whose fiducial area is about $2.5 \cdot 10^4$ m². The muon size is normalized to the average muon size in showers whose measured electron size exceeds the quoted values. The dashed line represents a conservative 10% cut on muon size (see figure 47) which should not cut out any gamma ray showers. The fraction of showers that survive this cut is the hadronic veto inefficiency or the reciprocal of the

rejection factor. The veto efficiency with 8 patches operational is shown in the table below

Size No	Nu	Rejection	Inefficiency
> 104	830	150:1	$6.7 \cdot 10^{-3}$
> 105	5240	300:1	$3.3 \cdot 10^{-3}$
> 106	33000	4000:1	$2.5 \cdot 10^{-3}$

These inefficiencies are better than the ones originally calculated for 3 reasons: (1) the Utah electron array providing the trigger is smaller than the CASA array and shower cores are much more concentrated within the muon array where particle densities are higher. (2) The array triggers on a size spectrum whose mean is 3-104. The larger size showers generate more muons. (3) Heavier nuclei as well as protons are present in the isotropic cosmic ray background which are more efficient producers of muons.

4.4 The Utah Tracking Cherenkov Telescopes

The University of Utah has deployed 4 Cherenkov tracking telescopes located on radii 120m due East, North, West and South of the center of the UMC installation (see figure 17). Each telescope is thus separated by about 170m. The optics consists of a 13" mirror with a single 2" fast (1.7 nsec risetime) pmt mounted in the mirror's focal plane. The full field of view is about 5°. Each telescope is mounted on a "Sky Sensor" computer controlled equatorial mount. It is sold by Celestron (as well as a number of mail order discount houses) for use by amateur astronomers at a cost of about \$900. The Sky Sensor has its own on board microprocessor which can locally control the telescope equatorial drive or it can act upon instructions sent to it via an RS232 connection to either a terminal or host computer system. The Utah telescopes are controlled by a single IBM clone 286 PC. The data generated, however, are gathered by CAMAC controlled by a MicroVax II Workstation.

EAS trajectories are reconstructed using the fast timing technique previously explained for the CASA array. The main difference here is that the Cherenkov photon yield is so enormous (about 100-1000 times) compared to numbers of electrons that the telescope angular resolution utilizing only 4 detectors is comparable to that of the entire 1089 element CASA array, namely about 0.5°. However, the telescopes can only operate on clear, moonless nights and only 1 source can be tracked at a time.

Pointing accuracy can be checked quite simply by commanding the telescopes to "lock onto" a target star by scanning the DC optical light yield from that star. Usually a bright star near the potential gamma ray source of interest is chosen in order to minimize the angle thru which the telescopes must turn in order to track that gamma ray source, ie. in the case of Cygnus X-3, the telescopes are commanded to lock onto the bright star Vega and after that is achieved, they are commanded to move to the coordinates of Cyg X-3 and then to track. (There is no bright optical source in the direction of Cyg X-3.) Pointing accuracy can be checked by returning to the star of interest, repeating the DC optical scan and finding coordinate errors. An example of the DC scan of the star Vega is shown in figure 49. The

top figure (49a) represents a scan in right ascension at fixed declination. Each "edge" of the scan is found by subtracting the DC background and locating the 1/2 maximum intensity points. The right ascension scan is repeated at different declinations and the resultant 1/2 intensity points are plotted as declination vs right ascension in figure 49b. The circle so defined represents the full angle field of view of the pmt, about 6°. The center of the circle can be located to an accuracy of about 0.25° - 0.5°, good enough to insure that the target is well inside the field of view.

The angular resolution of the Cherenkov telescopes can be estimated crudely in the following way: light spreads out over a distance of about 200m at detectable levels; maintaining a 2 nsec timing accuracy over a baseline of about 170m leads to an angular uncertainty of about $\delta\theta \sim \delta t/(d/c) \sim 2 \text{ ns} / 500 \text{ ns} \sim 1/4^\circ$. This is the error in the direction of the Cherenkov flash, not the EAS direction. Most of the Cherenkov light originates about 5000m altitude and, on the average, the shower core strikes about 100m from a telescope. Thus the EAS is usually inclined by about 1° to the telescope direction. If the shower core is located to within $\pm 20\text{m}$ by Cherenkov pulse height information then this angle is in error by $\delta\theta \sim 20/5000$ or $1/4^\circ$. Moreover, the altitude of maximum light production can jitter by about $\pm 50 \text{ g cm}^{-2}$ or about 2/3 km. This translates to an angular error of about $1/6^\circ$. These errors typically conspire to yield an error of about 0.4° .

In order to assess telescope performance we developed a Monte Carlo simulation based upon the calculations of Hillas.³² The Monte Carlo is used to generate lateral Cherenkov distributions including photon arrival time delays and delay variation as a function of shower energy, zenith angle, altitude and core distance. The telescope data itself was used to constrain the Monte Carlo. For example 4 telescope events could be subdivided into 4 sets of 3 telescope events to experimentally determine rms timing error and pulse height measurement error. The main source of timing error (about 2.7 nsec) is slewing while the amplitude error (about 17%) arises from fluctuations in pmt DC current due to night sky light (triggering threshold is about 7 p.e.). The parameters estimated by the Monte Carlo simulation for the telescope array are then

Energy Threshold	50 TeV
Energy uncertainty	$\pm 15 \%$
Core location error	$\pm 15\text{m}$
Angular Resolution (100 TeV)	0.66°
" (300 TeV)	0.45°

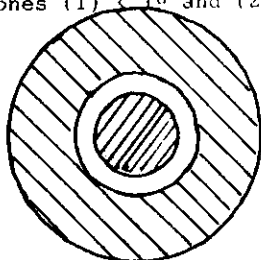
So far the Cherenkov telescopes have operated for about 1 year, tracking the Crab, Her X-1 and Cyg X-3. The power of this technique can be illustrated by presenting some of the preliminary results on Cyg X-3.

So far, we've made a preliminary analysis of about 4 months data (June - September, 1988) obtained from a Cyg X-3 scan. Total scan time was 140.9 hours and total # of triggers above 50 TeV was 18,002 or about 2.1/minute. The number of showers whose cores were within 120m of the array center was 11,206 and after χ^2 on reconstruction we were left with 9030 showers or about 1.1/minute.

Shown in figure 50 is the energy distribution of essentially background cosmic rays within about 1° of the Cyg X 3 direction. (Presumably, any gamma ray EAS comprises a very small fraction of this data sample.) The data is essentially raw. The telescopes are 100 % efficient at $E > 100$ TeV and the acceptance doesn't vary much with energy. Hence, this raw distribution at $E > 100$ TeV is the cosmic ray spectrum. It follows a 2.7 differential power law. Note that electron arrays can in no way compete with this sort of energy measurement.

Shown in figure 51 is the fraction of Utah electron array triggers per Cherenkov trigger vs energy (in units of 100 TeV). Note that the electron array is about 50 % efficient at about 200 TeV. Again, such a measurement is difficult for an electron array alone.

Any gamma ray initiated EAS should come from a direction close to the Cyg X 3 target coordinates. Shown below is a schematic of the full field of view circle centered on the Cyg X 3 target. We have divided that circle into 2 zones (1) $< 1^\circ$ and (2) $1.5^\circ - 3.0^\circ$.



The number of events N_2 whose direction reconstructs in zone 2 should definitely be background cosmic rays. If there are more events N_1 in zone 1 than background then N_1 should be $> N_2 \cdot 1/(32 - 1.52) = 0.148 \cdot N_2$ for roughly uniform acceptance. This is not the case. The 2 numbers are the same to within statistics.

A more meaningful analysis can be made by looking for any excess events at some particular Cyg X-3 phase of its 4.8 hr orbital period. The background in any phase bin can be estimated by noting the fraction of events in zone 2 that are in that phase bin and then multiplying the total number of events in zone 1 by that fraction. This technique automatically accounts for any acceptance differences between the 2 zones. Shown in figure 52a is a distribution of events vs the Cyg X-3 phase. Only events whose energy is greater than 100 TeV have been used where the telescopes are 100 % efficient and which should also generate a mean of about 20 muons in the Michigan muon array. The solid line is the background estimated as explained above. There are no obvious excesses in any phase bin.

A similar analysis can be applied to the subset of data for which $N_{\gamma} > 0.1 \cdot N_{\mu}$, ie, those events which should be gamma enriched. The resultant phase distribution is shown in figure 52b. Again, no significant excess is seen except the possible one of 3σ in phase bin 0.25-0.30. This analysis needs further work but there is certainly no compelling evidence of any strong gamma emission from Cyg X-3 based on this data.

This latter statement can be made more quantitative and its worth doing so to indicate the sensitivity achieved with these detectors. First, we will assume that the 11 events in phase bin 0.25-0.30 is the signal accumulated during observation over all Cyg X 3 phases and then calculate the Cyg X 3 flux required to generate that signal.

$$S/B = (F \cdot A \cdot t) / (I(>E) \cdot A \cdot \Omega \cdot t) = F / (I \cdot \Omega)$$

$$\text{hence } F = (S/B) \cdot (I \cdot \Omega)$$

where B is the total number of background events that would have been collected assuming uniform exposure to the 0.25-0.30 phase bin. ($B = I(>E) \cdot A \cdot \Omega \cdot t$ is a background number that increases linearly with exposure time --- acceptance effects are neglected in both the numerator and denominator of the above ratio.) $B = 100$ events (in phase bin 0.25-0.30, no muon cut) times 20 phase bins = 2000. $I(>E) \sim 10^{-8} \text{ cm}^{-2} \text{ s}^{-1} \text{ sr}^{-1}$ and $\Omega = 2\pi \cdot (1 - \cos(1^\circ)) = 9.6 \cdot 10^{-4} \text{ sr}$ so

$$F = (11/2000) \cdot (10^{-8}) \cdot (9.6 \cdot 10^{-4}) \\ = 5.3 \cdot 10^{-14} \text{ cm}^{-2} \text{ s}^{-1}$$

The energy flux is

$$\Sigma = E \cdot F = 10^{14} \cdot 5.3 \cdot 10^{-14} = 5.3 \text{ eV cm}^{-2} \text{ s}^{-1}$$

Note that this value is 1/20 of the energy flux values of previous claims for Cyg X-3 detections! No signal (or at best another 3σ one) at this level of sensitivity should be extremely worrisome to those contemplating entry into this field.

4.5 Combined Sensitivity Estimates

Finally, we list in the table below rough estimates for the sensitivities attainable with the installation just discussed. Energy flux values are quoted without (labelled Σ) and with (labelled Σ_{μ}) muon rejection capability, assuming a muon rejection factor of about 100 at energies greater than 100 TeV. Also, the calculation assumes a 6σ observation during a year's running time. This amounts to an exposure time of 2160 hours for an array and about 180 hours for Cherenkov telescopes.

	$\delta\theta$ degrees	A cm^2	Σ $\text{eV cm}^{-2} \text{ s}^{-1}$	Σ_{μ}	S	B
Fly's Eye	5	$2 \cdot 10^8$	800	80	104	30000
Utah e-	2	$2 \cdot 10^8$	94	9	140	54000
Utah Cherenkov	0.7	$4.5 \cdot 10^8$	74	7	22	1300
CASA	0.5	$2.5 \cdot 10^8$	7	0.7	137	50000

The appropriate 6σ flux limits can be ascertained by dividing the energy flux sensitivity values by the energy in eV. It should be

noted that none of the above systems are rate limited for a year's observation.

5 EHE TECHNIQUES

5.1 The Fly's Eye

Most experiments in the past in the EHE regime have consisted of ground based particle arrays in which the properties of the showers have been inferred from a sample of the secondaries taken at a few locations along the shower front at a single atmospheric depth or Cherenkov detector arrays which use fast time sampling techniques of the Cherenkov wavefront to obtain an integral history of shower development. Geometrical reconstruction is carried out via the fast timing technique previously described for the CASA array. However, in the EHE regime, detector deployment is sparse over several square kilometers area; event rate is low, estimation of shower energy is subject to severe fluctuation problems and angular resolution is typically no better than 5-10°.

The Fly's Eye was designed and built to overcome these limitations as well as to provide much more detailed information about shower longitudinal development which could, in principle, allow one to discriminate between EAS generated by protons and heavier nuclei. The detector (see figures 53a and b) consists of 2 centralized arrays of large (62" diameter) mirrors and associated photomultipliers which pick up the atmospheric scintillation light given off by nitrogen molecules excited by the passage of electrons (or any relativistic charged particle) in an EAS. The 2 arrays are separated by 3.5 km and permit stereoscopic viewing of a limited selection of showers. The mirrors (67 at FE I and 36 at FE II) and associated pmt's (12 or 14 per mirror) are arranged in such a way that almost the entire 2 π steradian night sky is imaged by a total of about 880 tubes (at FE I; at FE II about 1/2 of the night sky is imaged). The solid angle of each pmt is about 6.57·10⁻³ sr and the full angle fov is about 5.2°. The detector is capable of seeing a 100 EeV shower at a distance of about 20 km. Hence its fiducial acceptance for such showers is enormous, about 1000 km² sr. This acceptance (shown in figure 54) obviously is energy dependent but saturates at the highest energies. The detector in all its gory detail has been described elsewhere.³⁴ Here I will just mention a few of its salient features.

5.1.1 Signal to Noise Considerations

The fundamental difficulty faced in implementing the Fly's Eye technique involves the extraction of a fast relatively low level light signal in the presence of an enormous backdrop of ambient light present even on clear moonless nights. The ability to expand the range of detectable energies both at the low as well as the high energy end of the spectrum hinges critically on how well these signals can be extracted from noise. Calculation of the signal to noise follows a line of reasoning similar to that put forth in section 3.1 on sensitivity of Cherenkov detectors. A fundamental difference is that here the light source (EAS) is moving across the field of view at the speed of light and at impact parameters ranging from several hundred meters to 10s of kilometers. Hence, pulse widths in any photomultiplier viewing such a light source will vary from ~100 nsec to several μ sec, ie, $\delta t \sim R_p \cdot \theta/c \sim .33 \cdot R_p(\text{km}) \mu\text{sec}$. Moreover, since

shower energies at any impact parameter follow the cosmic ray spectrum, pulse heights will vary accordingly. The upshot is that the detector must be capable of recording pulse height integrals (proportional to shower energy) with a dynamic range close to several times 10³. A detailed analysis of the signal generated by a source moving thru the sky at the speed of light yields

$$S = N_e n_g \cdot (1 + \cos(\theta)) \cdot \exp(-r/L) \cdot A \cdot \epsilon_s \cdot \delta t / (4\pi \cdot R_p^2)$$

where S is the photoelectron yield from a single pmt, N_e is the number of electrons in the shower (varies along the track of the shower), n_g is the scintillation photon yield/electron (about 4 and almost altitude independent), θ is the angle between the line of sight to the shower and the shower direction, r is the distance from detector to light source, L is the scattering length of light in the atmosphere (about 18 km at sea level for 360 nm light), A is the mirror area and ϵ_s is the mirror-pmt optical to photoelectron signal conversion efficiency.

The background night sky noise (or fluctuation in photoelectron yield due to DC pmt current) is

$$N \sim (4 \cdot B \cdot \epsilon_b \cdot A \cdot \delta t)^{1/2}$$

where B is the night sky brightness (5·10⁵ photons m⁻² sr⁻¹ usec⁻¹), ϵ_b is the background light to photoelectron conversion efficiency and the factor 4 is added as consideration for light caused by low energy cosmic rays striking the detector and long term night sky airglow. Hence, the signal to noise ratio scales as

$$S/N \sim \epsilon_s (A \cdot \delta t / \epsilon_b \cdot \Omega)^{1/2}$$

A word about δt is appropriate; essentially, it is an integration time over which noise fluctuations are smoothed out. A priori this time is not known since it is event independent. The best that one can do is to integrate only for the duration of the signal pulse. That's tricky to do here. To give a rough idea of the problem, in 1 usec the background light yields about 2000 p.e. and a 1 σ fluctuation is about 45 p.e. One would hope to trigger on about 200 p.e. or about 1/10 of the DC current. Triggering properly to integrate the low level signal current riding on top of this horrendous noise is fraught with great peril. The Fly's Eye does it by splitting signal paths into several parallel electronic channels implemented with filters of differing time constants and independent triggers which generate integrate gates of different fixed widths. This technique comes close to optimizing for δt . Remembering then that $\delta t \sim \delta \theta$ and that $\Omega = \pi \cdot \delta \theta^2$ we get

$$S/N \sim \epsilon_s (A / \epsilon_b \cdot \delta \theta)^{1/2}$$

Thus, Fly's Eye "visibility" can be optimized by maximizing ϵ_s by using bialkali pmt's, high uv reflectivity primary mirrors with no other secondary reflecting surfaces or lenses, minimizing ϵ_b in the optical spectral region outside the 330 nm to 410 nm nitrogen fluorescence signal region and by minimizing $\delta \theta$. If we note that the number of pmt's N_t required to image the entire night sky scales as 1/ $\delta \theta^2$ we can rewrite the above as

one might conclude that building Fly's Eyes with more and more tubes doesn't buy you very much. This is true as far as signal to noise in triggering and accuracy of measuring photoelectron yields is concerned. Hence the existing Fly's Eyes were built with "only" 1000 pmt's. This, along with a mirror diameter of 1.6m leads to a visibility distance for 100 EeV showers of about 20 km which would give a rate of such events (if they exist) of about 1/yr. This was deemed sufficient for the original Fly's Eye design but it is an insufficient criterion if one wishes to search for EHE gamma ray (or other neutral particle) sources. The angular resolution is just not good enough.

5.1.2 Geometrical Reconstruction

The angular resolution of the Fly's Eye is quite event dependent in a way which is much different than that of other existing EAS detector. This can best be illustrated by examining the "single eye" geometrical reconstruction technique. An EAS appears as a great circle projected onto the celestial sphere. The event geometry is schematically illustrated in figure 55. The pmt hit pattern directions for a real event are shown in figure 56. A fit of a great circle to this pattern yields the coordinates of the plane in space (event "planar" angle) within which the EAS trajectory must lie. Crudely, the angular resolution in this dimension is given by the ratio of the 1/2 angle fov of single pmt divided by the total angular extent or "track length" subtended by the EAS or about $2.5^\circ/70^\circ \sim 2^\circ$. However, the "angle in the shower-detector" plane is usually not so well-defined (all though it can be for showers whose track length is say 120°). This angle is determined by fits to the shower observation angles chi vs arrival time of the light pulse from the shower. (See figure 57). It can readily be seen that the relationship between the observation angle chi (the angle between the directions to the point of EAS ground impact and source of light along the EAS trajectory) and the time of arrival of the light pulse at the detector is given by

$$\chi(t) = \chi(t_0) - 2 \cdot \tan^{-1} \cdot (c \cdot (t - t_0) / R_p)$$

The fits yield the parameters t_0 , R_p and $\chi(t_0)$. An example of a such a fit is depicted in figure 58 for a real event. The angle $\chi(t_0)$ is typically determined to an accuracy ranging from 10° down to about 2° depending primarily upon the angular track length of the event. The impact parameter, R_p , is typically determined to better than 5%. This parameter most directly influences the calorimetric energy assessment which is usually quite good ($\pm 10-20\%$). The parameters R_p and $\chi(t_0)$ are strongly correlated as can be seen upon examination of the chi-squared surface in the vicinity of the minimum depicting the best fit estimates for a typical event (see figure 59). The minimization search process can sometimes lead to poor estimates of these parameters. Thus, error due to a poor determination of the angle $\chi(t_0)$ coupled with the more accurately and consistently well-determined planar angle will propagate into errors of declination and right ascension along the celestial sphere in a highly asymmetric way. Special techniques have been developed to handle these asymmetric angular errors in searching for possible astrophysical sources.

If a shower is seen by both Fly's Eyes I and II, a best fit shower-detector plane can be determined and the intersection of those two planes defines the shower trajectory. In such cases the resultant angular errors are not very different and the angular resolution on the celestial sphere can be easily assessed. Unfortunately, most events are not seen in stereo due to the limited aperture of Fly's Eye II.

5.1.3 Angular Error and Anisotropy Searches

Ignoring, for the moment, problems of angular resolution, an EHE event excess from the direction of Cygnus X-3 emerges with little processing of the Fly's Eye data. Shown in figure 60 is a distribution of events ($E > 0.5$ EeV) as a function of galactic longitude for bins centered on the Cygnus X-3 galactic latitude. The non uniform Fly's Eye exposure accounts for the smooth variation of bin counts but not the narrow excess near longitude 80° where Cygnus X-3 lies.

A detailed analysis of this possible excess requires that the asymmetric angular errors be properly treated. Not only are the errors asymmetric in declination and right ascension along the celestial sphere, but the asymmetry, being driven primarily by the timing fit along the shower trajectory, manifests itself in a non-preferential direction along either the right ascension or declination coordinate. Thus, dividing the sky into right ascension and declination bins in order to search for event excesses in the usual way, will result in a loss of sensitivity. We have handled this problem by developing a computational procedure which is intended to optimize sensitivity to point sources when the data is afflicted with asymmetric angular errors as well as irregularities in exposure time.

Each shower's direction is represented by a probability density distribution on the celestial sphere. Imagine that celestial sphere is represented by an array of grid points, each point represented by the coordinates (ra, dec). Any given shower's direction is represented by a probability density function whose most likely direction is the one assigned by the best fit geometrical reconstruction values. Each assigned ± 1 error in all angular parameters ($\chi(0)$ and the shower-detector planar angle) will translate into a 1 contour on the celestial sphere along the lines of that shown in figure 61. Integration of this function over the entire grid yields a value of 1, ie, the shower has a probability of 1 that it arrived from somewhere. At any point on the grid (direction in the night sky) summing of the density function over all showers gives the total event arrival direction density (showers/deg²).

Each shower's energy is represented by a probability distribution over energies, the width of which depends on the quality of the measured profile of the shower's longitudinal development curve (see figure 62). An energy "cut" than thus be imposed by multiplying each shower's arrival direction probability density function by the probability that it passes the cut. The "weight" of a shower at any point on the grid is redefined to be this rescaled density function and the total shower density at this point is simply the sum over all shower weights. The smearing of each shower's energy reduces the dependence of the results on the precise value of the cut and the smearing of each shower's direction yields a continuous function for

the total shower density, so no binning is required for its evaluation at any point in the sky. When the actual Fly's Eye data is used to evaluate total shower density at any point on the celestial sphere, that density is called the actual density.

Celestial anisotropies can be discerned by comparison of the actual data set with an ensemble of simulation data sets derived from the actual data set under the assumption that the Fly's Eye is responding to an isotropic particle intensity. If the particle intensity were isotropic, then there should be a time independent flux from each direction in local detector coordinates (eg. declination and hour angle; the hour angle of any point on the sky is how it is east or west of the meridian, an imaginary line passing between the north and south pole due overhead, see figure 63). In this case, a shower detected with any particular local coordinates could have arrived with equal probability for those identical local coordinates at any other time of shower detection. The simulation data sets exploit this property. Each simulation data set is constructed from the actual data set by "scrambling" each shower's sidereal time of arrival to a different value selected at random from the actual sidereal detection arrival times while preserving the shower's original declination and hour angle. For any point on the celestial sphere, the total shower density (as described above for the actual data) can be evaluated for each simulation data set. The ensemble of such sets determine a distribution of values for the density at that point. The mean value of that distribution defines the expected total shower density at any point. The fraction of the simulation data sets in which the total shower density at some point exceeds the actual density measures the probability that a density as great or greater than the actual density would occur if the particle density were isotropic. Note that this technique automatically takes into account variations in Fly's Eye acceptance with event zenith angle as well as exposure irregularities due to an erratic duty cycle.

This method yields a density excess at 68% +/- 16% with a chance probability of $6.5 \cdot 10^{-4}$. The distribution of probabilities differs little from a uniform distribution and no other point on the sky (1055 points) has this small a chance probability. Figure 64 shows the significance of this density excess near Cygnus X-3. The contours represent the number of given by $(\rho(\text{actual}) - \rho(\text{sim}))/\delta$ where ρ is the total shower density function and δ is the rms deviation of density values for that sky location. Each contour line increases by 0.5 σ from 1.0 σ up to the 4.0 σ contour immediately surrounding the Cygnus X-3 location. Roughly speaking, the contour map implies that about 25 events came from the Cygnus X-3 direction with a background of about 6 expected.

This latter statement can be made more quantitative by moving randomly selected showers in the simulation data set to the Cyg X-3 coordinates, but offset slightly from that direction by sampling each shower's coordinate error distribution. The number of such showers was adjusted until the mean density at Cyg X-3 agreed with the actual density there. This occurred when the number of such showers above 0.5 EeV was 25. The expected density at Cyg X-3 based on the isotropic only simulations is 0.26 showers/deg². Together with the known isotropic cosmic ray flux above 0.5 EeV of $6.8 \cdot 10^{-6} \text{ cm}^{-2} \text{ sr}^{-1} \text{ s}^{-1}$

¹ gives an effective fiducial area-exposure time product of $1.25 \cdot 10^{18} \text{ cm}^2 \text{ s}$. The estimate $\rho = 2.0 \cdot 10^{-17} \text{ cm}^{-2} \text{ s}^{-1}$

$$F = (25 \text{ showers}) / (1.25 \cdot 10^{18} \text{ cm}^2 \text{ s})$$

$$= 2.0 \cdot 10^{-17} \text{ cm}^{-2} \text{ s}^{-1}$$

The energy flux is then

$$\Sigma = E \cdot F = 10 \text{ eV cm}^{-2} \text{ s}^{-1}$$

a very low sensitivity value in this business as we have previously seen. Note that if the source is 11 kpc away and emitting isotropically, then its energy output would be about $2.3 \cdot 10^{35} \text{ ergs s}^{-1}$.

5.1.4 Other Possible EHE Discriminants

It should be noted that if the above EHE flux from Cygnus X-3 is real that the astroparticles in question *could be neutrons*. The probability that a neutron will survive and not decay along the 11 kpc flight path from Cygnus X-3 to Earth is given by

$$P = \exp(-0.108 \cdot d/E)$$

where d is the source distance in kpc and E is in EeV. $P=0.3$ for Cyg X-3 at $E=1 \text{ EeV}$!

How might one tell the difference between an EeV gamma ray, neutron or for that matter an iron nucleus. Shown in Figure 65 is the longitudinal development curve for EAS generated by the above mentioned 3 types of particles. Note that there are differences but the existing Fly's Eye has no more than a snowball's chance in hell of telling the difference on a shower by shower basis. What's needed is a much higher resolution Fly's Eye to more accurately measure longitudinal development profiles. We are currently trying to develop such a detector (HiRes Fly's Eye) at the University of Utah. Hopefully, it can be implemented before I'm too old and decrepit to travel to Italy again.

1	INTRODUCTION	1
1.1	Description of Problem	1
1.2	Astroparticle Sources	2
1.3	Binary X-Ray Systems	3
2	HIGH ENERGY GAMMA RAYS	5
2.1	The Extensive Air Shower (EAS)	6
2.2	Gamma Ray Hadronic Discriminators	7
3	THE ATMOSPHERIC CHERENKOV TECHNIQUE	7
3.1	Sensitivity	7
3.2	Rejection Factors for Cherenkov Detectors	9
3.3	Problems	11
4	UHE TECHNIQUES	11
4.1	The Utah-Michigan-Chicago EAS Facility	12
4.2	The CASA Array	12
4.2.1	Shower Calculations	12
4.2.2	Estimation of Angular Resolution	13
4.2.3	Optimization	14
4.2.4	Technical Details	15
4.2.5	Reconstruction of Real Showers	17
4.2.6	Angular Resolution Results	19
4.2.7	Preliminary Size Estimates	21
4.3	The Michigan Muon Array	22
4.4	The Utah Tracking Cherenkov Telescopes	25
4.5	Combined Sensitivity Estimates	28
5	EHE TECHNIQUES	29
5.1	The Fly's Eye	29
5.1.1	Signal to Noise Considerations	29
5.1.2	Geometrical Reconstruction	31
5.1.3	Angular Error and Anisotropy Searches	32
5.1.4	Other Possible EHE Discriminants	34

REFERENCES

1. Protheroe, R.J., Proc. 20th Int. Cosmic Ray Conf. 8, OG-3 p.21 (1987).
2. Hess, V.F., Phys. Z. 13, 1084 (1912).
3. Skobel'tzyn, D., Ann. Phys. Lpz. 43, 354 (1927).
4. Linsley, J., Phys. Rev. Lett. 10, 146 (1963).
5. Hillas, A.M., Ann. Rev. of Astron. & Astrophys. 22, 425, (1984).
6. Giler, M., J. Phys. G. Nuc. Phys. 9, 1139 (1983).
7. Jokipii, J.R. and Morfill, G.E., Proc. 19th Int. Cosmic Ray Conf. 3, 132 (1985).
8. Wdowczyk, J. and Wolfendale, A.W., Ann. Rev. of Nuc. & Particle Physics (to be published, Feb. 1989).
9. Tananbaum, H. et al, Ap. J. Lett. 174, L143 (1972).
10. Baltrusaitis, R.M. et al, Ap. J. Lett. 293, L69 (1985).
11. Giacconi, R. et al, Ap. J. 184, 227 (1973).
12. Bahcall, J.N., Bahcall, N.A., Ap.J.Let. 178, L1 (1972).
13. Bartlett, J. et al, Phys. Rev. D 32, 1630 (1985).
14. See for example MACRO and LVD proposals for Gran Sasso and Grande experiment in Arkansas, USA, (1989).
15. Bahcall, J.N. et al, Rev. Mod. Phys. 60, 297 (1988).
16. Bionta, R.M. et al, PRL 58, 1494 (1987).
17. Hirata, K. et al, PRL 58, 1490 (1987).
18. Trimble, V., Rev. Mod. Phys. 60, 859 (1988).
19. Protheroe, R., 20th Int. Cosmic Ray Conf. 8, 21 (1987).
20. Weekes, T., Physics Reports 160, 1 (1988).
21. Hillas, A.M., 19th Int. Cosmic Ray Conf. 3, 445 (1985).
22. Hillas, A.M., Int. Conf. on High Energy Gamma Ray Astronomy, Crimean Astrophysical Observatory Simferopol, Crimea, USSR to be published (1989).
23. Weekes, T. et al, Ap. J. to be published (July, 1989).
24. Li, T. and Ma, Y. Ap. J. 272, 317 (1985).
25. Weekes, T.C. et al., Arkansas Gamma Ray Astronomy Conf. Little Rock, Arkansas (May 9-12, 1989).

26. Snyder, H.S. Phys. Rev 76, 1563 (1949); also see Fig.1 Greisen, K. in "Extensive Air Showers", Progress in Cosmic Ray Physics III (1956).
27. Nishimura, J. and Kamata, K. Prog. Theor. Phys. 5, 629 (1951).
28. Haar, P. and Cronin, J., Senior Thesis, U of Chicago (1989).
29. Edwards, P.G. and Protheroe, R.J., 19th Int. Cosmic Ray Conf., LaJolla paper HE 4.5-7 (1985).
30. Hara, T. et al, 18th Int. Cosmic Ray Conf., Bangalore, paper EA 1.2-13 (1983).
31. Greisen, K., Annual Reviews of Nuclear Science (1960).
32. Hillas, A.M., J.Phys.G:Nucl.Phys 8, 1461 (1982) and same as above p. 1475.
33. Molnar, L.A., private communication (1988).
34. Baltrusaitis, R.M. et al, Nucl. Inst. Meth. in Physics Research A240, 410 (1985) and also A264, 87 (1988).

FIGURES

- Fig. 1 Size and magnetic field strength where astroparticles might be accelerated to high energies. For example, to accelerate protons to 100 EeV must not lie below the diagonal band (lower edge for relativistic plasmas - upper edge for speeds of 1000 km/s.
- Fig. 2 Counts accumulated on .096 second bins from Her X-1 on 11/6/71 during the central 30 sec of a 100 sec pass on Uhuru. The curve is a minimum χ^2 fit to the X-ray pulsations of a sine function, its 1st and 2nd harmonic plus a constant modulated by the detector's triangular response function.
- Fig.3 The difference Δt between the arrival time of an x-ray pulse from Her X-1 and the time predicted for a constant period.
- Fig.4 Her X-1 intensity data (2-6 KeV) during 3 long term ON states. Vertical lines represent orbital eclipses every 1.7 days. Long term ON states last for about 11-12 days followed by about a 24 day OFF state.
- Fig.5 Model for the Her X-1 close x-ray binary system.
- Fig.6 Schematic of hadronic extensive air shower.
- Fig.7 Lateral distribution of secondary components in an EAS at ground level.
- Fig.8 Monte Carlo simulation of 250 GeV (a) proton and (b) gamma ray generated EAS.
- Fig.9 The Whipple Observatory 10m gamma ray telescope.
- Fig.10 Monte Carlo generated Cherenkov images for an atmospheric Cherenkov detector. 1 TeV Nucleon and 320 GeV gamma ray induced images are shown.
- Fig.11 Image of 4 320 GeV vertical gamma ray showers striking the ground at the 4 corners of a quadrant centered on the detector 100 meters away.
- Fig.12 Schematic of Cherenkov image and parameter definition.
- Fig.13 Cherenkov image parameter distribution from Monte Carlo simulations of an on-axis gamma source and an isotropic cosmic ray background.
- Fig.14 Comparison of predicted parameter distributions for background cosmic rays with measured ones.

- Fig.15 Distribution of ON and OFF source azimuth parameters for the Crab (differences shown in inset).
- Fig.16 The distribution of ON-OFF azimuth differences in terms of standard deviations.
- Fig.17 The UMC UHE Gamma Ray Observatory installation. Open boxes - 1000 counters 4 element 1.5 m² Casa 15m separation electron array (500m x 500m). Energy threshold about 300 TeV. Patches - 16 64 element 10 ft underground buried Michigan muon array. Each patch is 128 m². 1 GeV muon threshold. Energy threshold 300 TeV. Central circles - U of Utah Fly's Eye II detector. dark boxes connected by lines - U of U electron array. 36 4 element scintillation counters about 80m radius. dark circles - 4 element 13 inch U of U Cherenkov tracking telescopes 50 TeV threshold.
- Fig.18 Ground-level size distribution for 100 TeV vertical showers. $\Sigma(N_e) \sim 40\%$.
- Fig.19 Shower lateral distribution from Monte-Carlo with NKG function shown for comparison.
- Fig.20 Electron arrival time distribution (m⁻² nsec⁻¹) for different core distances.
- Fig.21 Angular resolution vs timing precision. Inset shows shower time spread vs shower size.
- Fig.22 Angular resolution vs detector area.
- Fig.23 Angular resolution vs shower zenith angle.
- Fig.24 Density of gamma rays vs arrival time delay for different core distances.
- Fig.25 Density of electrons vs time delay for different core distances after passing through 1 r.l. lead.
- Fig. 26 Array efficiency vs shower size for different detector spacing.
- Fig.27 Angular resolution vs shower size for different detector spacing.
- Fig.28 Time required to detect Cyg X-3 at 6 sigma vs detector spacing assuming either an E⁻¹ or E^{-1.55} spectrum and normalized to a gamma flux of 10⁻¹² cm⁻² s⁻¹ at 100 TeV. The upper scale shows the 50% efficient triggering threshold energy.
- Fig.29 Exploded view of CASA scintillator station.

- Fig.30 Schematic of CASA local station electronics.
- Fig.31 Measured time resolution for CASA counters.
- Fig.32 Schematic of 1-dim shower reconstruction.
- Fig.33 Angular resolution of the 7 x 7 CASA array currently in operation made by comparing angles reconstructed from each of 2 "sub-arrays" obtained by dividing each detector station in half.
- Fig.34 Azimuthal distributions for zenith angles within the following ranges:(a) < 15° (b) 15° - 30° (c) 30° - 40° (d) > 40°.
- Fig.35 Fourier expansion (1st 8 sine and cosine) of azimuthal distribution of figure 34d. Solid line is a_0 , dashed lines its error.
- Fig.36 Angular resolution vs (a) azimuthal angle (b) distance of core from array center (c) zenith angle (d) zenith angle for $N_e > 20000$ (e) # particles detected (f) # station links (g) # station alerts (h) shower size N_e .
- Fig.37 (a) Number of station alerts vs shower size (Monte Carlo) (b) Size distribution when 45-48 stations alerted.
- Fig.38 Real data
(a) N_e vs # station alerts
(b) # particles detected vs # station alerts
(c) # particles detected vs N_e .
- Fig.39 Number of particles detected per station in an EAS recorded by CASA (a) $N_d = 250$ (b) $N_d = 1400$.
- Fig.40 NKG fits to radial distributions of average showers built up from showers whose numbers of total detected particles are (a) $N_d = 200 \pm 25$ (b) $N_d = 800 \pm 25$.
- Fig.41 Preliminary electron size spectrum (a) Shower age s is a free parameter (b) s is fixed at the average value of 1.3.
- Fig.42 Number of muons vs number of electrons in proton and gamma ray EAS (Monte-Carlo).
- Fig.43 Schematic of U of Michigan "buried" muon detector. A 5" hemispherical pmt (canabalized from the original IMB proton decay experiment) is housed in a watertight PVC container. A bevelled hole is cut into the scintillator into which the pmt is inserted. The scintillator is wrapped in a watertight, polyethylene bag and clamped to the pmt housing. Counter dimensions are 6' x 4'

or $2 \frac{1}{4} \text{ m}^2$.

- Fig. 44 Muon lateral distribution from Akeno data fits.
- Fig. 45 Distribution of number of muon counters that fire in an event. 4 patches or 256 counters (571 m^2) were operational. Mean number tat fire = 11 (corrected to 9.5 for accidentals within 1 usec gate).
- Fig. 46 Calculated veto inefficiency vs muon patch separation in meters.
- Fig. 47 Distributions of muon size N_μ normalized to $\langle N_\mu \rangle$ for showers whose measured electron size is (a) $N_e > 10^4$ (b) $N_e > 10^5$. The dashed line represents a 10% cut below which gamma ray showers are expected to reside. Hadronic rejection factors for this cut are (a) 150:1 (b) 4000:1.
- Fig. 48 Utah tracking Cherenkov telescope.
- Fig. 49 (a) DC optical scan of Vega, pmt current vs right ascension (24 hours=360°) (b) position of scan edges defined by 1/2 maximum intensity points, declination vs right ascension. Edge error ~ 0.2°. Circle is full field of view of pmt.
- Fig. 50 Energy spectrum measured by Cherenkov telescopes
- Fig. 51 Fraction of Utah e^+e^- ground array triggers per Cherenkov tracking telescope trigger vs energy in units of 100 TeV.
- Fig. 52 Phase plot of background (solid line) and events within 1° of the Cyg X-3 direction. (a) no muon cut (b) $N_\mu < 0.1 \langle N_\mu \rangle$. Molnar³³ ephemis used to get phase.
- Fig. 53 (a) Fly's Eye I installation (b) Single Fly's Eye mirror, housing and associated pmt focal plane cluster.
- Fig. 54 Fly's Eye I acceptance in $\text{km}^2 \text{ sr}$ vs EAS energy.
- Fig. 55 Event geometry for a single Fly's Eye. pmt hit pattern follows a great circle on the celestial sphere (or on the spherical surface defined by the viewing directions of the Fly's Eye "facets". The angle Ψ and impact parameter R_p are defined by fits to the observation angles χ vs time of observation.
- Fig. 56 PMT hit pattern directions shown projected onto surface of Celestial Sphere. Each dot represents a hit, each x an "out of time" noise pulse. Line is best fit of a great circle defining plane in

which the event lies.

- Fig. 57 Kinematics of Fly's Eye EAS timing. T is the time lag between the passage of the shower front and the arrival of the light pulse from any point on the shower viewed by a detector at an angle χ from the direction towards EAS "ground impact".
- Fig. 58 Time of arrival plot for pmt hits of Fig. 56. Θ is the angle between the line of sight to the point of light emission on the shower axis and the shower axis. The horizontal axis is pulse arrival time (scaled by c/R_p).
- Fig. 59 Chi-squared surface in the vicinity of the best estimate of the parameters R_p and $\chi(t_0)$ for a typical event. Parameters are strongly correlated.
- Fig. 60 Distribution of EAS vs galactic longitude. Each bin is 10° wide in galactic latitude centered on +1°. Peak is at Cygnus X-3.
- Fig. 61 Right ascension-declination grid with shower direction probability density function overlaid.
- Fig. 62 Longitudinal development profile of a typical EAS. Shower energy is given by the integral $\epsilon/x_0 N_e dx$ where ϵ/x_0 is the ratio of an electron's critical energy to its radiation length in air ($2.2 \text{ MeV/g cm}^{-2}$). There is about a 10% correction for undetected energy.³⁴
- Fig. 63 Schematic of declination and hour angle (local detector coordinates of the shower arrival direction.
- Fig. 64 Cygnus X-3 centered on this $20^\circ \times 20^\circ$ probability contour plot with ra and dec as the x and y axes. The dots are points on the galactic plane separated by 1° of galactic longitude. Each contour around Cygnus X-3 has $\sigma = 1.0, 1.5, 2.0, 2.5, 3.0, 3.5, 4.0$
- Fig. 65 Longitudinal development profiles for EAS initiated by a nucleon, iron nucleus and gamma ray each of total energy 1 EeV.

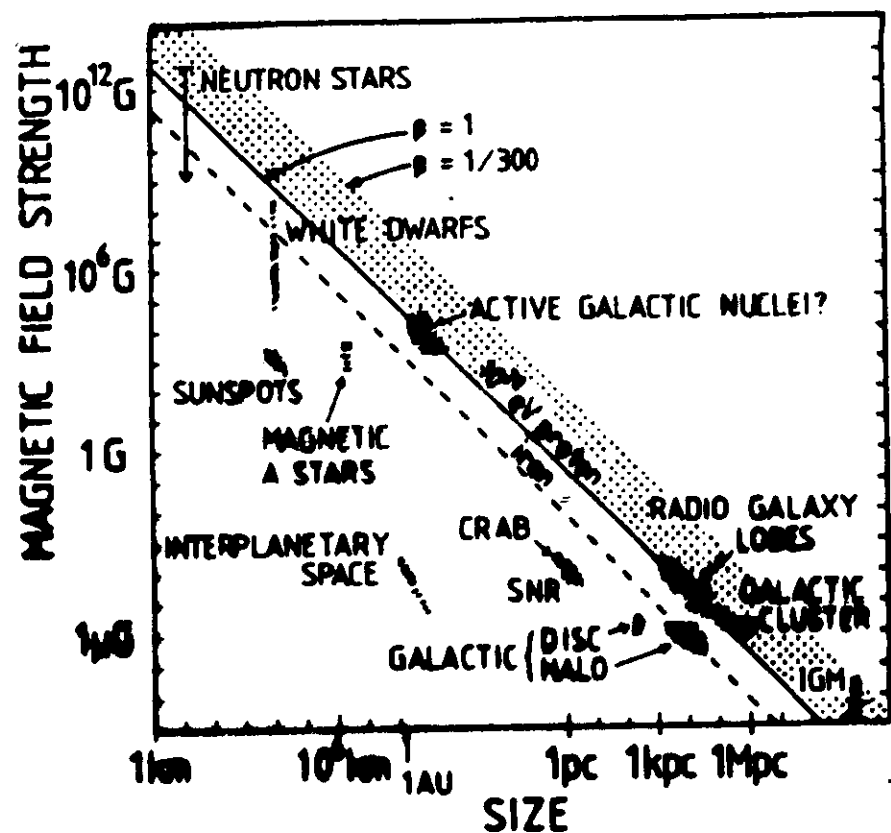


Figure 1 Size and magnetic field strength of possible sites of particle acceleration. Objects below the diagonal line cannot accelerate protons to 10^{20} eV.

SOURCE IN HERCULES (2U1705+34) November 6, 1971

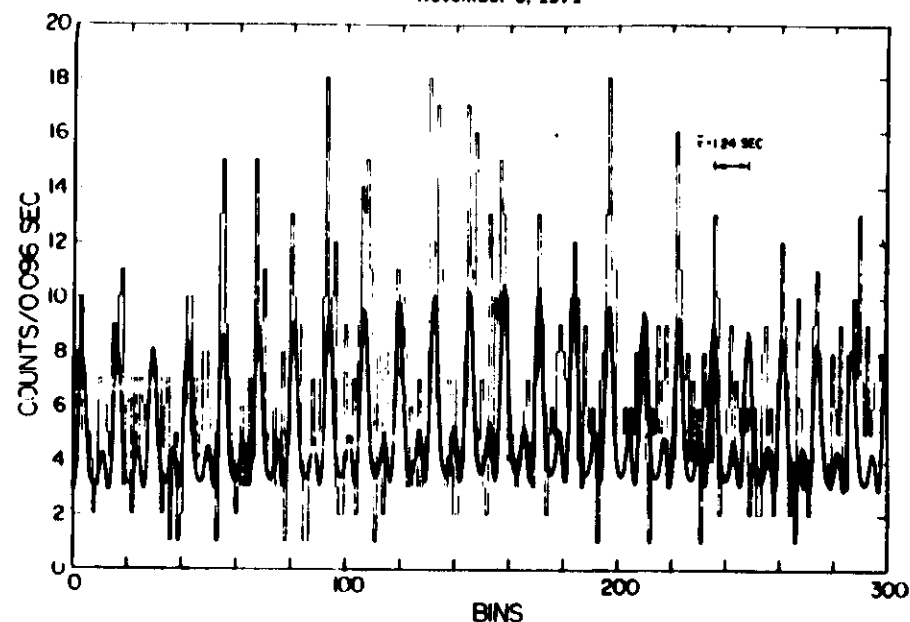


Fig. 2 The counts accumulated in 0.096 second bins from Hercules X-1 during the central 30 seconds of a 100 second pass on 1971 November 6. The heavier curve is a minimum χ^2 fit to the pulsations of a sine function, its first and second harmonics plus a constant, convoluted by the triangular response of the collimator. The functional fit is systematically below the peak counting rate partly due to the sharpness of the pulsing and partly due to the minimum χ^2 technique.

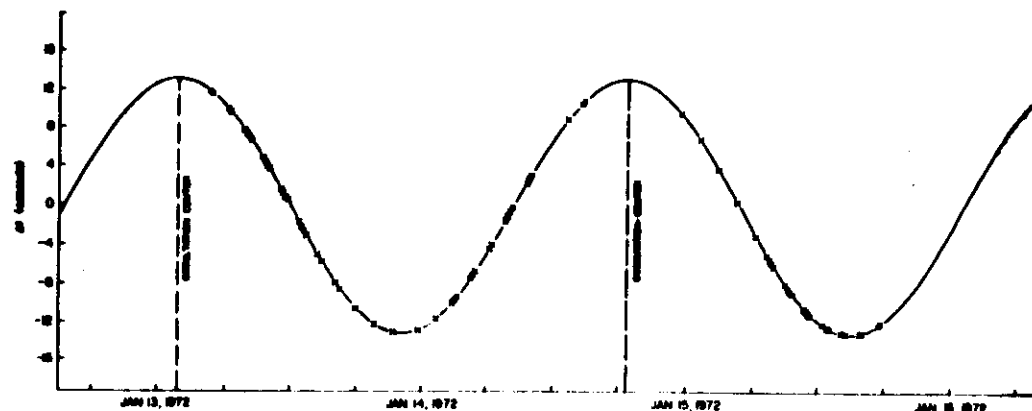


Fig. 3 - The difference Δt between the time of occurrence of a pulse and the time predicted for a constant period is plotted as a function of time. A best fit function and the values of the parameters are given: $\Delta t = b_0 + b_1 t + b_2 t^2 + b_3 \sin[2\pi(t - t_0)/P]$, $\chi^2 = 1.24772 + 0.000001$, $a = 0 + 0.000000$, $b = 13.19 \pm 0.03$ sec.

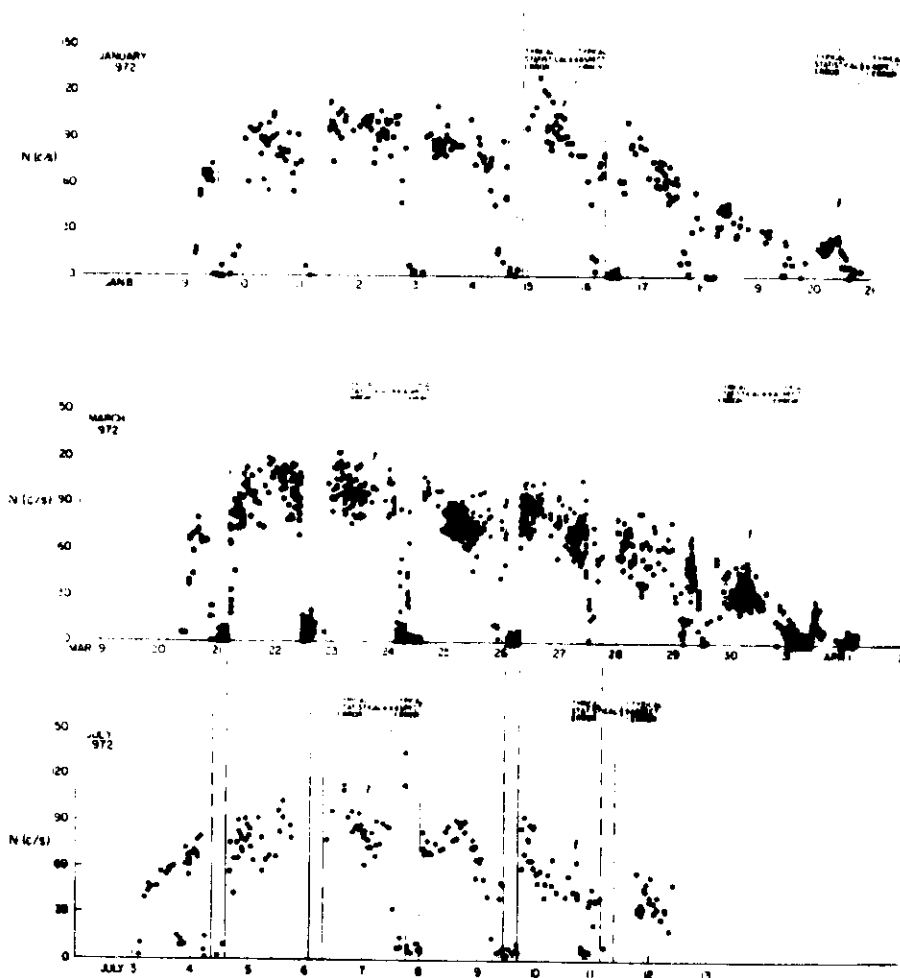


FIG. 4 — Hercules intensity data (2-6 keV) during three ON states. The vertical lines represent the orbital eclipses, whose positions are determined accurately from the pulsation Doppler analysis. Typical errors appropriate for different groups of data are shown; the statistical error bar is relevant for point-to-point comparisons, and the aspect error bar is relevant for day-to-day comparisons. It should be noted that most intensity points below about 10 counts s^{-1} are upper limits.

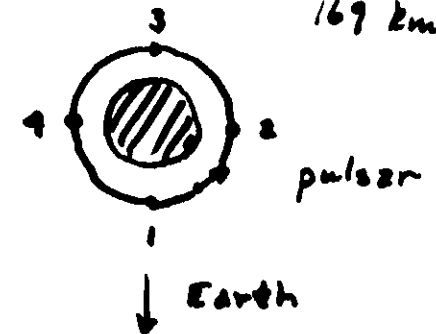
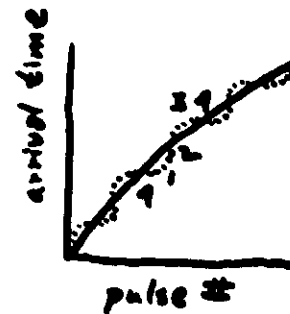
Parameters of Herve X-1

Observe:

1. Orbital period: T 1.7 days
2. Projected semi-major axis: $a_x \sin i$

Doppler Delays

13 sec
($3.9 \cdot 10^6$ km)
 $V_x \sin i$
169 $km s^{-1}$



Also:

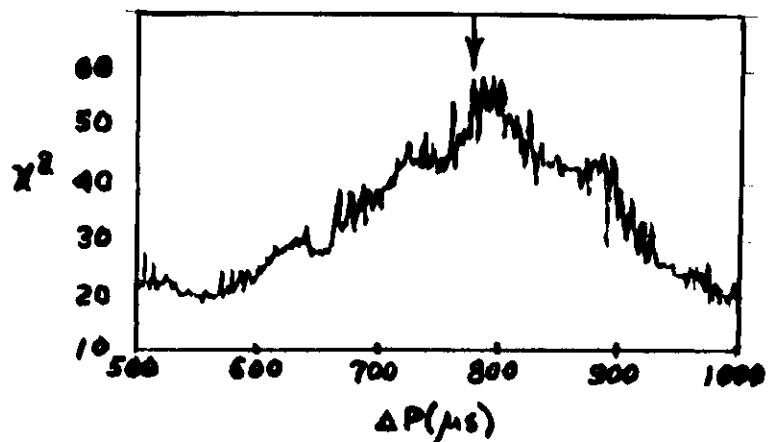
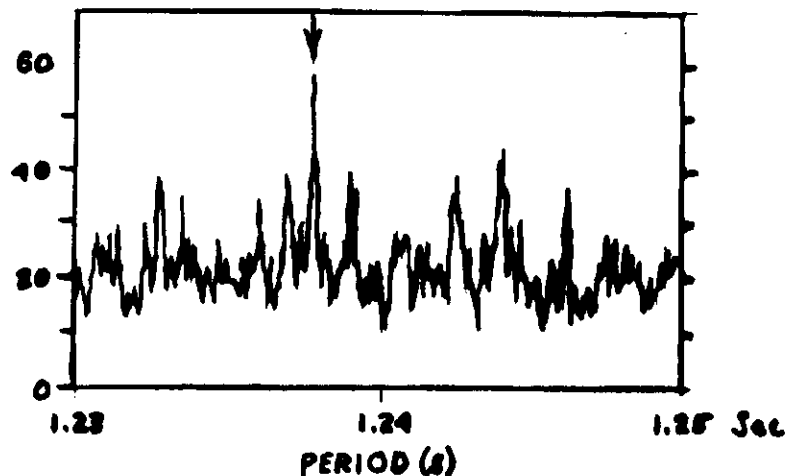
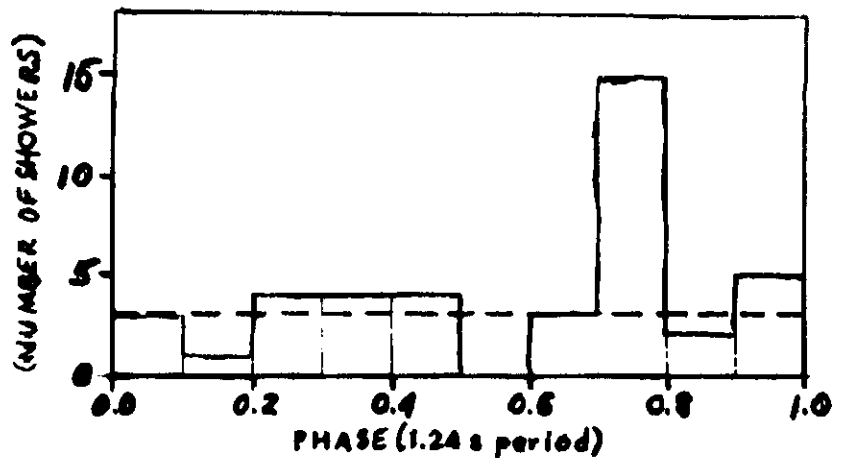
3. Amplitude of Doppler Velocity curve for companion star: $V \sin i$ 20.2 $km s^{-1}$
4. Duration of X-ray eclipse: $\theta_e \sim 25^\circ$

\Rightarrow At time of our observations

1.7d Orbital Phase $\Phi \sim 0.66$

35d X-Ray phase ~ 0.63

1.24s pul. phase - not known



FLUX (averaged over 1.24 s period during hot 40 minute interval)

$$F = \left(\frac{S}{B} \right) I(> E) \Omega = 3.3 \cdot 10^{-12} \text{ cm}^2 \text{ s}^{-1} \text{ at } E \gtrsim 1 \text{ PeV}$$

CRUDE LUMINOSITY Estimate

$$L_\gamma = F \bar{E} 4\pi d^2 \quad d \sim 5 \text{ Kpc}$$

$$L_\gamma \approx 10^{37} \text{ erg/s} \quad \text{comparable to X-Ray}$$

Indicates sporadic, efficient acceleration

Statistics

$$P(15, 3.0) = 3 \cdot 10^{-7} \quad - \text{but}$$

$$\# \text{ tries} = 10 \text{ bins} \cdot 4 \text{ phases} \cdot 7 \text{ data runs} = \underline{280}$$

$$\therefore \text{chance Probability} \sim 2 \cdot 10^{-4} \quad (\sim 3.5 \sigma)$$

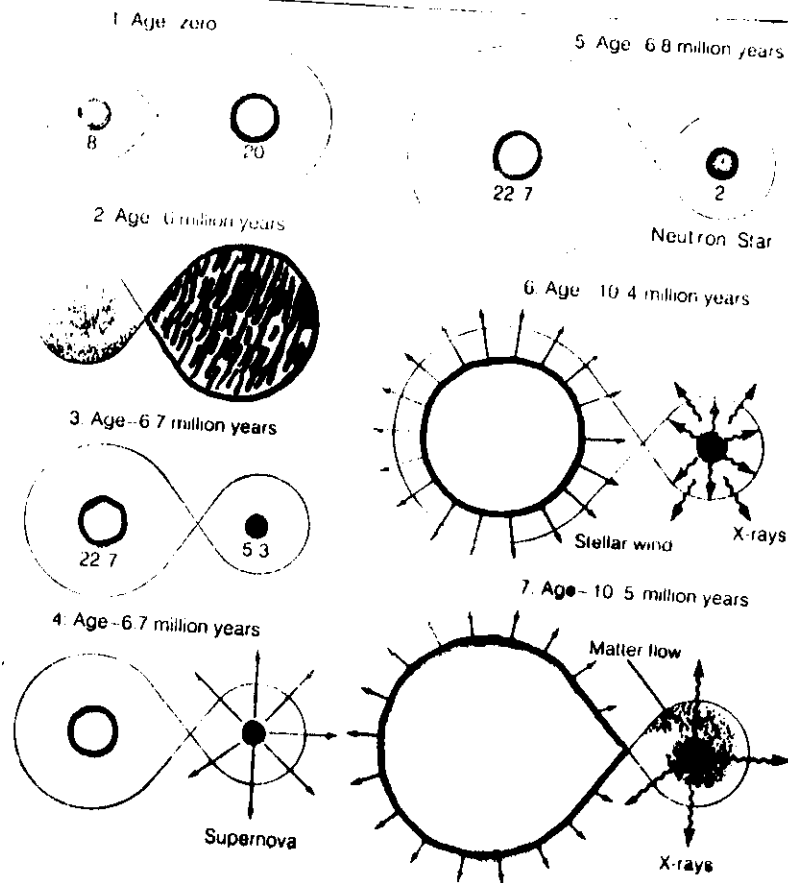


FIG 16.29 MASS EXCHANGE AND EVOLUTION IN A CLOSE BINARY SYSTEM. The star that is initially more massive evolves faster and giant it deposits material on the companion. This speeds up the evolution of the second star, so that it expands and returns matter to the first one is by this time a compact object, such as a neutron star, the consequences of this stage of mass transfer can be violent (see Chapter 17).

SUMMARY

Progress in stellar evolution are deduced from observations of stars in various stages, particularly in clusters, from theoretical calculations.

Distances to clusters can be determined by plotting color-magnitude diagram and comparing the location of the main sequence with that of a standard H-R diagram.

Fact that all the stars in a cluster have the same age.

Distances from star to star within the cluster are determined by differences in stellar mass. This allows us to determine how stars of different mass evolve.

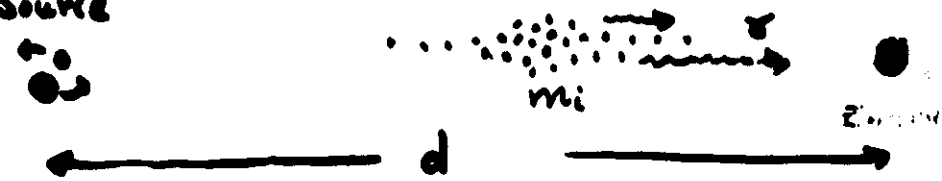
4. The age of a cluster can be inferred from the location of its main sequence turnoff point.

5. Stars in the process of forming are often embedded within dense clouds and are best observed in the infrared wavelengths.

6. A star forms from the gravitational collapse of a cloud of gas and dust.

An Argument for Photons

Source



A particle of mass m travelling at $v < c$ will arrive later than photon by

$$\Delta t = d / 2c v^2$$

- Thus, particles with a spectrum of energies will undergo time dispersion.

$$\text{Suppose } \frac{dn}{dE} = K (1 - e^{-u}) u^{-3.5} \quad (u = E / E_{\text{thresh}})$$

- A modulation of signal intensity of period P would be reduced by a factor of 3.0 if, for particles at $E = E_{\text{thresh}}$, $\Delta t > 3.5$

$$\text{Hence } \Delta t_{\text{thresh}} > \left(\frac{d}{7cP} \right)^{1/2}$$

$$\text{or } mc^2 < \left(\frac{7cP}{d} \right)^{1/2}$$

Conclusions

Hercules X-1

$$P = 1.237 \text{ sec} \quad d = 5 \text{ kpc}$$
$$E_{\text{thresh}} \sim 300 \text{ GeV}$$

$$\Rightarrow m_e^2 < 1.2 \text{ MeV}$$

Cygnus X-3

$$P \sim 12.6 \text{ ms}^{\dagger} \quad d = 12 \text{ kpc}$$
$$E_{\text{thresh}} \sim 700 \text{ GeV}$$

$$\Rightarrow m_e^2 < 0.2 \text{ MeV}$$

or: if one relies on sharpness of 4.8 hr period instead ---

$$\Rightarrow m_e^2 < 60 \text{ MeV}$$

- particles are neutral (not electrons)
- interact in earth's atm (not neutrinos)

\Rightarrow They are photons

16

Nature's Own Particle Accelerator

by M. Mitchell Waldrop

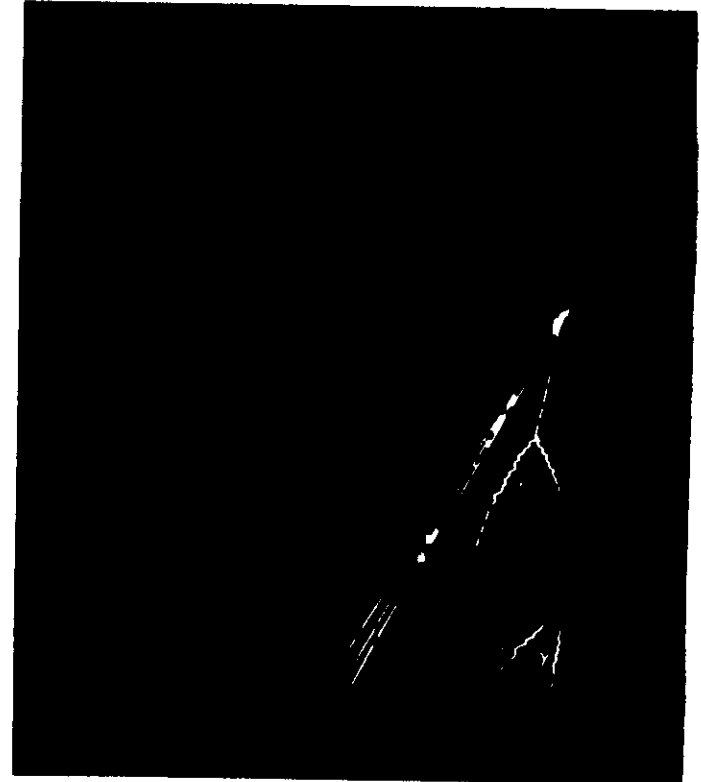
Cosmic rays, at energies future accelerators can't hope to match, still have much to teach physicists and astrophysicists.

Austrian physicist Victor F. Hess discovered the ionizing phenomenon in 1912 when his ground detectors acted up all hour. Thinking he took his instruments too far from the molecules of air around him—on land, or electrically charged, or in his observation, he argued—the ionizing radiation must be descending from the heavens. Giving Hess credit for his discovery, the nature of his discovery was one of the most important in the history of the next three decades. It was Nobel laureate Robert A. Millikan who in the 1920s was the first to refer to the radiation as "cosmic rays."

The cosmic rays, made up of cosmic rays, are now known to be the positively charged nuclei of hydrogen atoms. Next, most of them are helium nuclei, or alpha particles, followed by nuclei of carbon, nitrogen, oxygen and so on. They are most abundant in the atmosphere. Except for particles having the highest energies, cosmic rays cannot penetrate the earth's surface. They come from all directions, their intensity increased primarily by interaction with the magnetic field encountered near the top. They come infrequently, however, with a few particles per square centimeter per second hitting the atmosphere. And this is a large number.

Air shower: A cosmic ray's collision with a molecule in the atmosphere results in a relatively narrow, intense core of heavy particles (hadrons) and a penumbra of others—all grist for the physicist's mill.

M. M. Waldrop, by permission



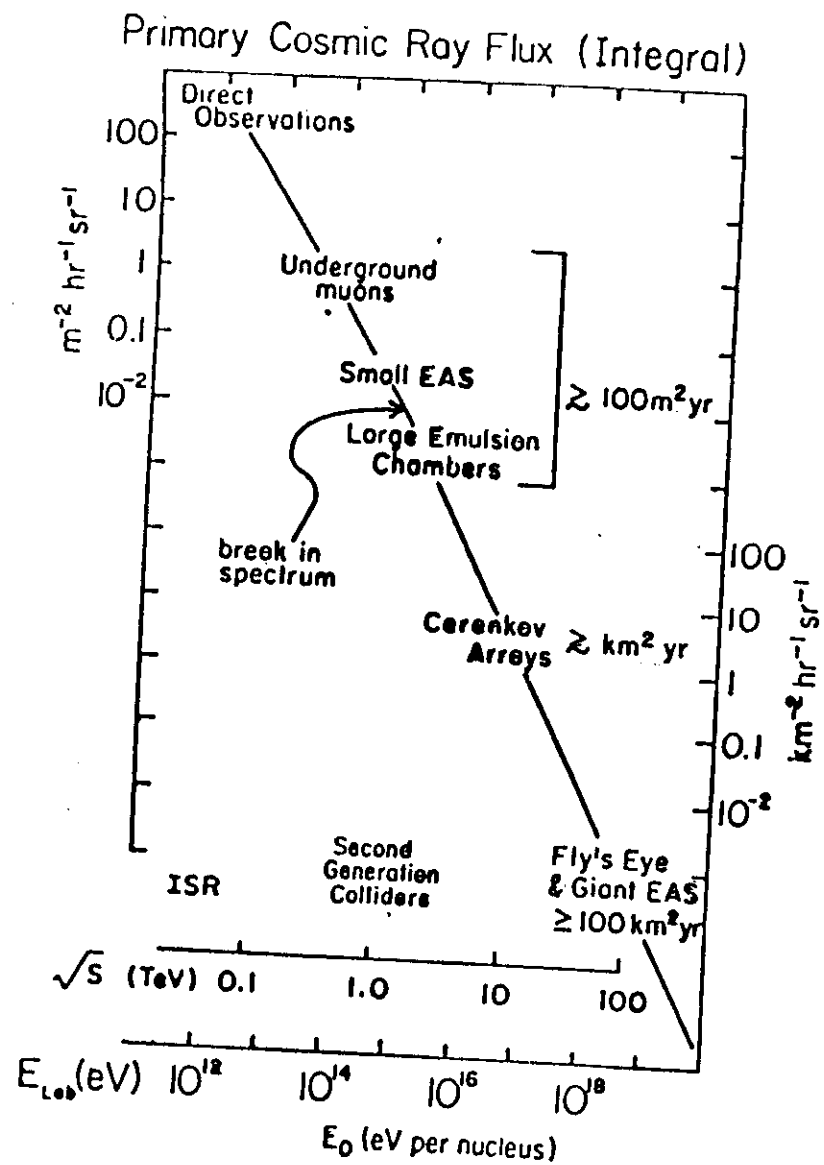


FIG. 1

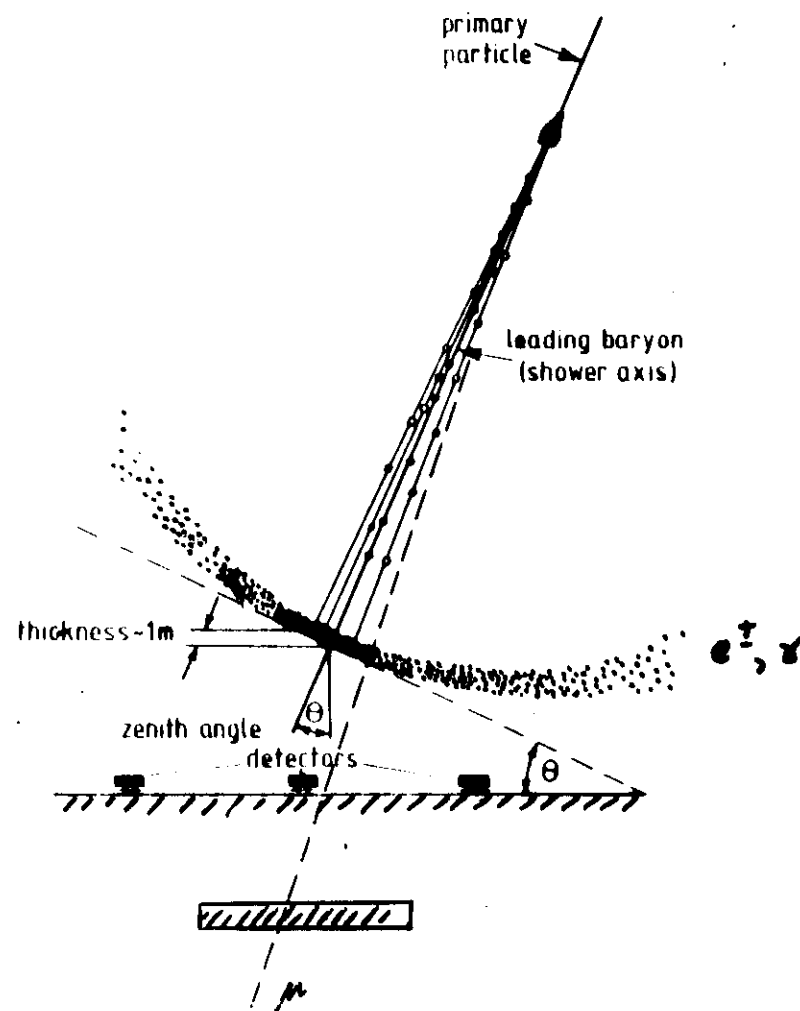




Fig. 6. The atmospheric Cherenkov Gamma-Ray Telescope with 10 m diameter at the Whipple Observatory in southern Arizona

night-sky background the phototubes used in atmospheric Cherenkov telescopes draw large currents. In general, the use of filters has not made a dramatic improvement in the detector sensitivity.

Grindlay [30] used a technique which had two detectors, one with sensitivity in the ultraviolet, the other in the visible. Because of its penetrating muon component, the UV channel was expected to be more sensitive to background hadrons. However, the method of discrimination by ultraviolet versus visible is currently being exploited at the Crimean Astrophysical Observatory [31].

(e) *Field of view.* The optimum field of view is determined by the angular size of the shower light image and the displacement of the centroid of the image from the center of the detector field of view as the impact parameter increases. To maximise the gamma-ray collection area the field of view should be as large as possible. However, this also increases the energy threshold, since more night-sky light is accepted. In practice, most detectors have had half-angles in the range 0.25° to 2.5° . Recent Monte Carlo simulations and image size measurements [32–35] have indicated that the shower image size is typically 0.4° (FWHM), which is somewhat smaller than had been previously supposed.

The field of view used in a practical detector is defined by the size of the phototubes used and the scale of the focal plane. In some cases the field is defined by an aperture and widened to illuminate more than one phototube, or narrowed to concentrate the light on the center of the photocathode.



• Detector Noise $N \sim (\epsilon B A \Omega t)^{1/2}$ where

$\epsilon \sim$ light to photoelectron conversion eff

$B \sim$ background

$A \sim$ collecting area

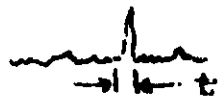
$\Omega \sim$ Solid angle of detector $\sim \pi \theta^2$

$t \sim$ receiver integration time

• Signal $S \sim \epsilon A$

assuming it arrives as a burst

- Signal/Noise $SN \sim (\epsilon A / B \Omega t)^{1/2}$



t should be large enough
to capture signal - but
no larger!

- maximize ϵ, A
- minimize Ω, t

- Energy Threshold

$$E_{thr} \propto 1/SN \sim (B \Omega t / \epsilon A)^{1/2}$$

- For Cherenkov Detectors - maximizing SN
lowers energy threshold

- Flux Sensitivity - a more important
consideration

* Signal Events $S_r = F_r \cdot A \cdot T$

signal flux · collecting area · observing time

* Background Events $S_b = I(>E_{thr}) \cdot A \cdot \Omega \cdot T / r$
cosmic ray flux · area · solid angle · time / "rejection"

- $N_r = F_r (r A T / I(>E) \Omega)^{1/2} = S_r / S_b^{1/2}$

Source and Background Flux?

$$F_r \sim E_r^{-\Gamma}$$

$$\Gamma \sim 1 ??$$

$$I(>E_b) \sim E_b^{-1.55}$$

$$1 \text{ TeV} \sim 1 \text{ PeV}$$

note $E_r \sim 0.3 E_b$

$$\rightarrow E_b \text{ at } E > 1 \text{ PeV}$$

$$N_r \sim E^{0.8-\Gamma} (r A T / \pi)^{1/2} / \delta \theta$$

Detectable sources eg Cyg X-3 seem
to have flat spectra

$$F_r = a E^{-1} ; a \sim 100 \text{ eV cm}^2 \text{ s}^{-1}$$

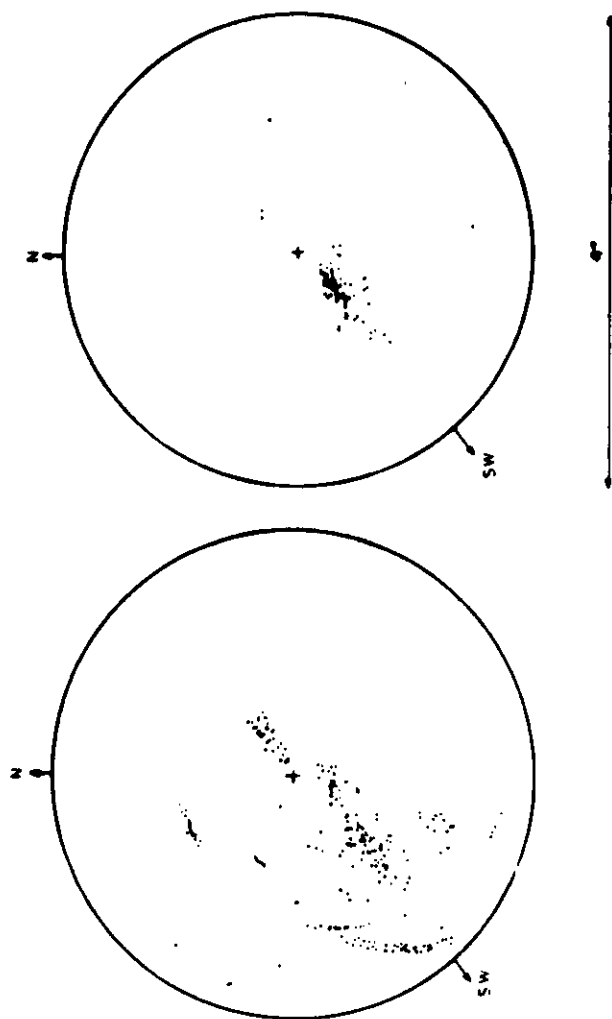
- Define: Σ_i = energy flux = $E F_r$ ($= a$)

Note: $I(E) = 10^{-10} (E/2 \text{ PeV})^{-\delta}$ $\delta = 1.55 \text{ } E < 2 \text{ PeV}$

$$\delta = 2.1 \text{ } E > 2 \text{ PeV}$$

$$\Sigma_i (\text{eV cm}^2 \text{ s}^{-1}) = \frac{3 \cdot 10^{10} \delta \theta \cdot N_r \cdot E^{2.3}}{(r A T)^{1/2}}$$

eg/ Whipple reports 90° Crab observation
at $F_r = 1.8 \cdot 10^{-11} \text{ cm}^2 \text{ s}^{-1}$, and $E > 0.7 \text{ TeV}$
 $\Sigma_i \sim 12.6 \text{ eV cm}^2 \text{ s}^{-1}$



(a) PROTON (1 TeV)

(b) GAMMA RAY (320 GeV)

Fig 10 The distribution of Cherenkov photons in the $5'$ full field of a 30 m optical reflector from an air shower whose trajectory is parallel to the optical axis of the reflector. (a) for a 1 TeV muon beam primary falling 45 m southeast of the telescope and (b) for a 320 GeV gamma ray at the same location. The short arcs in the nuclear picture are segments of Cherenkov rings from local muons in the air shower (from Monte Carlo simulations by A. M. Hillas [33]).

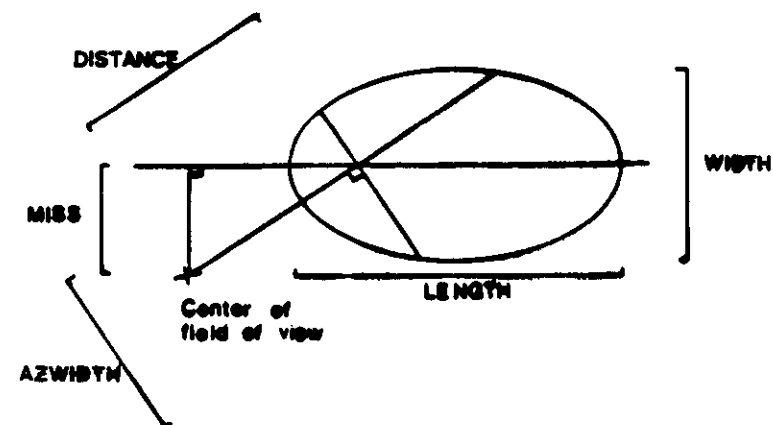


FIGURE 12

13

COMPARISON OF SIMULATED AND MEASURED PARAMETERS

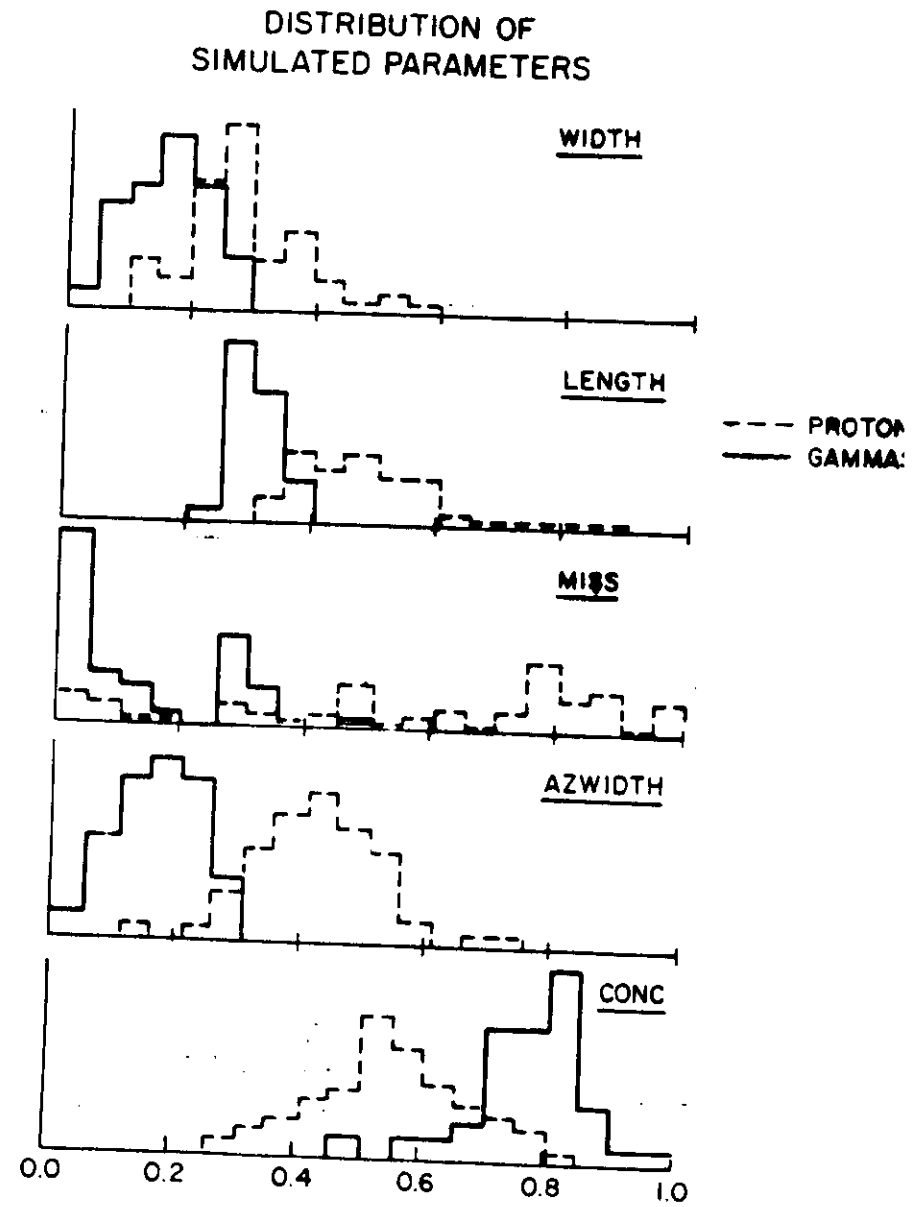


FIGURE 13

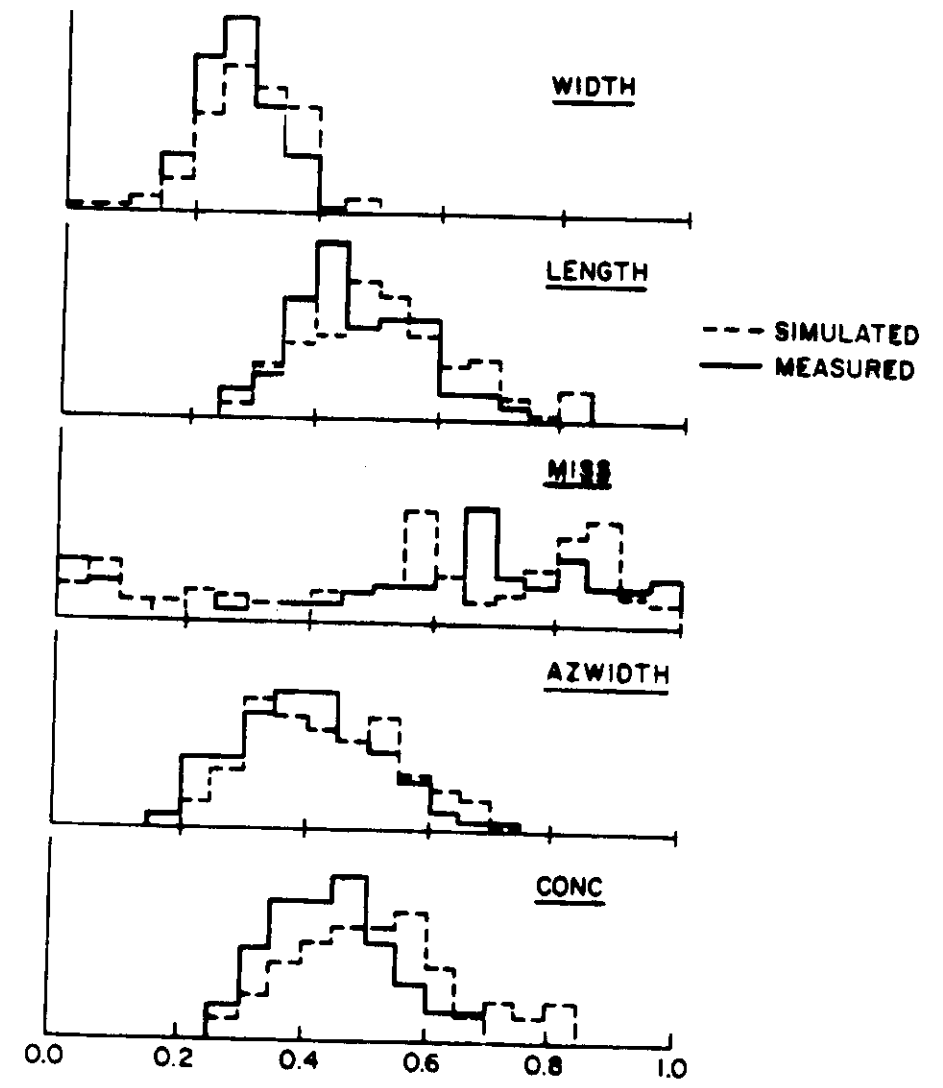


FIGURE 14

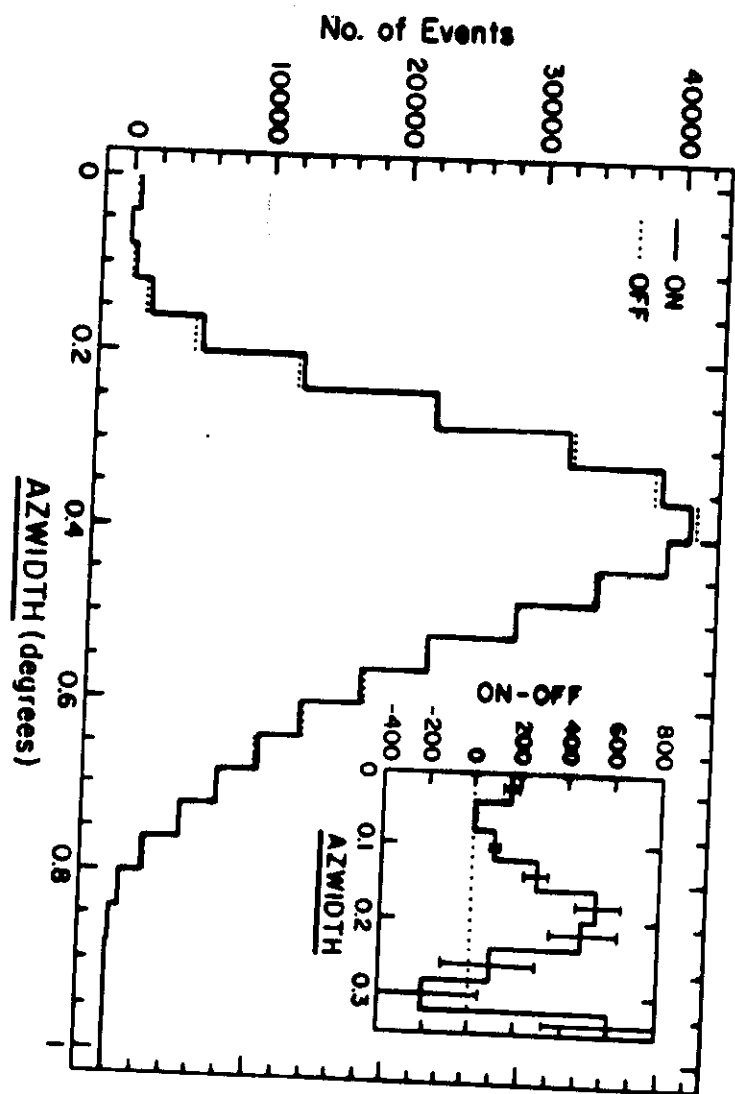


FIGURE 15

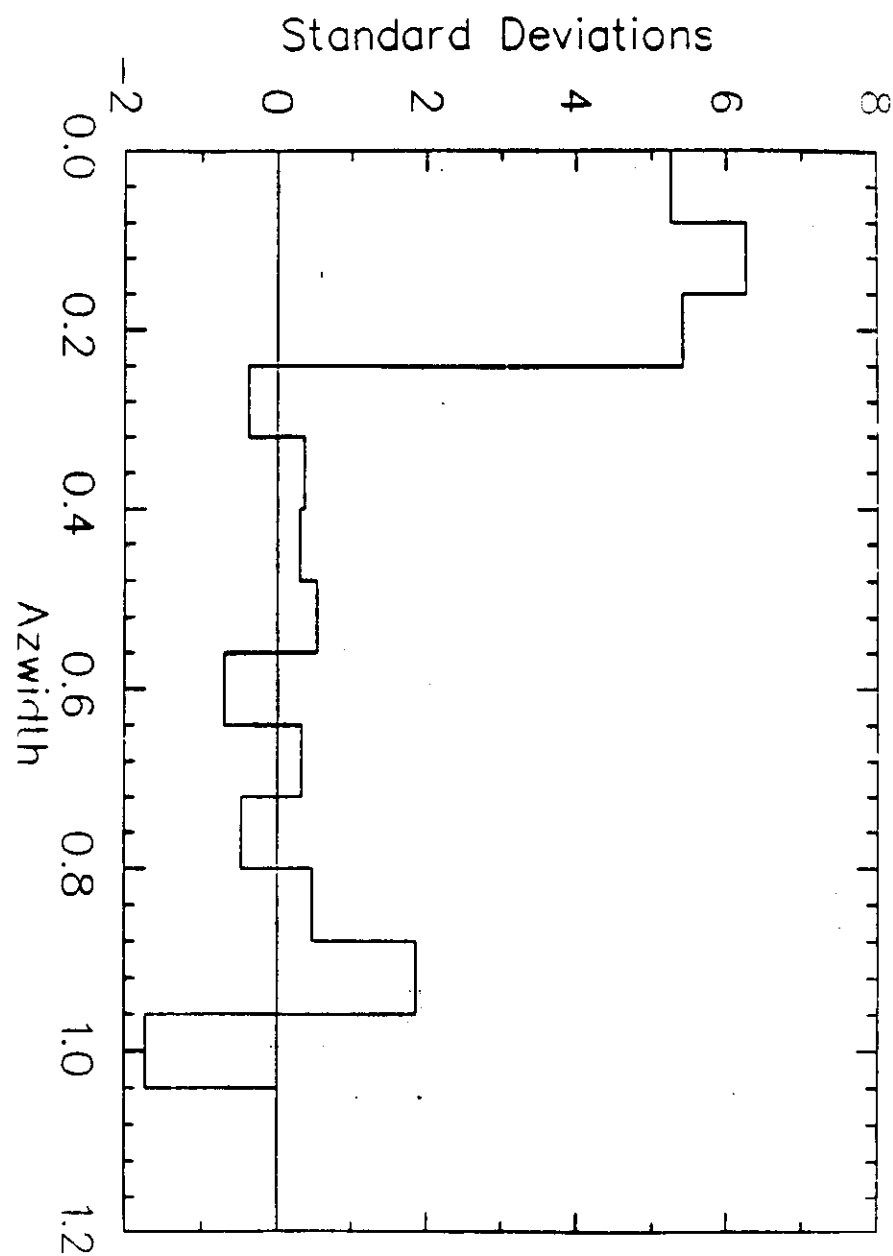
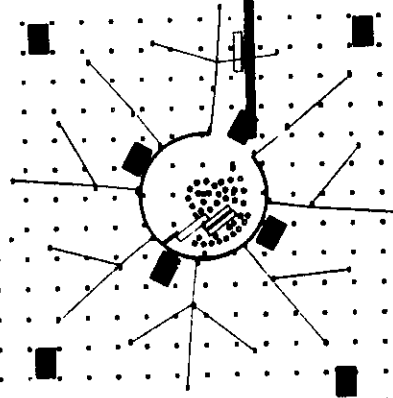


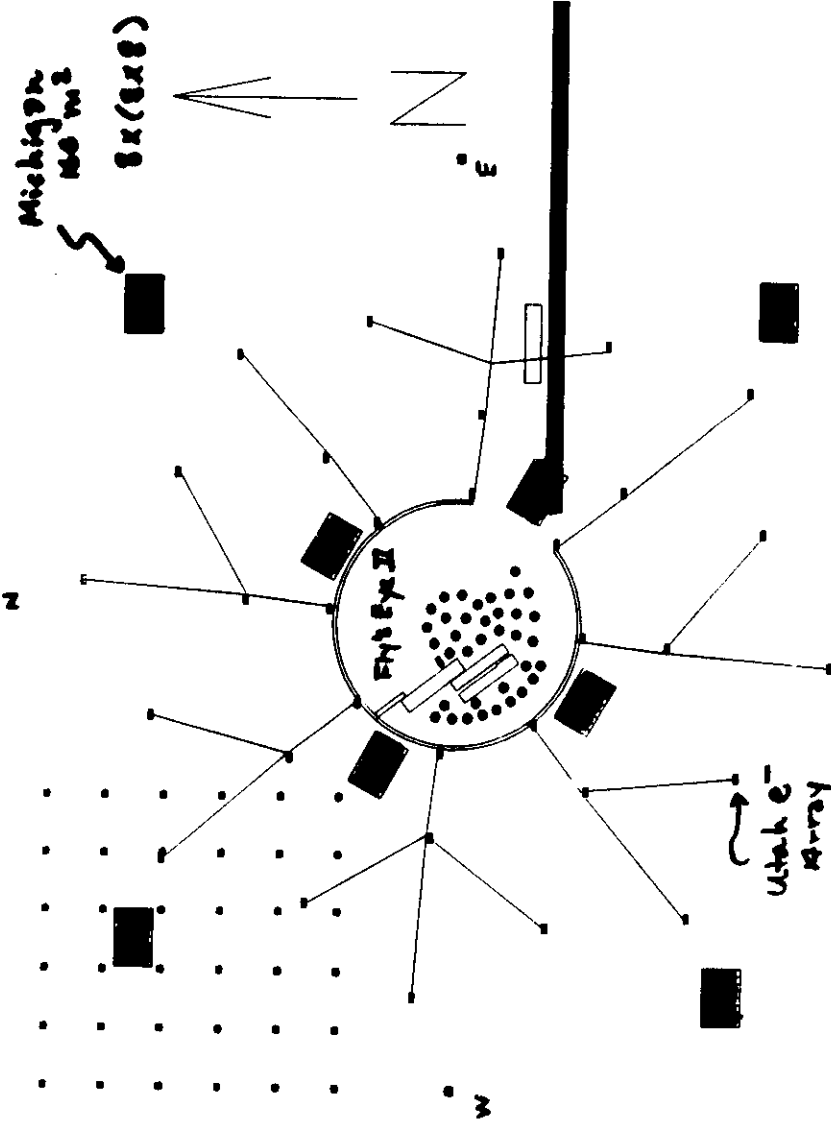
FIGURE 16

Case
 ~1000 cm²
 500 m x 500 m
 Michigan
 16 "patches"
 2400 m²



Case 7x7

15m →

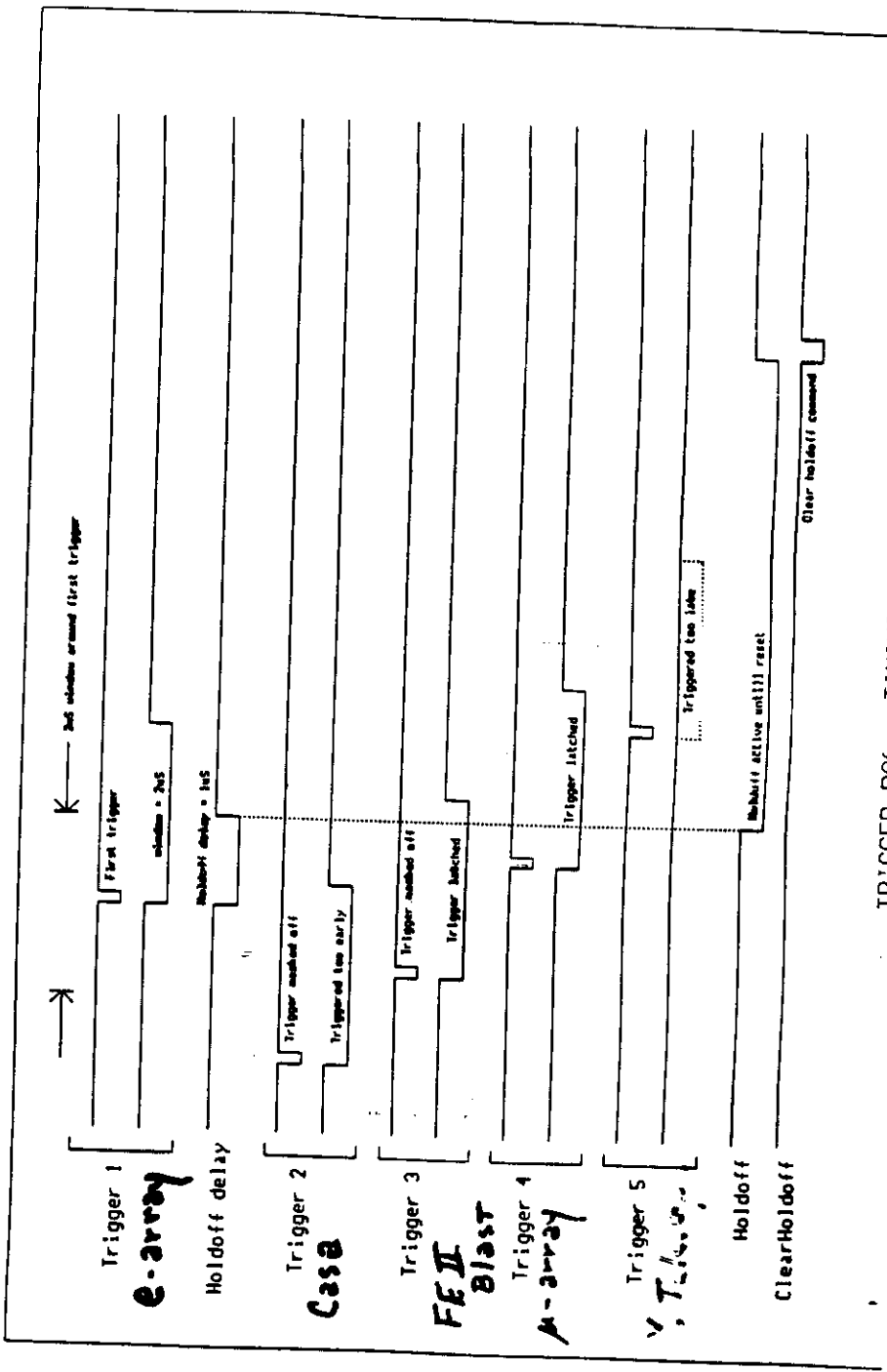


Utah Telescope

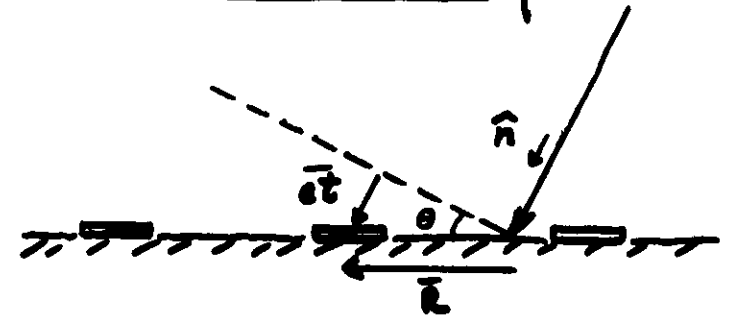
Utah Array
 38 (4)

Trigger: OR of non-masked possibilities

also FEI, E "Track mode" recorded



Shower Geometry



$$\hat{n} \cdot \vec{R} = \hat{n} \cdot \hat{ct}$$

$$0 = n_x(x - n_x ct) + n_y(y - n_y ct) + n_z(z - n_z ct)$$

$$\text{But } n_x^2 + n_y^2 + n_z^2 = 1 \quad \text{so}$$

$$\underline{n_x x + n_y y + n_z z = ct}$$

- Usually experimenters measure (\vec{R}_i, t_i) and fit to above expression
- CASA notes $\frac{c \Delta t}{\Delta R} = \sin \theta$
- only time differences needed

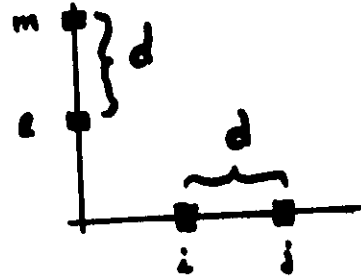
Let t_i be time station i (x_i, y_i, h_i) struck
 $n_x x_i + n_y y_i + n_z h_i = ct_i$

Similarly - if station j at $(x_j, 0, h_j)$
struck at t_j - we have

$$n_x x_j + n_y h_j = c t_j$$

Subtracting

$$n_x = \frac{[c(t_i - t_j) - n_y(h_i - h_j)]}{(x_i - x_j)}$$



We can now make the same argument
for boxes along the y -direction
at "coordinates" $(0, y_i, h_i, t_i)$
 $(0, y_m, h_m, t_m)$

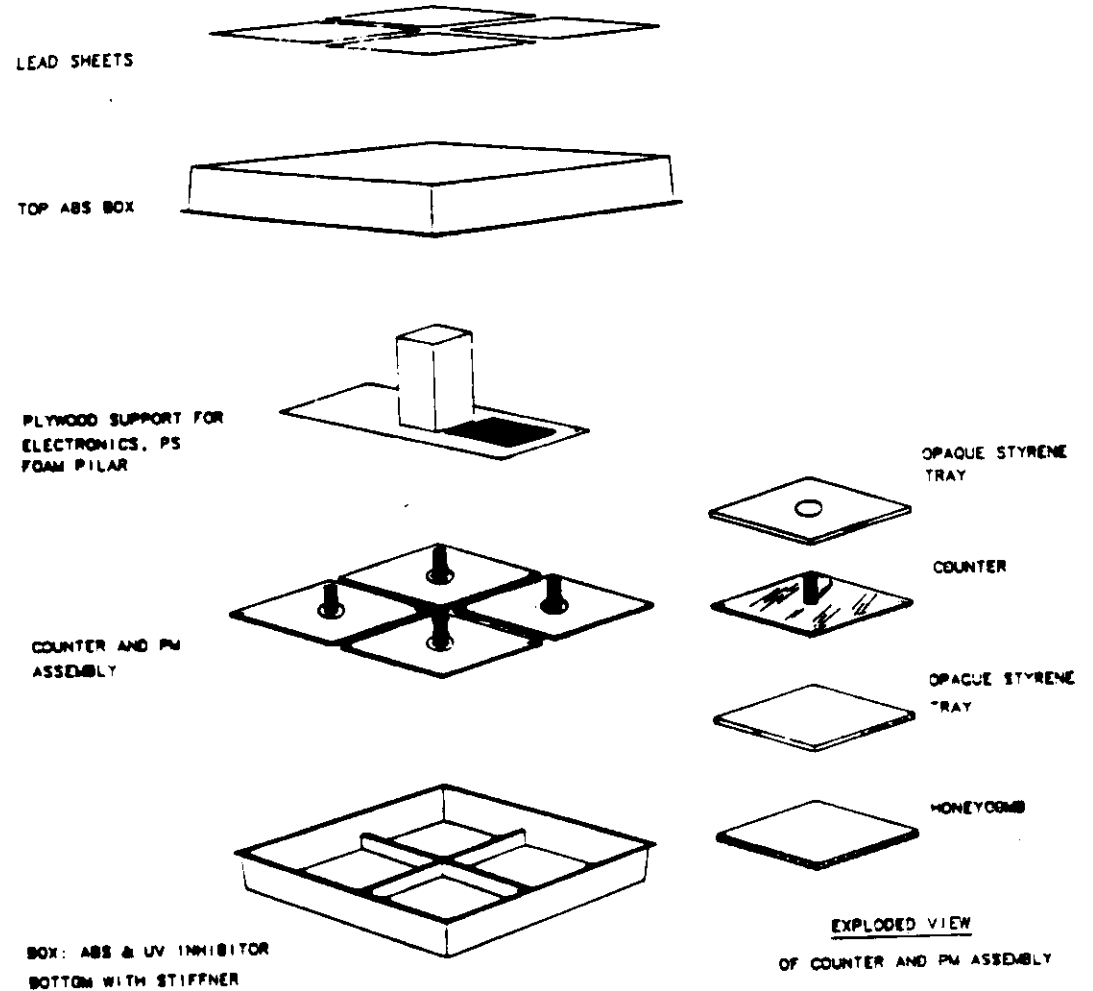
noting that $x_i - x_j = y_i - y_m = d$

$$n_x = [c t_{x_i}^i - n_y(h_i - h_i)] / d$$

$$n_y = [c t_{y_i}^m - n_x(h_i - h_m)] / d$$

where $t_{x_i}^i$ and $t_{y_i}^m$

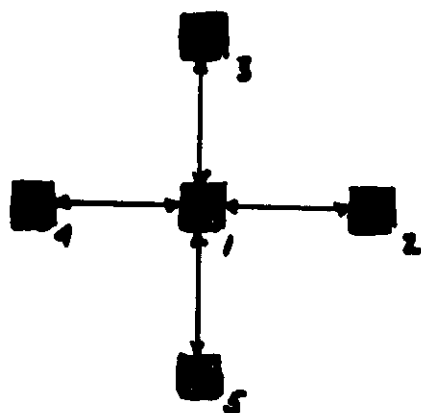
are time differences in x and y
directions between "linked" stations



EXPLODED VIEW OF CASA DETECTOR

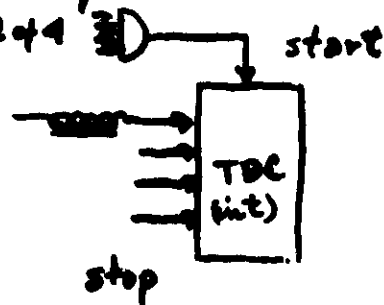

FIG 29

HOW LATAA WORKS



When station 1 "struck" its TDC starts "struck" means alerted by 2 out of 4 counters

All 4 (n2,3) delayed hits stop their respective TDC. If T_i is time of earliest hit and A_i is time of station start (2 of 4 coincidence)



$$\overset{\text{measured}}{\tau_i} = T_i - A_i + \underset{\text{offset}}{\delta_i}$$

Station 1 sends alerts to 2, 3, 4, 5!
Stations 2-5 " " to 1

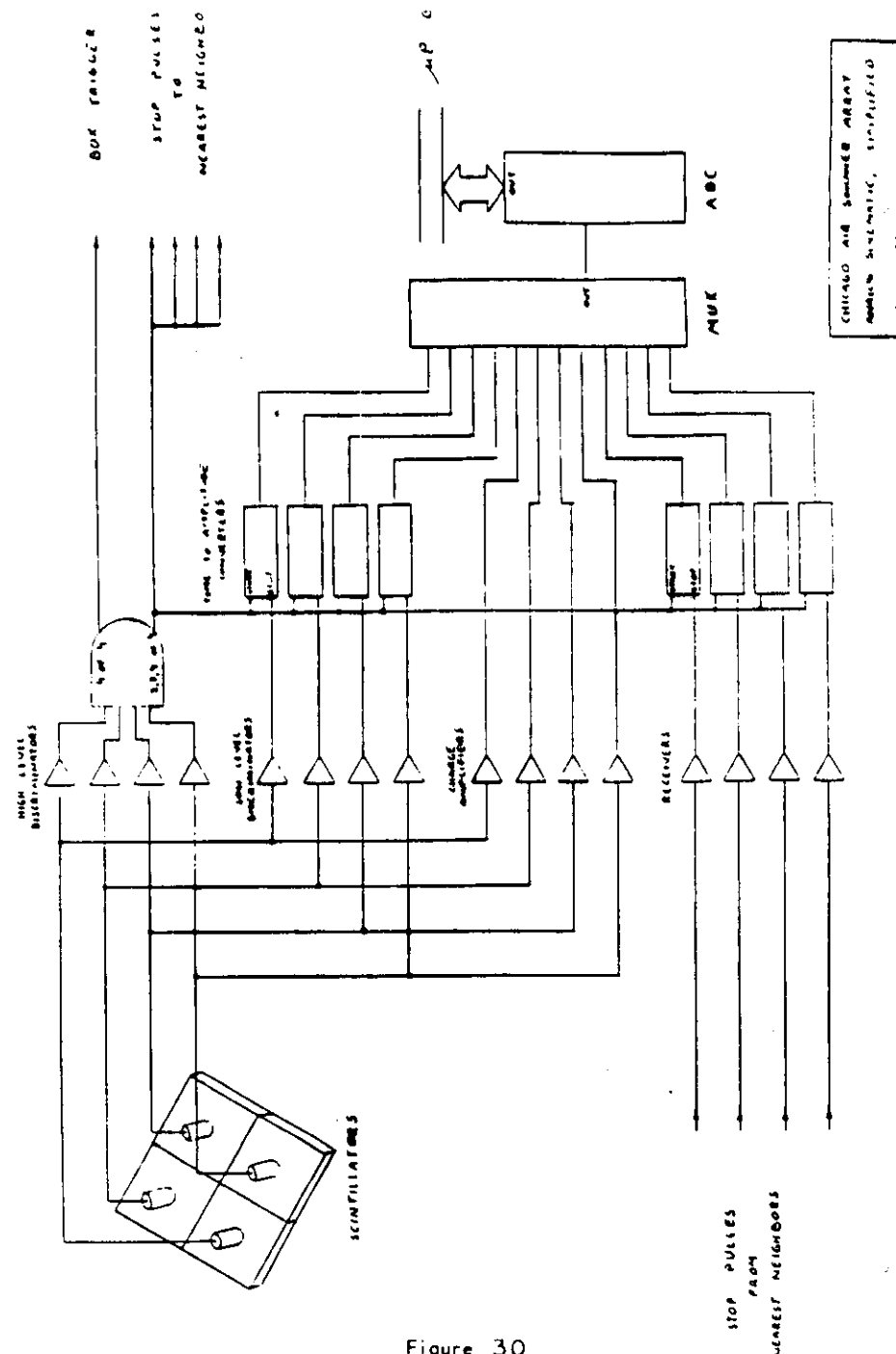
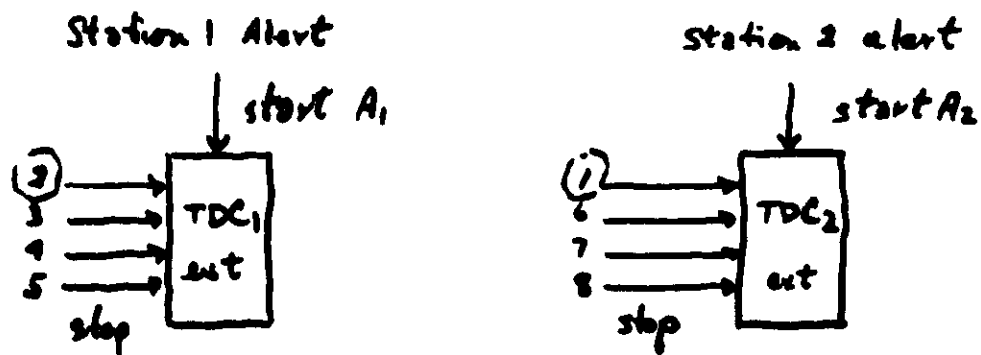


Figure 30

Station 2-5 Measurements



Thus if 2 neighbors alerted they stop the TDC's in each other thus giving external times τ_{ij} and τ_{ji}

$$\tau_{ij} = A_j - A_i + \delta_{ij}$$

• Arrival Time differences are thus

$$\tau_{ij} = (\tau_i - \tau_j) + (\tau_{ji} - \tau_{ij})/2 - O_{ij}$$

where $O_{ij} = (\delta_i - \delta_j) + (\delta_{ji} - \delta_{ij})/2$

• Use weighted average of these time differences to get direction cosines

$$n_x = \sum_{\substack{i,j \\ \text{pairs}}} [c \tau_{k,i,j} - n_z(h_i - h_j)] W_{ij} / d \sum W_{ij}$$

$\langle n_z \rangle = 0.91$

• Weights W_{ij}
total # particles which passed through i, j

• n_z
We are trying to determine n_z
How use it?

i) Use average n_z all data $\langle n_z \rangle \sim 0.91$

ii) Iterate - starting with $\langle n_z \rangle$
computationally intensive
no difference noted - yet.

• Offsets (cable, circuit delays, etc)

Note $\langle n_x \rangle = \langle n_y \rangle = 0$

$$O_{ij} = \langle (\tau_i - \tau_j) + (\tau_{ji} - \tau_{ij})/2 - n_z(h_i - h_j)/c \rangle$$

• Pedestals ~ single particle \Rightarrow
average pedestal subtracted
pulse heights when only 2 counters
fired / station

• Slowing - measure and correct!
set $\tau_t = f(\text{pulse height})$

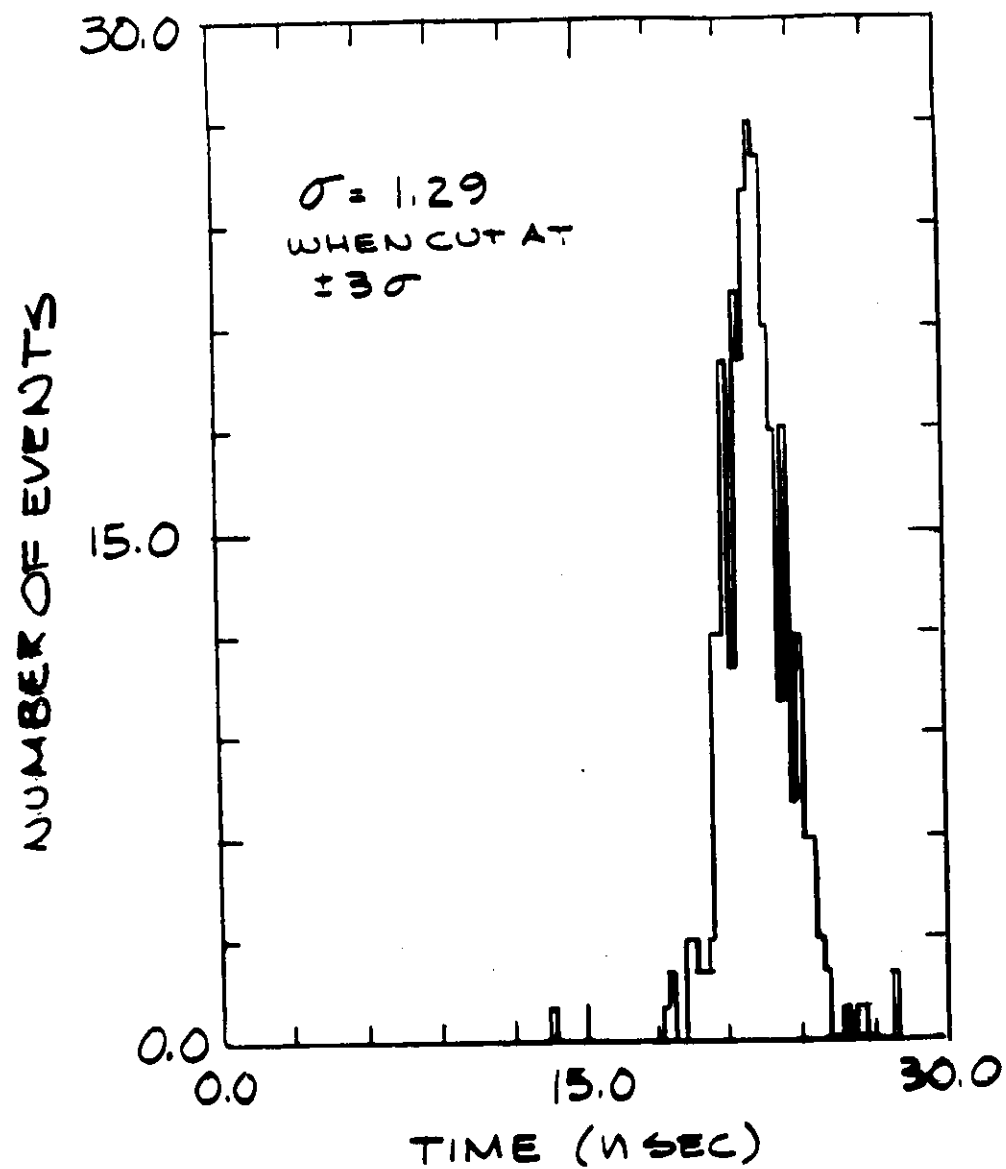


Figure 31

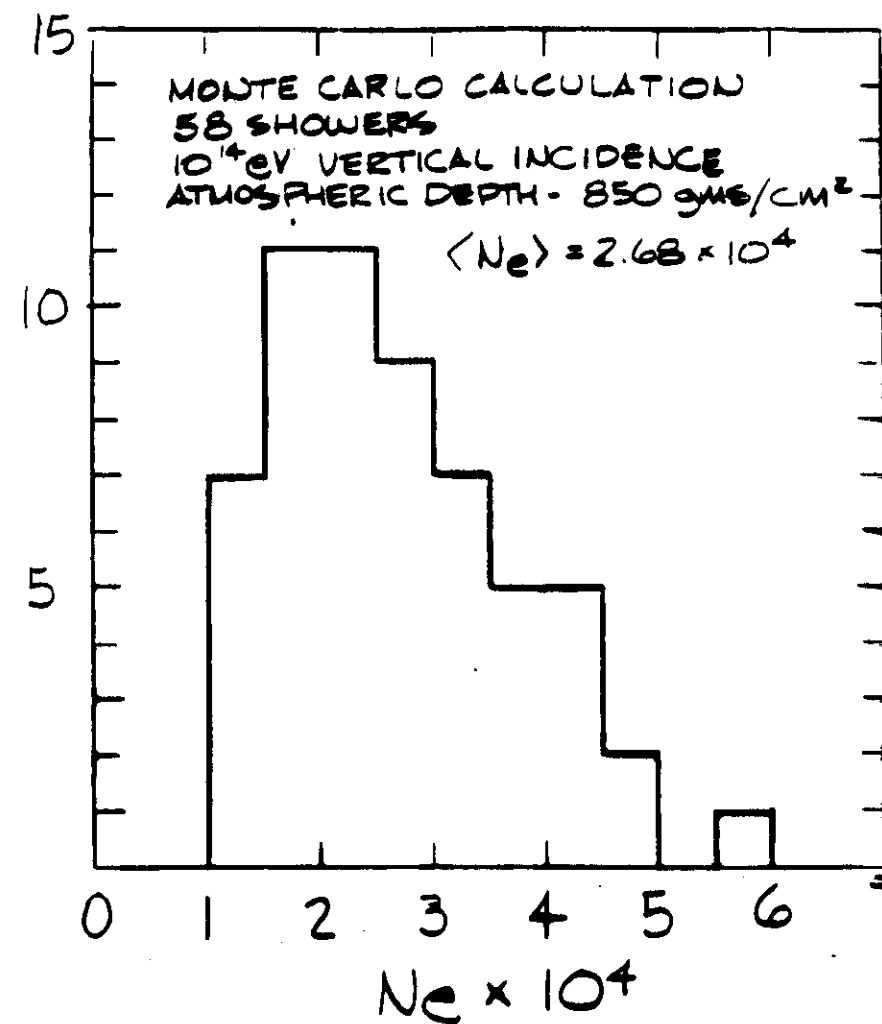
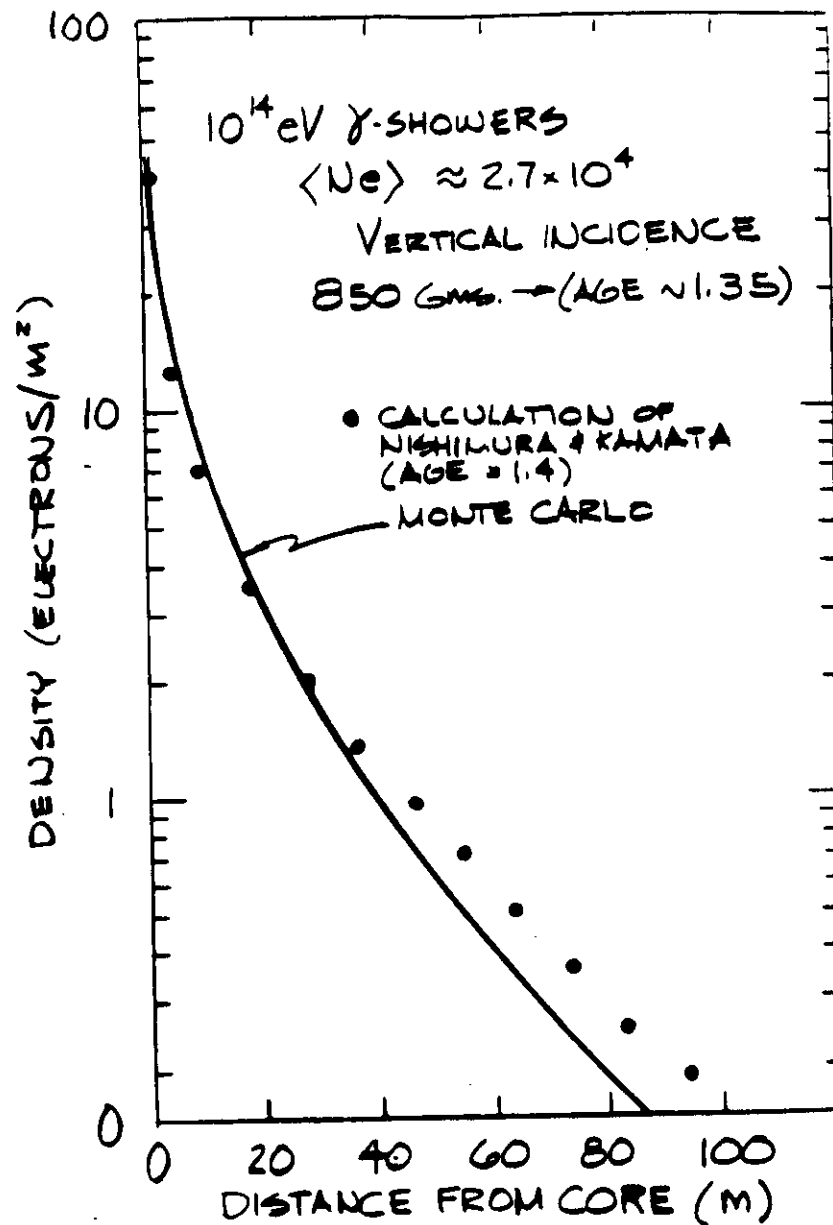
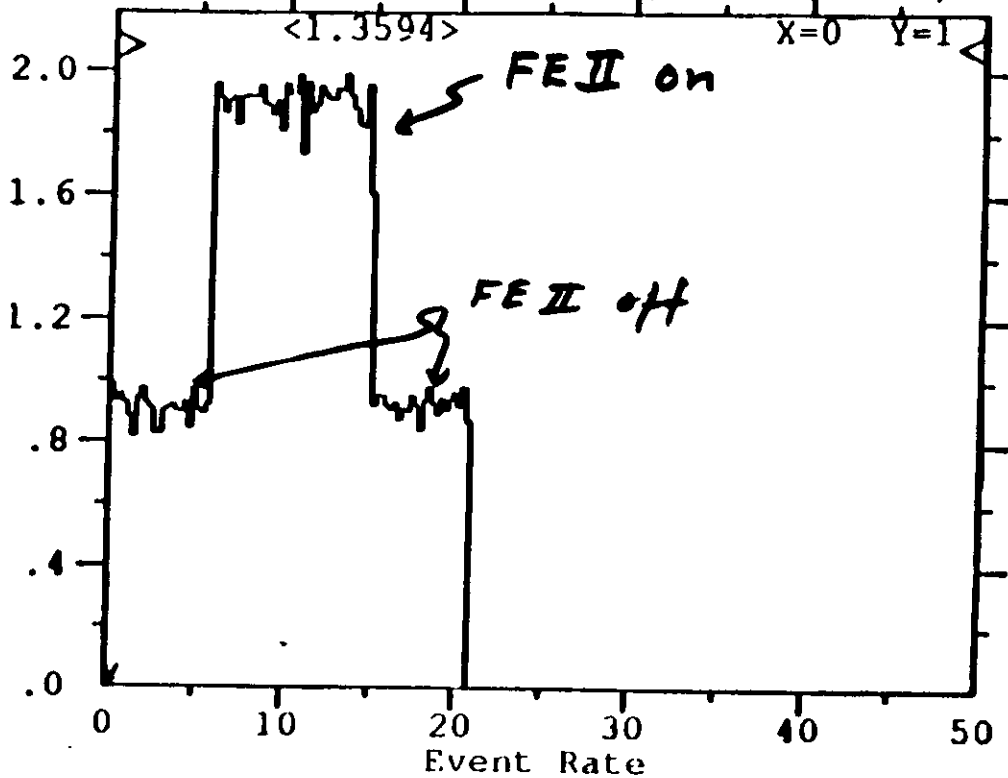


Figure 18

RUN 331 17-MAR-88 14:18:20
 #CALLS= 0 6785 0 (UND HIST OVR)

<1.3594>

X=0 Y=1



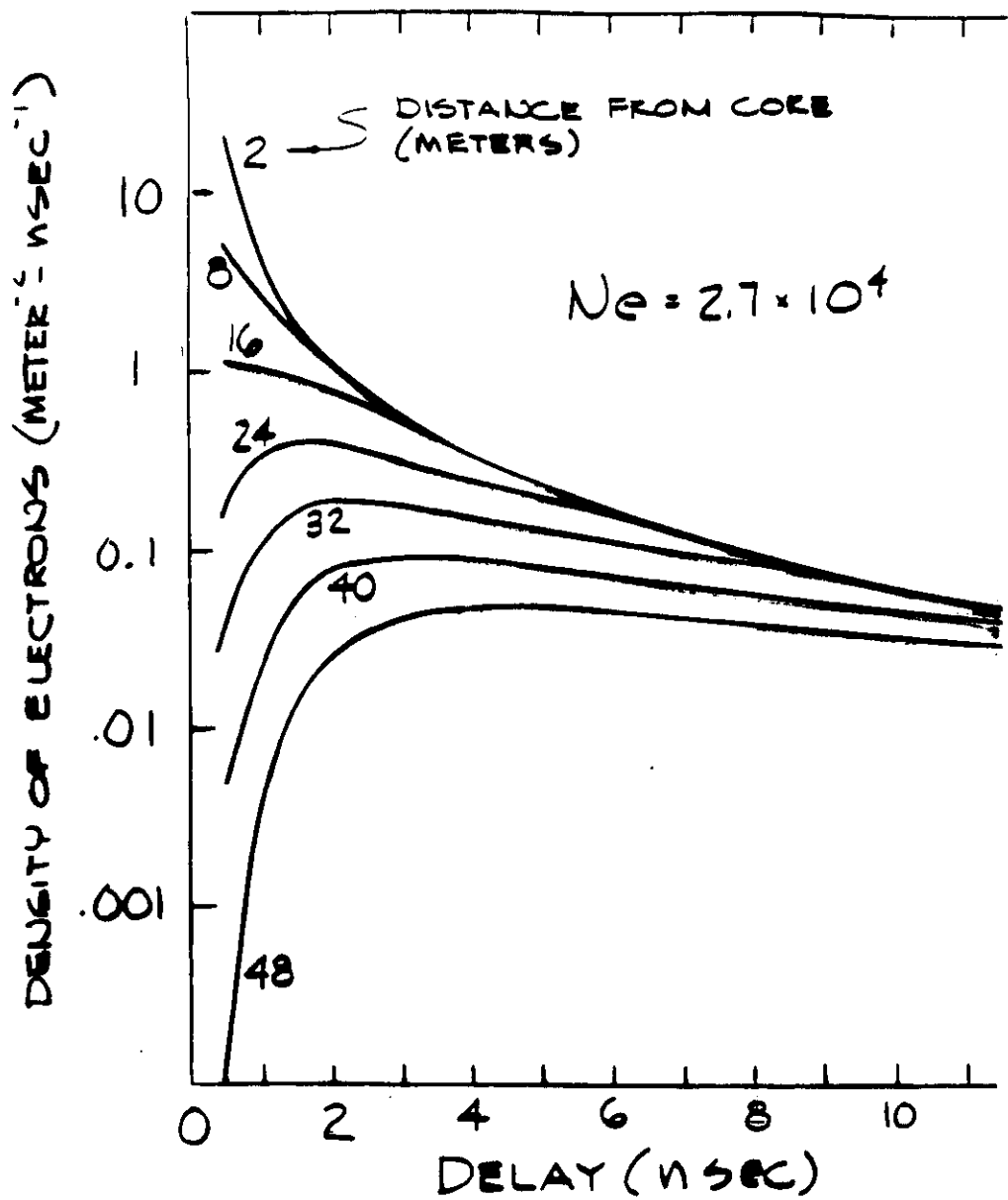


Figure 20

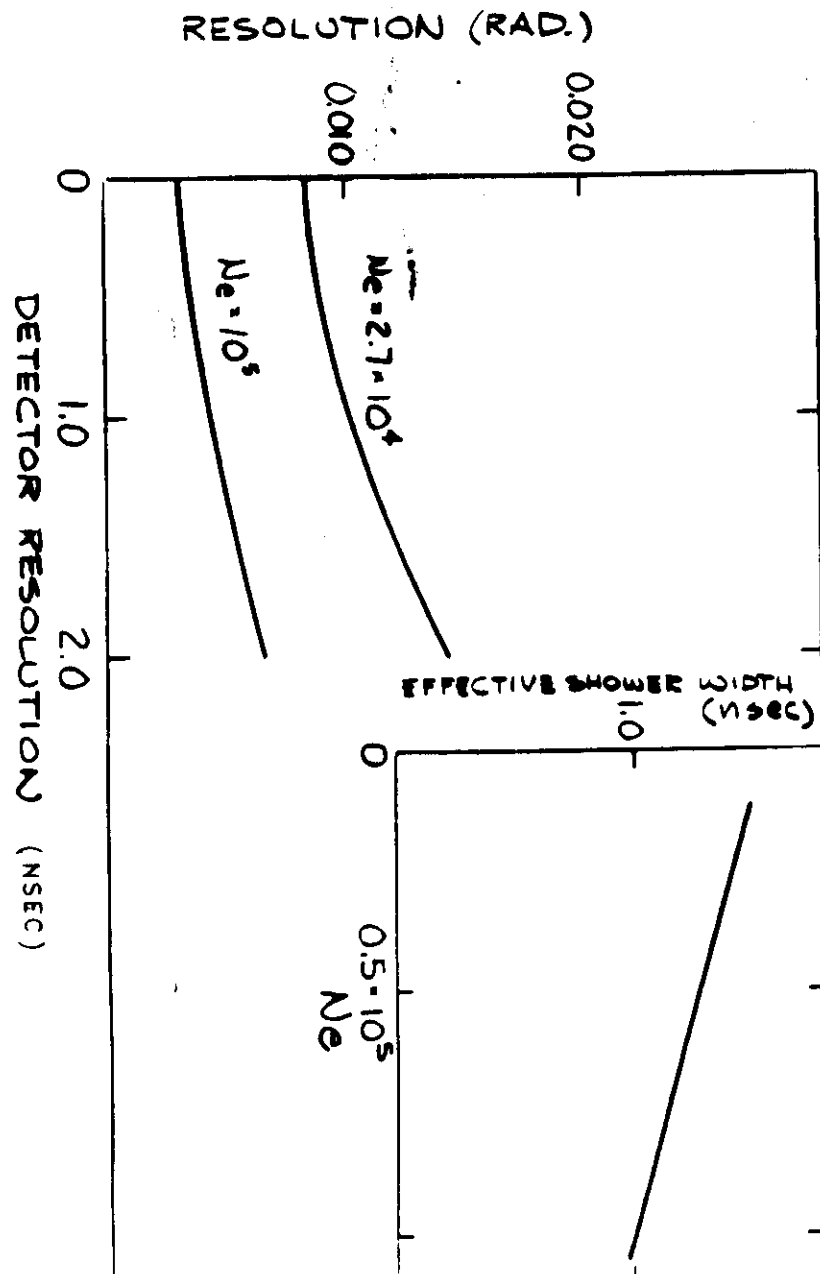


Figure 21

Figure 22

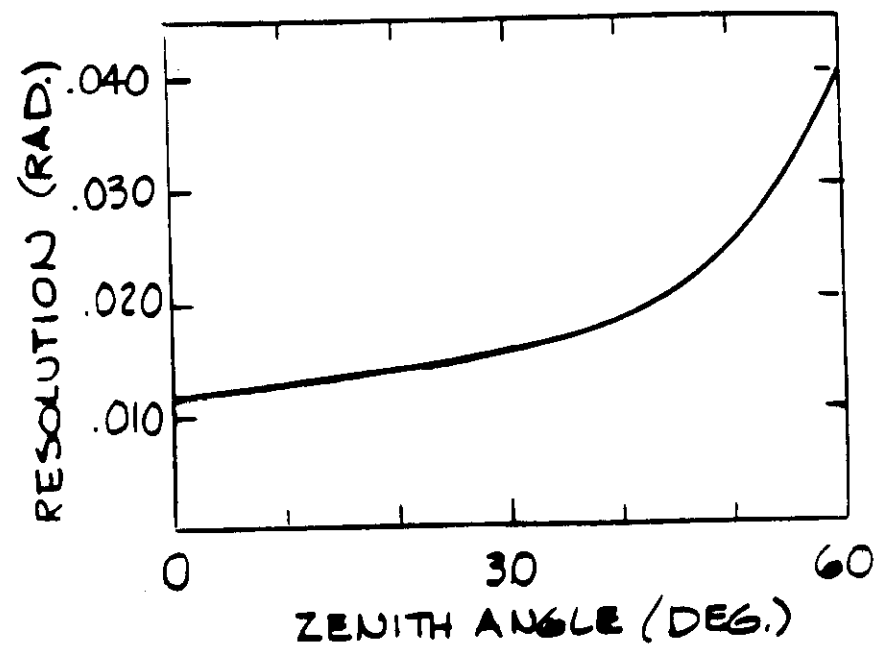
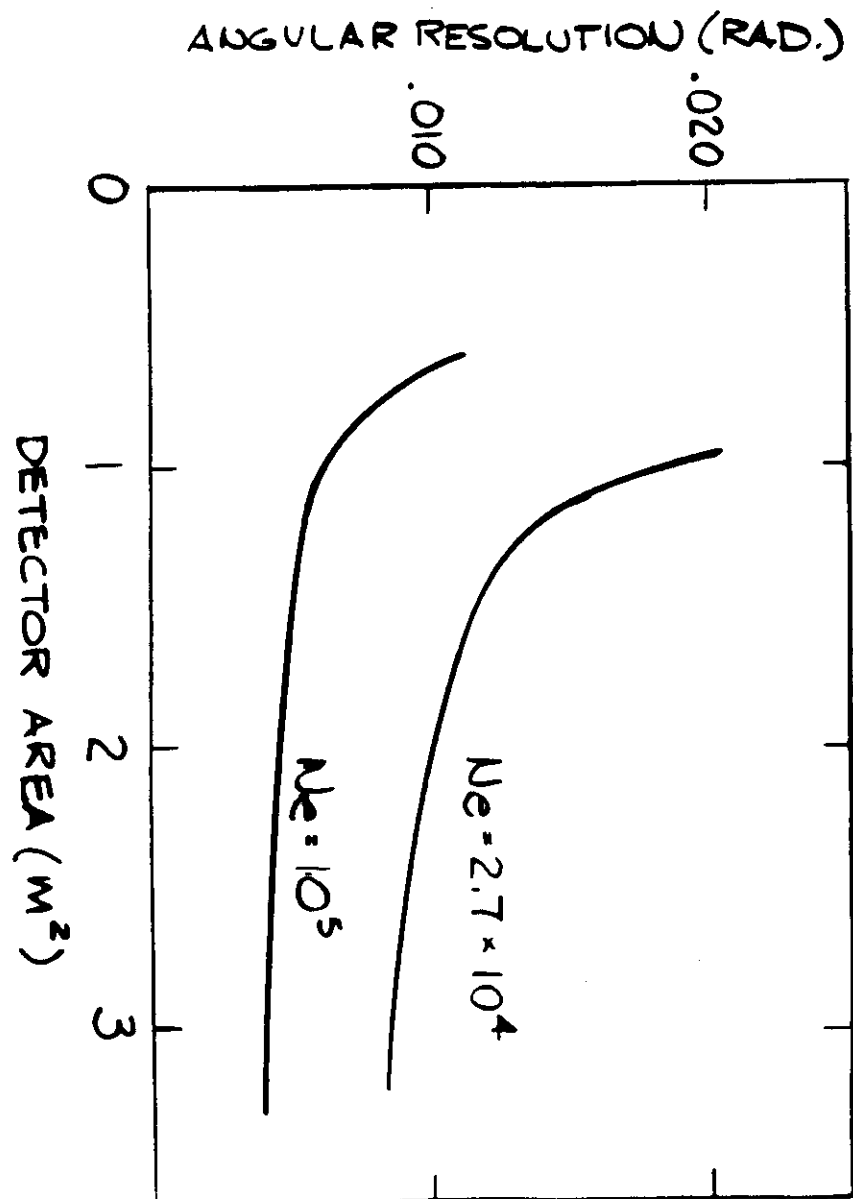
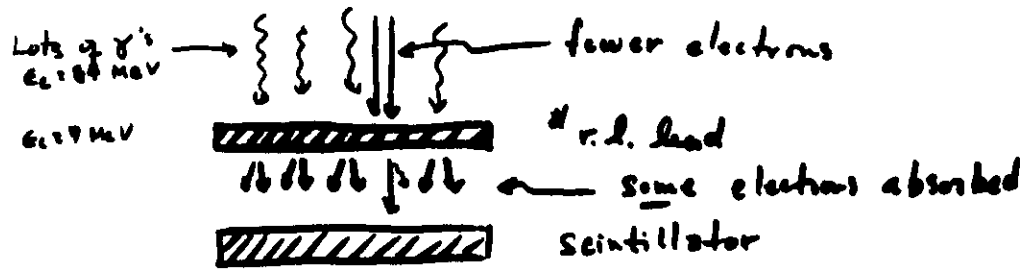


Figure 23

Improving Angular Resolution

Add Layer of Lead Above Counters



- 1) More particles hit scintillator
 - 2) Narrower time spread
- butten 80 typically $\rightarrow \frac{80}{20}$

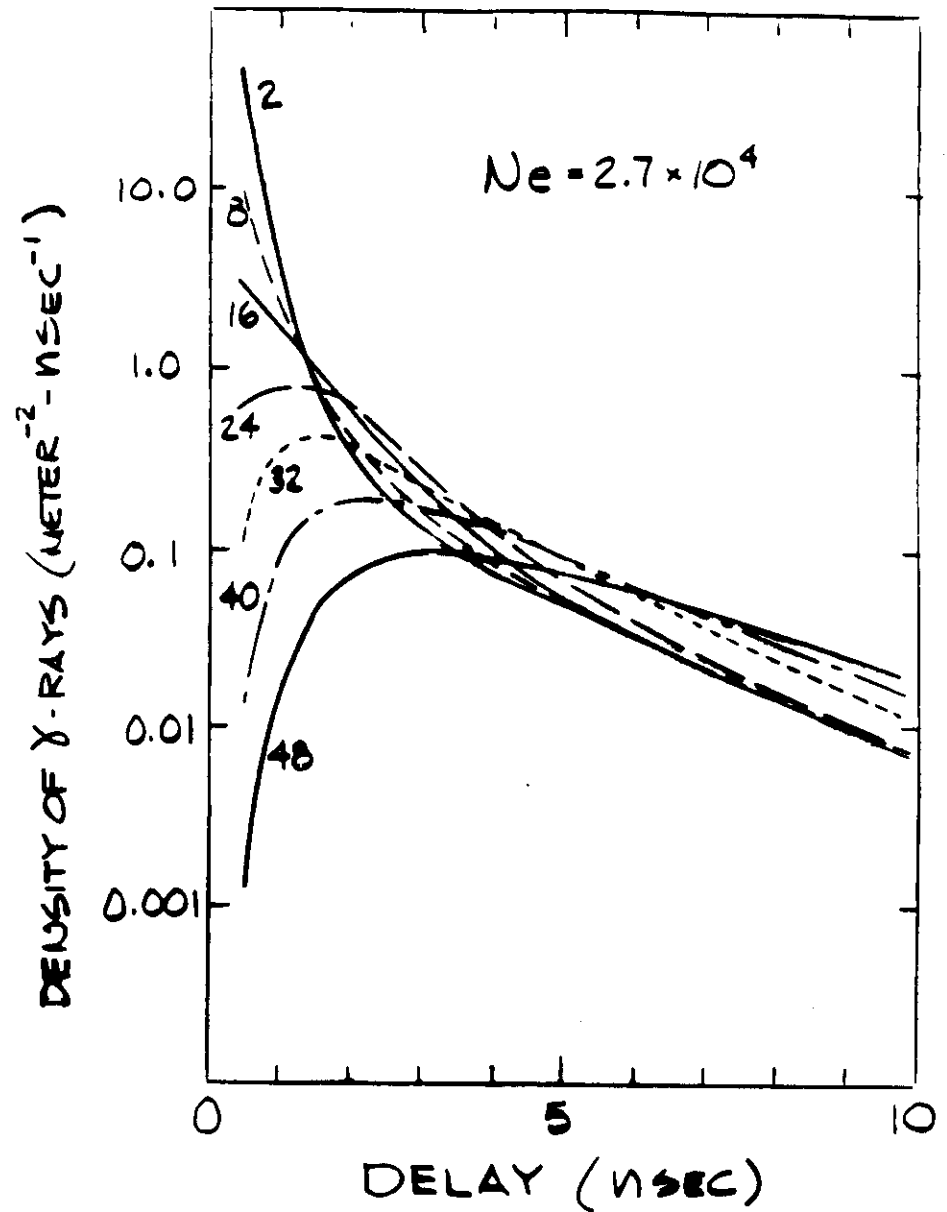
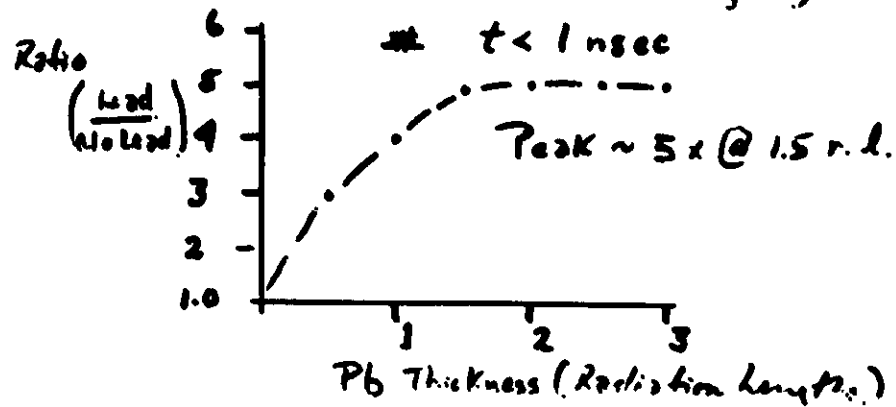
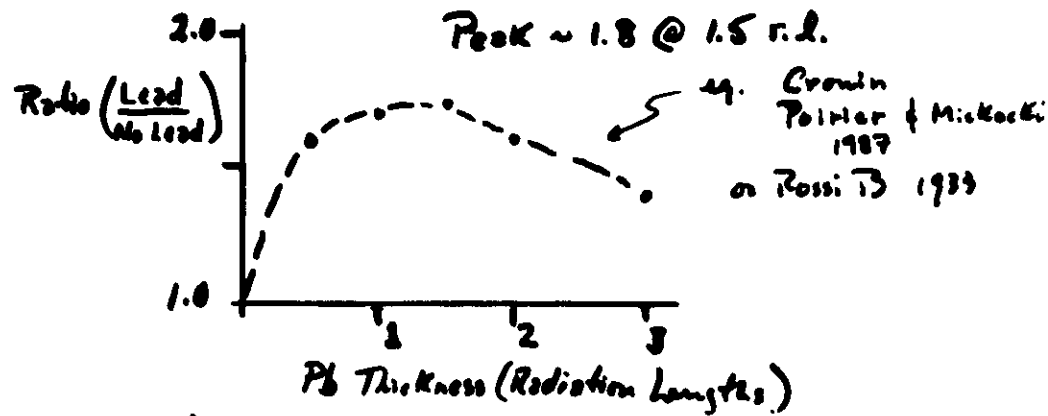


Figure 24

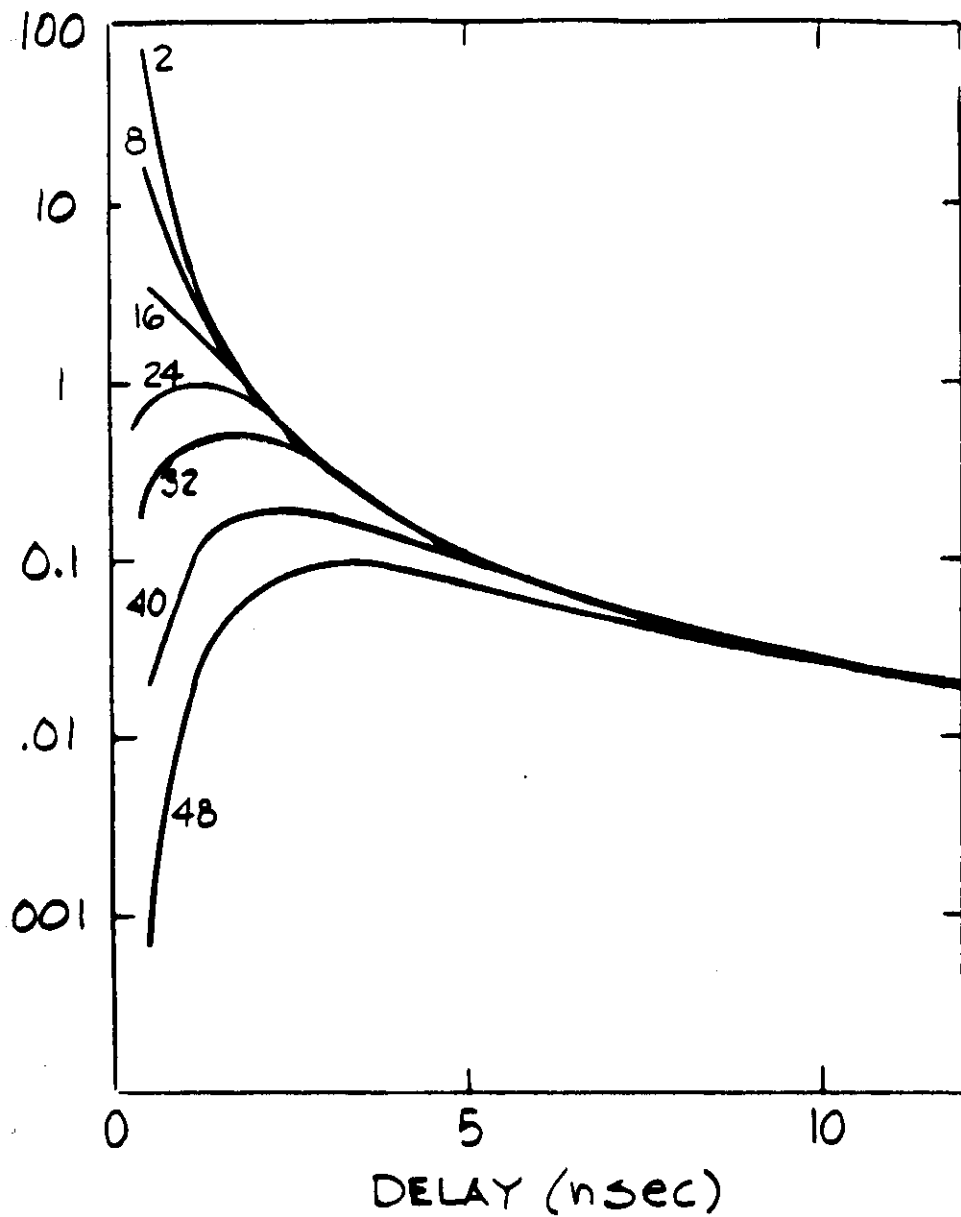
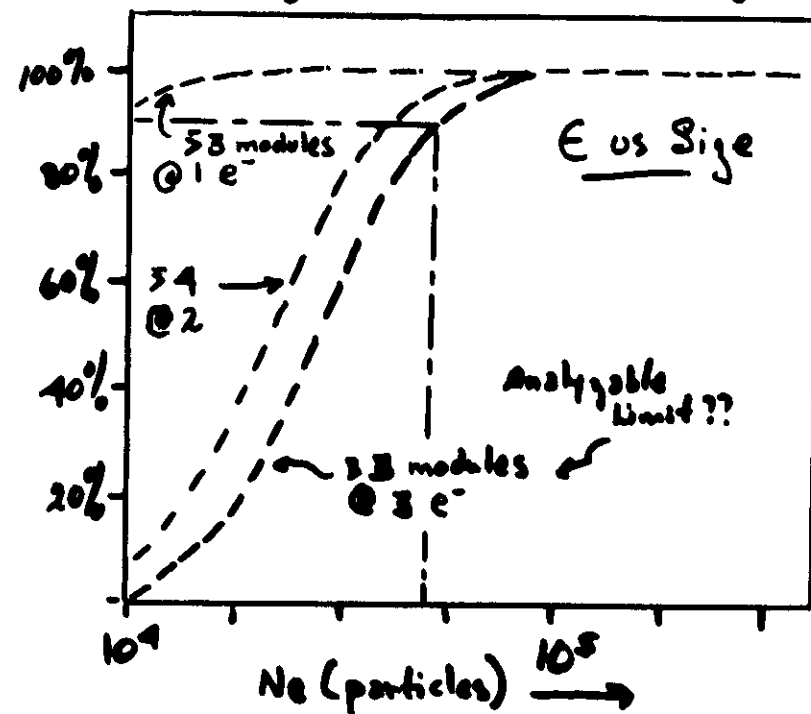


Figure 25

Surface Array Threshold

- Dugway, Utah Altitude (860 g cm^{-2})
 $\rightarrow \sim 2.5 \times$ # particles at Sea Level
- Threshold determined by detector spacing and requirement of Analyzability



90% E @ $10^{4.7}$ (50,000 particles)

Cascade Theory $\Rightarrow E_r \approx 0.4 \text{ PeV}$

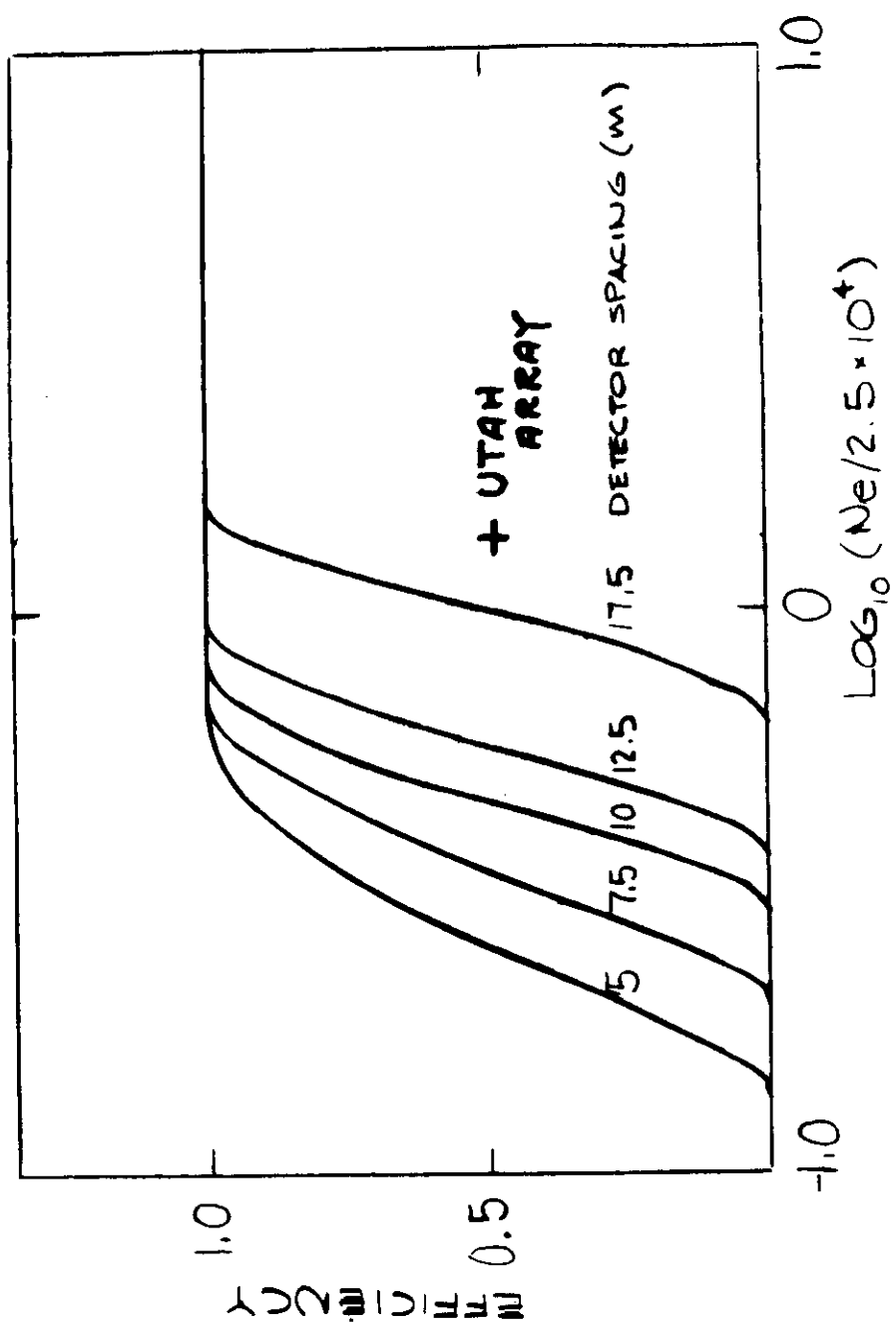


Figure 26

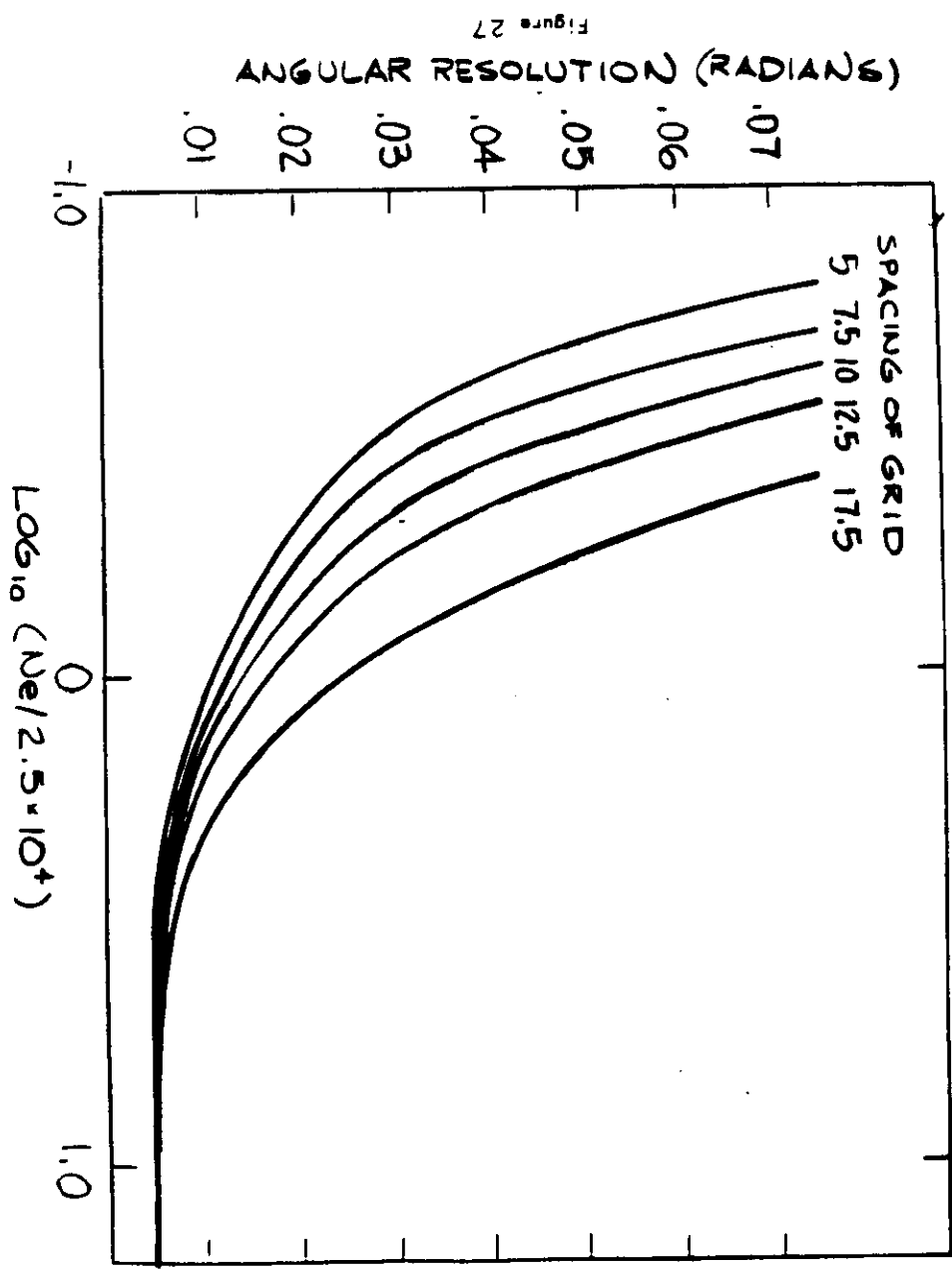
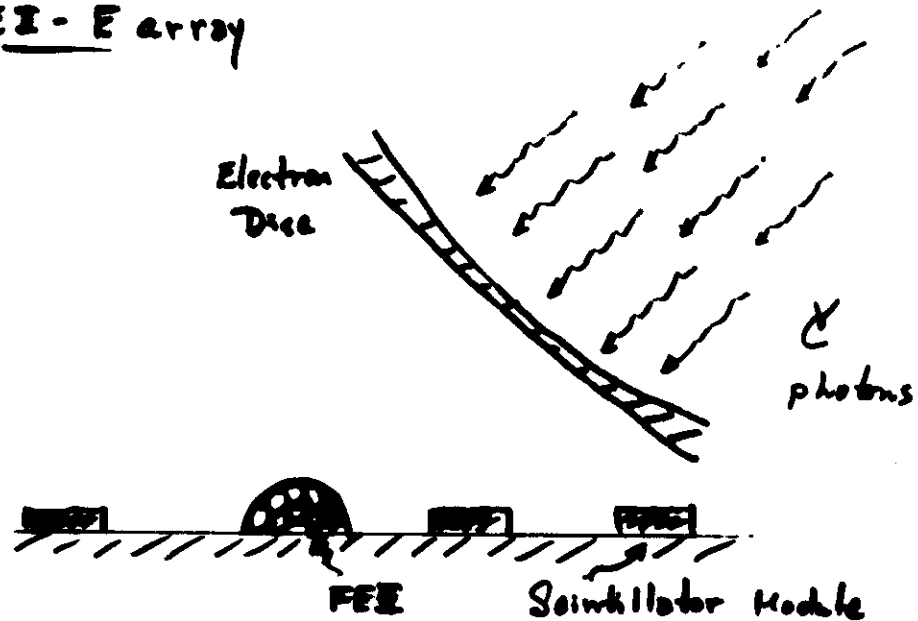


Figure 27

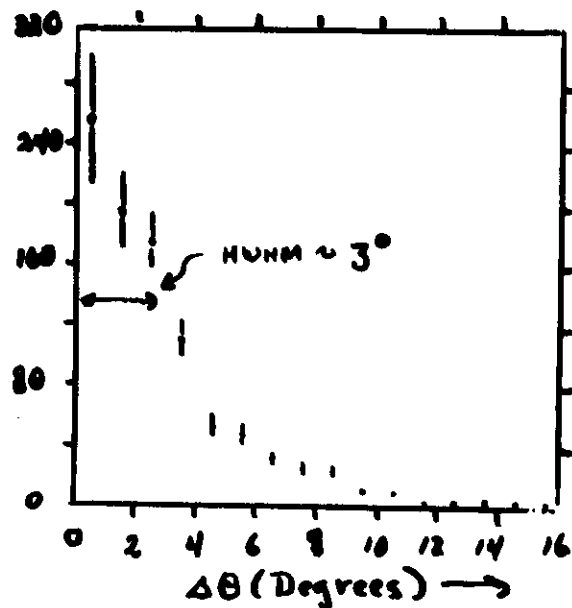
Angular Resolution I

FEE - E array



$\Delta\theta$ (FEE - Array)

3.5 Modules
"Conical" Correction



FEE tube $\sim \pm 2.5^\circ$
 $\Rightarrow \sigma_{\text{Array}} \sim 1.4^\circ$

TIME FOR 6 SIGMA DETECTION OF CYG X-3

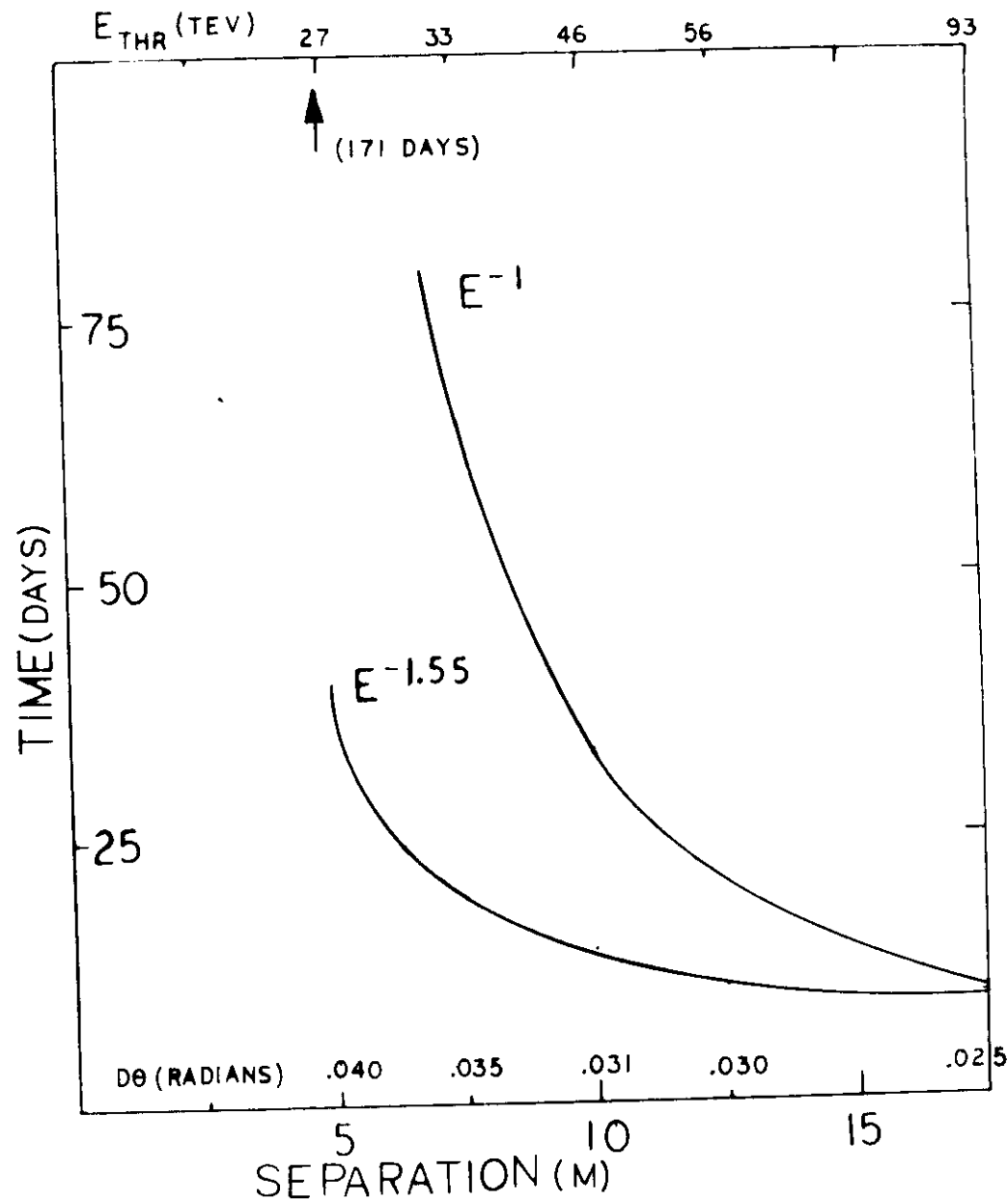


FIG 28

Angular Resolution (II)

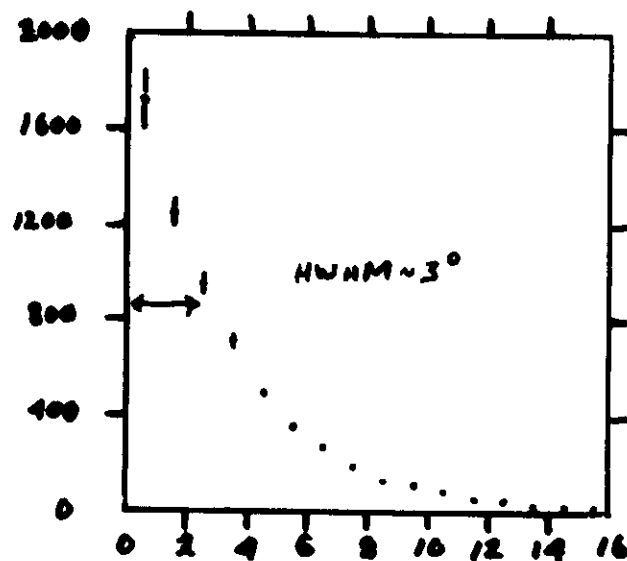
→ Check array against itself

Specify $\Delta\theta$ resolution of each + core
 Analyze each $\Delta\theta$ separately!

Array
Modules

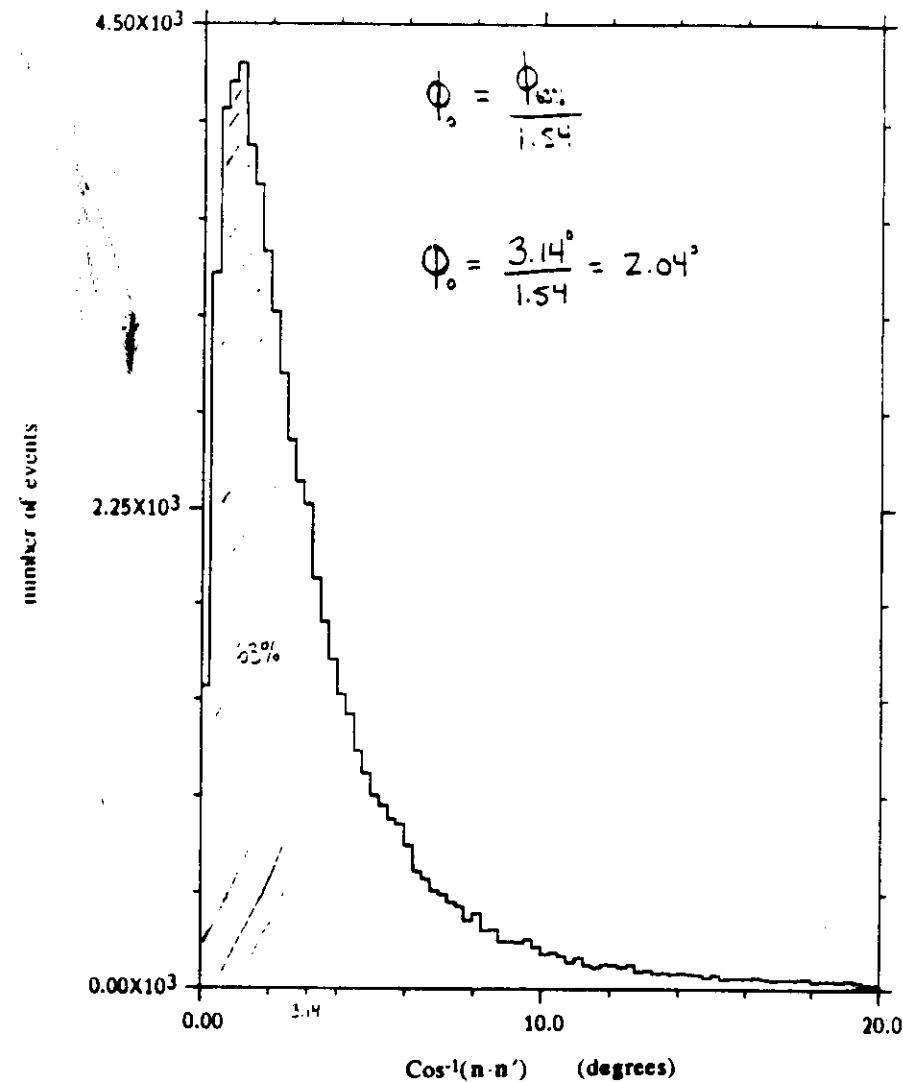


$\Delta\theta (\text{Array}_1 - \text{Array}_2)$



35 Modules
 each $\frac{1}{2}$
 "Conical" Correction

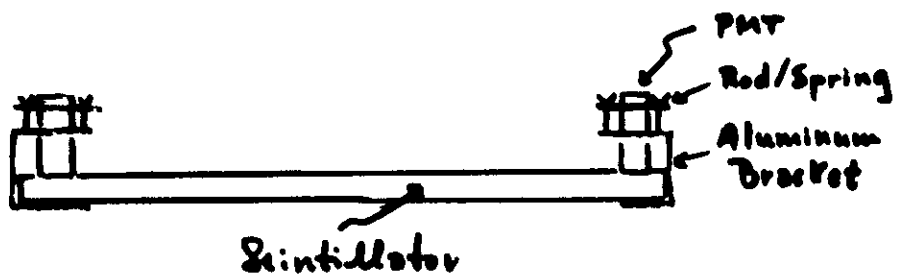
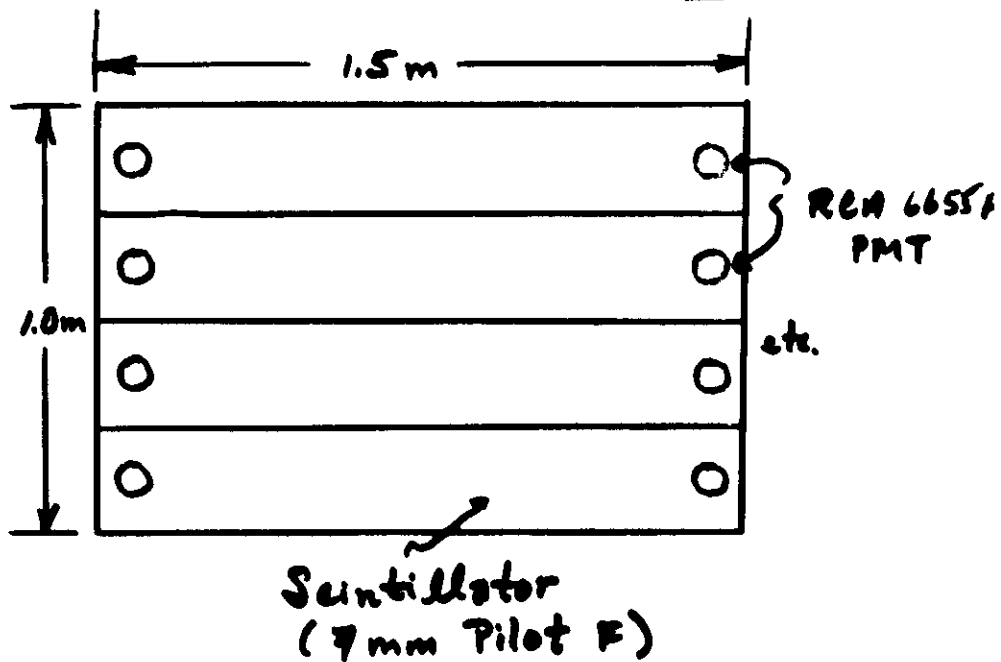
$\Rightarrow \sigma_{\text{array}} \sim 1.8^\circ$



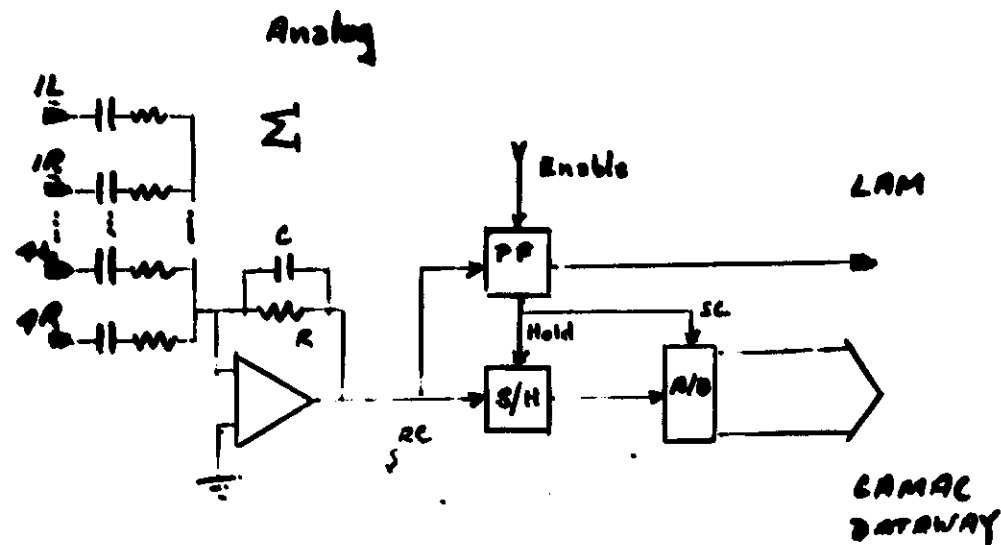
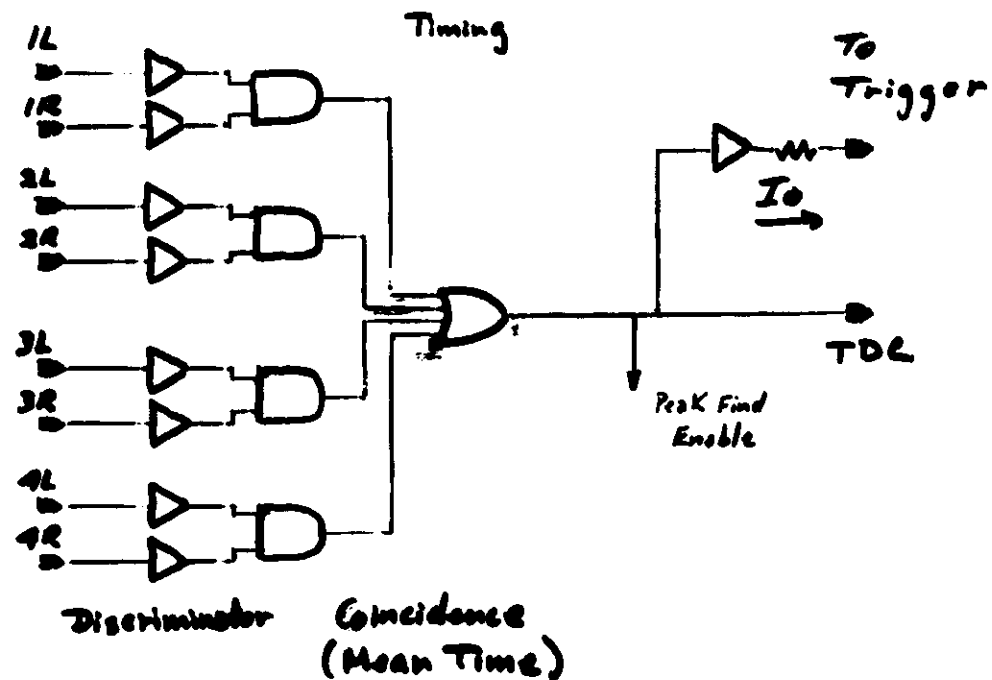
MEAN= 3.615 SIGMA= 4.565
 0.6478E+05 POINTS 0.6386E+05 POINTS IN PLOT
 0.0000E+00 OUT ON LEFT 921.0 OUT ON RIGHT

Figure 33 Distribution of $\text{Cos}^{-1}(\mathbf{n} \cdot \mathbf{n}')$

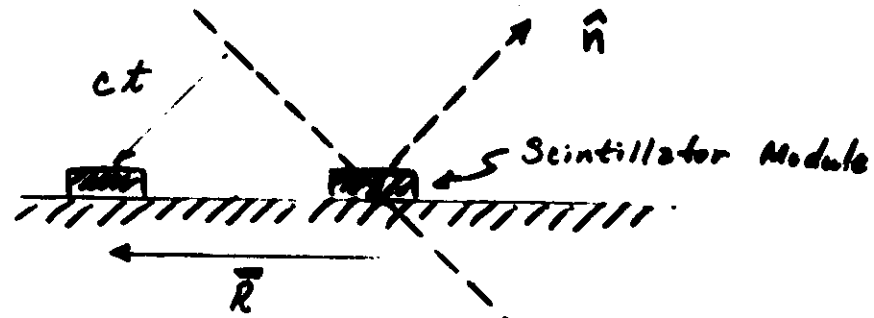
ARRAY Counters UTAH



ARRAY ELECTRONICS

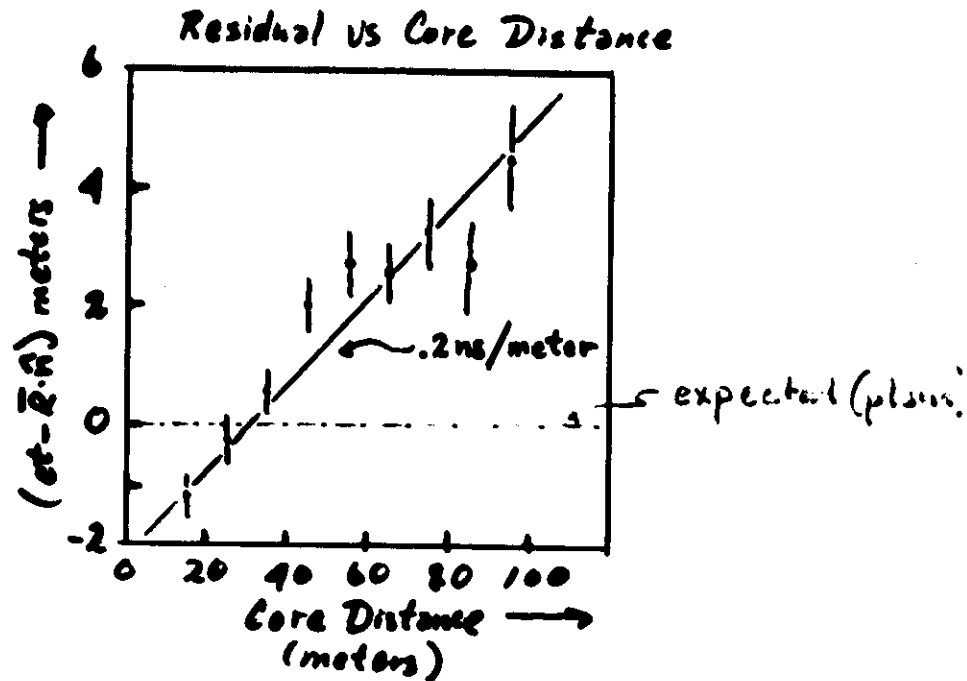


Electron Array Angular Resolution

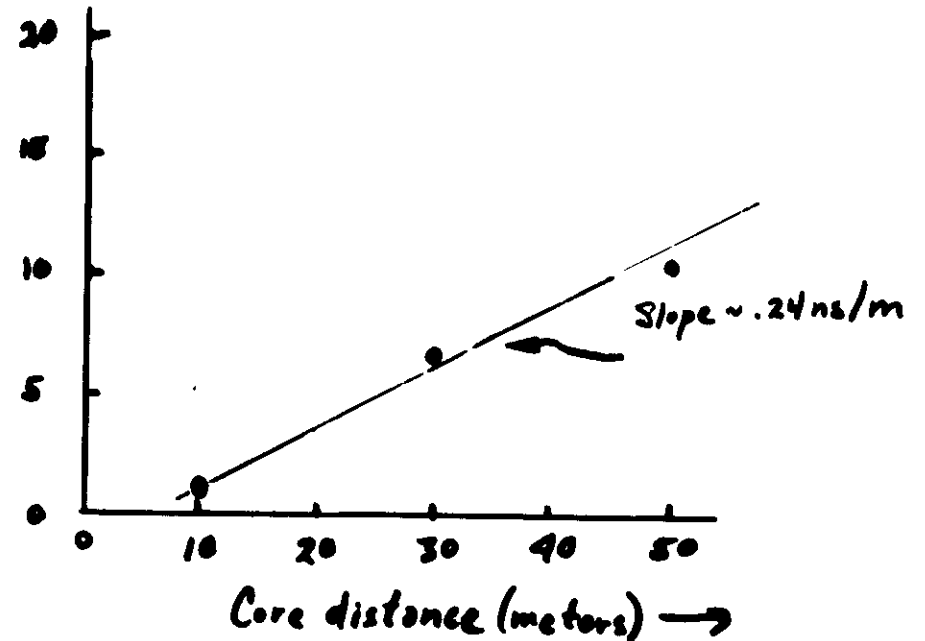
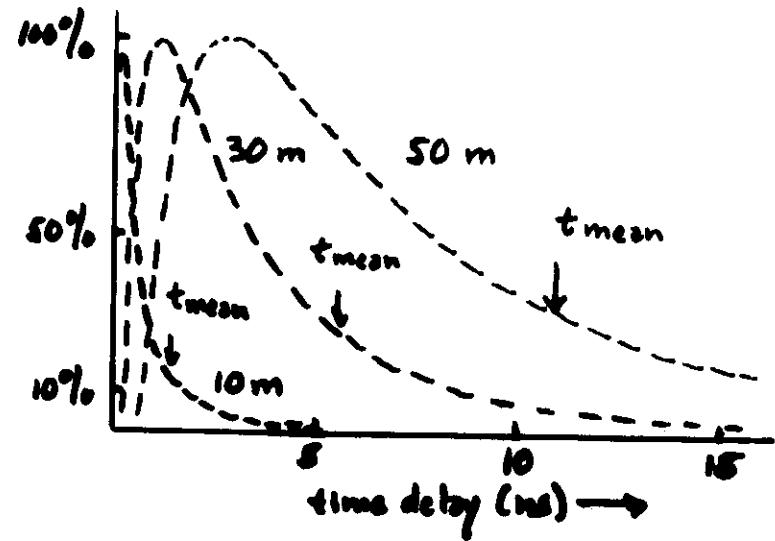


For a plane:

$$ct_{\text{measured}} = \vec{R} \cdot \hat{n}_{\text{fitted}}$$



Time Distribution of Scintillator Signal for PeV KAS (Hillas)



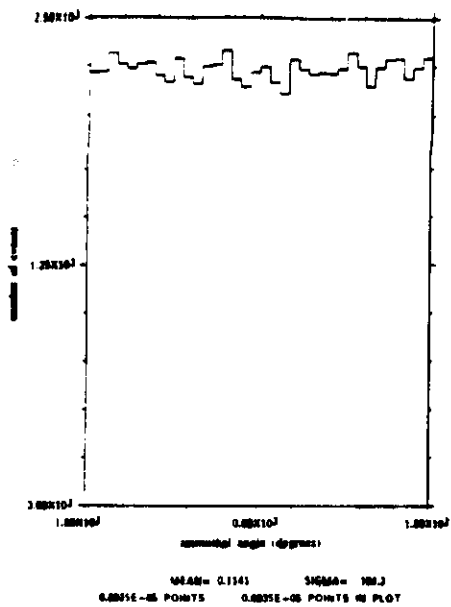


Figure 34a: Azimuthal Angular Distribution (zenith angle $\leq 15^\circ$)

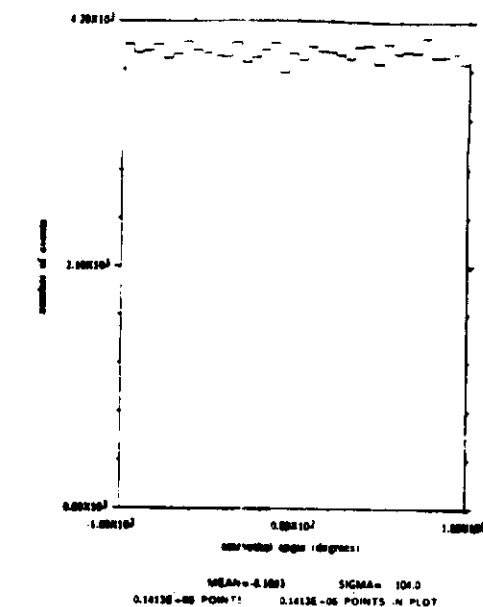


Figure 34b: Azimuthal Angular Distribution ($15^\circ \leq \text{zenith angle} \leq 30^\circ$)

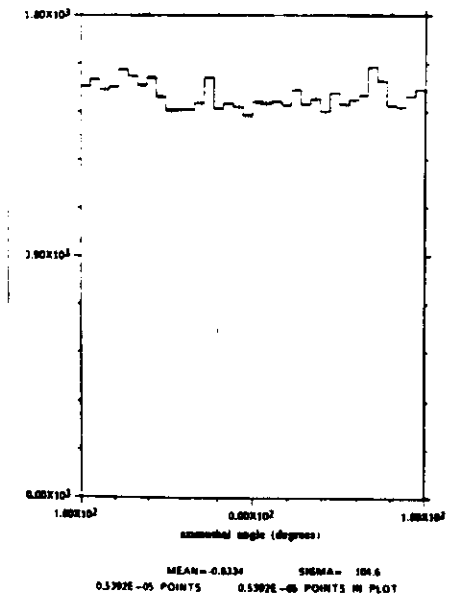


Figure 34c: Azimuthal Angular Distribution ($30^\circ \leq \text{zenith angle} \leq 40^\circ$)

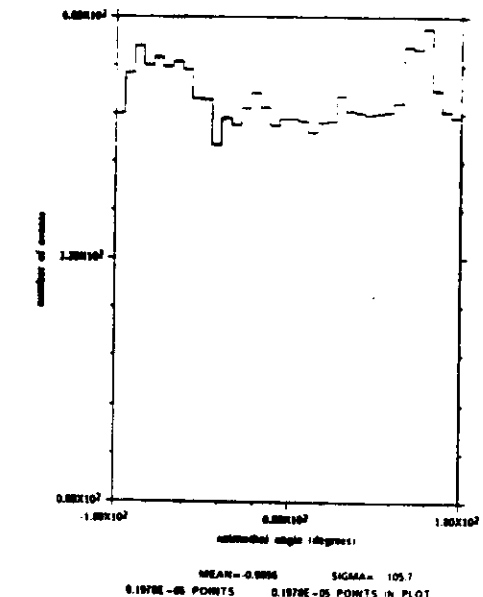


Figure 34d: Azimuthal Angular Distribution (zenith angle $\geq 40^\circ$)

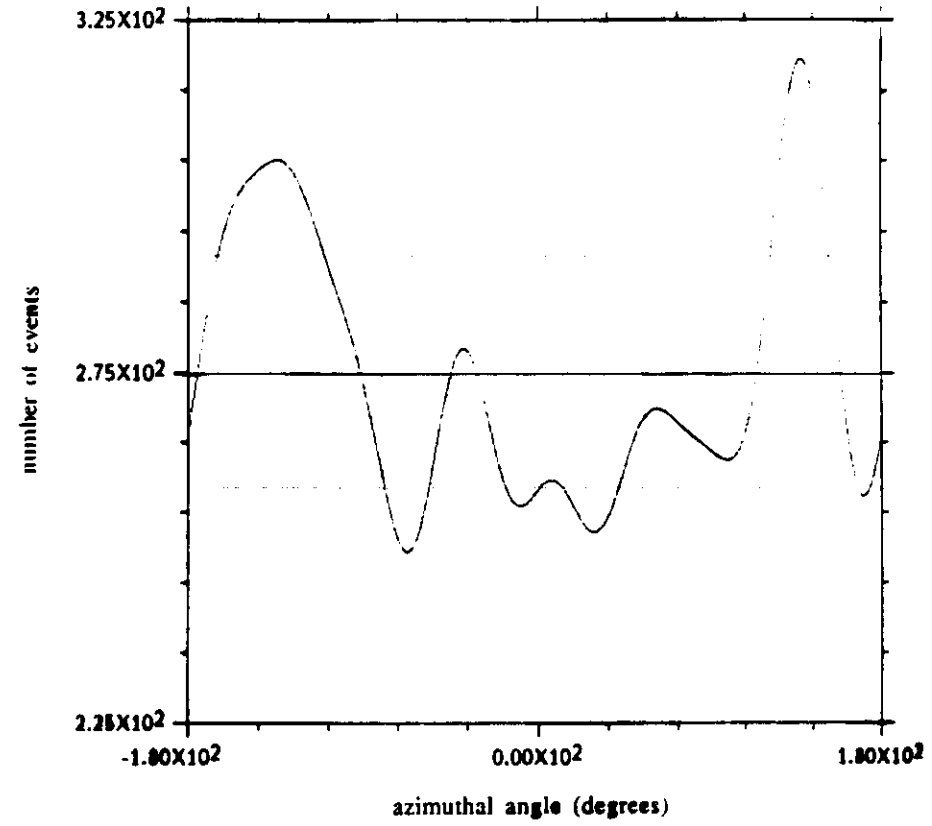


Figure 35a: Fourier Expansion of Azimuthal Angular Distribution (zenith angle $\geq 40^\circ$)

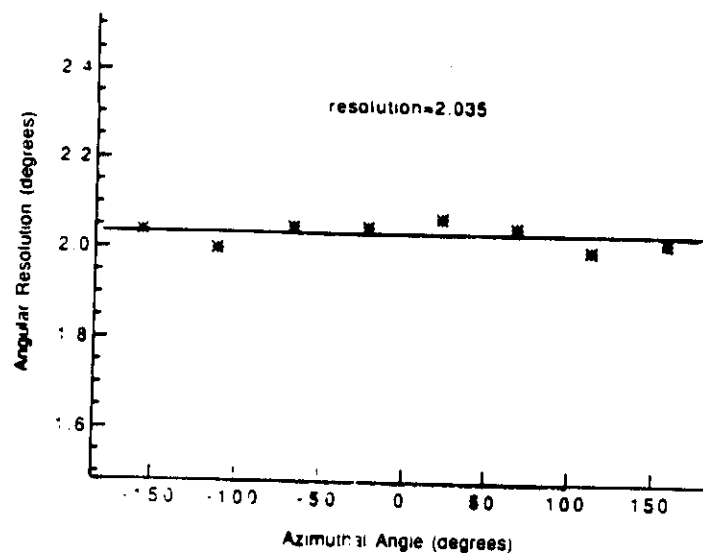


Figure 36a Angular Resolution vs. Azimuthal Angle

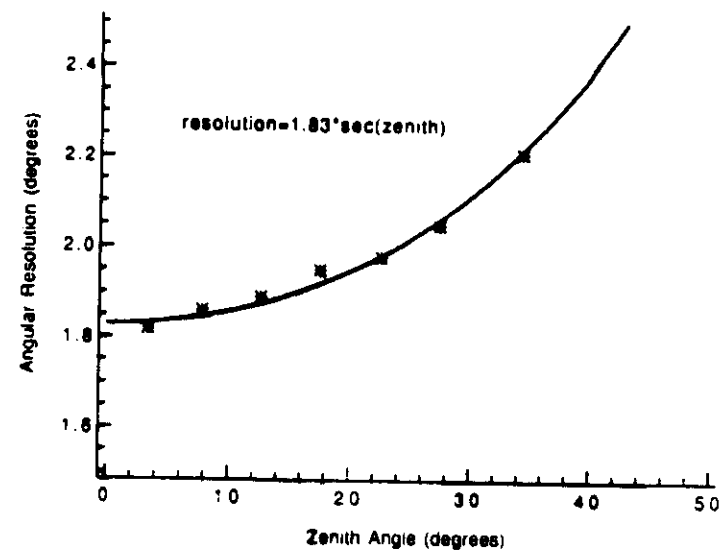


Figure 36c Angular Resolution vs. Zenith Angle

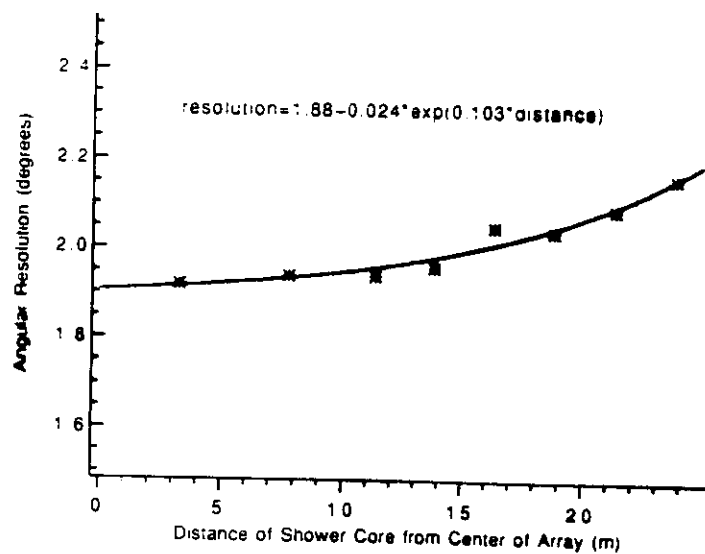


Figure 36b Angular Resolution vs. Distance from Shower Core to Center of the Array

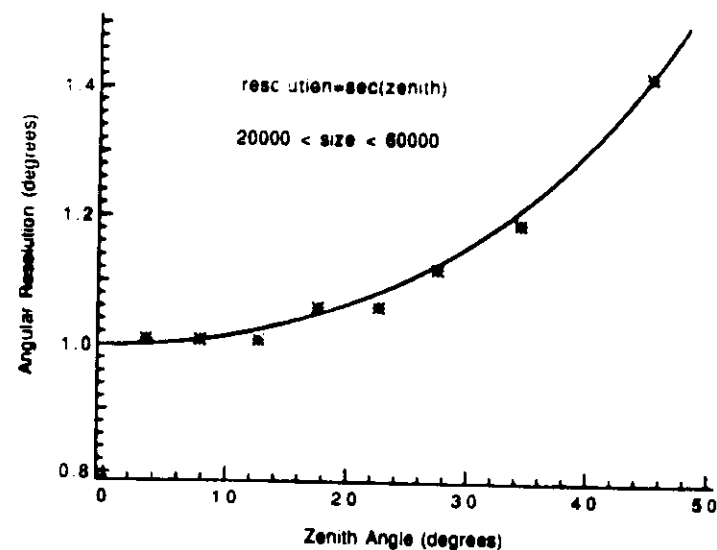


Figure 36d Angular Resolution vs. Zenith Angle
(20000 ≤ shower size ≤ 60000)

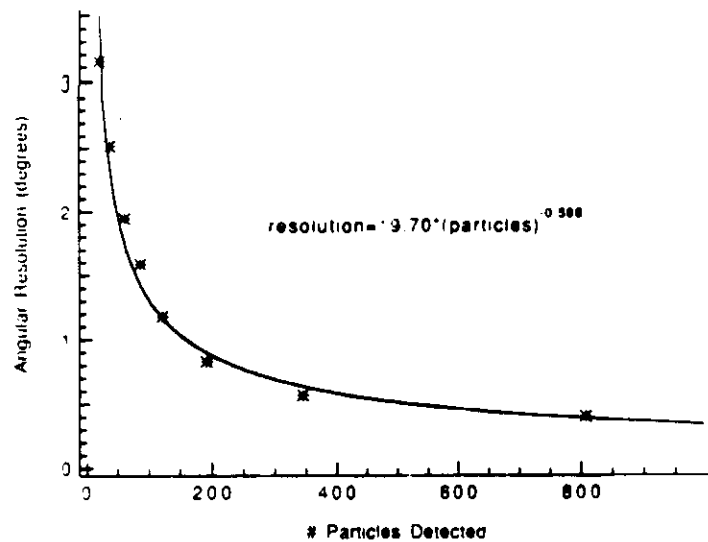


Figure 36e Angular Resolution vs. Number of Particles Detected

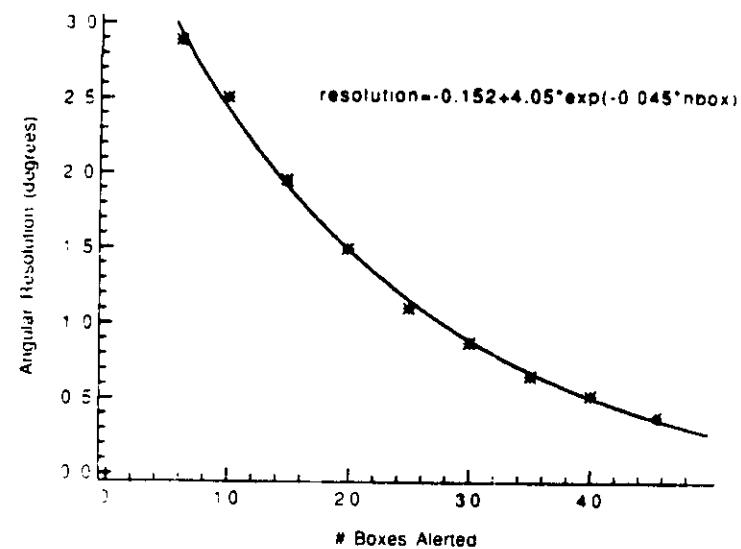


Figure 36g Angular Resolution vs. Number of Box Alerts

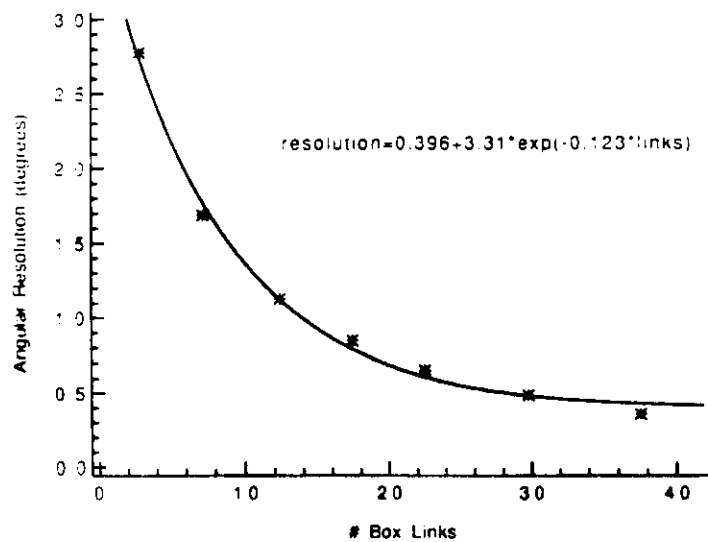


Figure 36f Angular Resolution vs. Number of Box Links

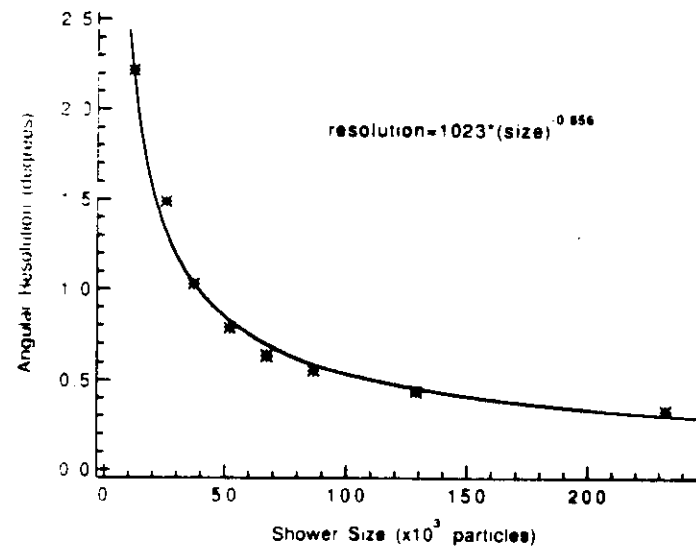


Figure 36h Angular Resolution vs. Shower Size

Size Estimates

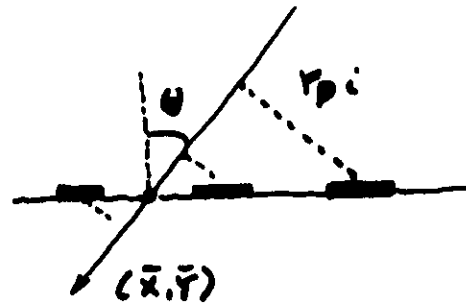
- Find shower core

$$X = \sum x_i n_i \quad Y = \sum y_i n_i$$

$$n_i = N_i / N_{TOT} \quad \text{from pulse heights}$$

- Find r_{pi} and

$$\rho(r_{pi}) = \frac{N_i}{A \cos \theta}$$



- Fit to NKG

$$\rho(r_p) = N_e \overset{\text{size}}{f(s, r_p / r_1)} / r_1^2$$

$$r_1 = \text{Moliere radius (94 m at Dagway; 79 at Sashur)}$$

$$f = \left(\frac{r_p}{r_1}\right)^{s-2} \left(1 + \frac{r_p}{r_1}\right)^{s-4.5} \frac{\Gamma(4.5-2s)}{2\pi \Gamma(s) \Gamma(4.5-s)}$$

$$n \rho \sim \frac{A_1 \exp^{-A_2 r_p}}{r_p}$$

$$N_e = 2\pi A_1 / A_2 \overset{\text{size}}{f}$$

$$\text{Note } N_e = \int 2\pi \rho(r_p) dr_p$$

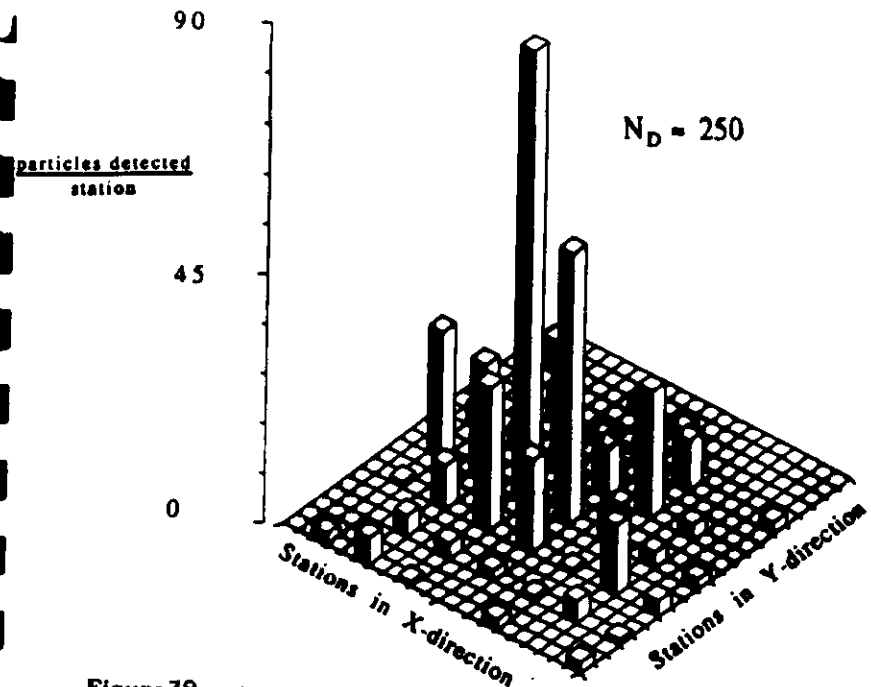
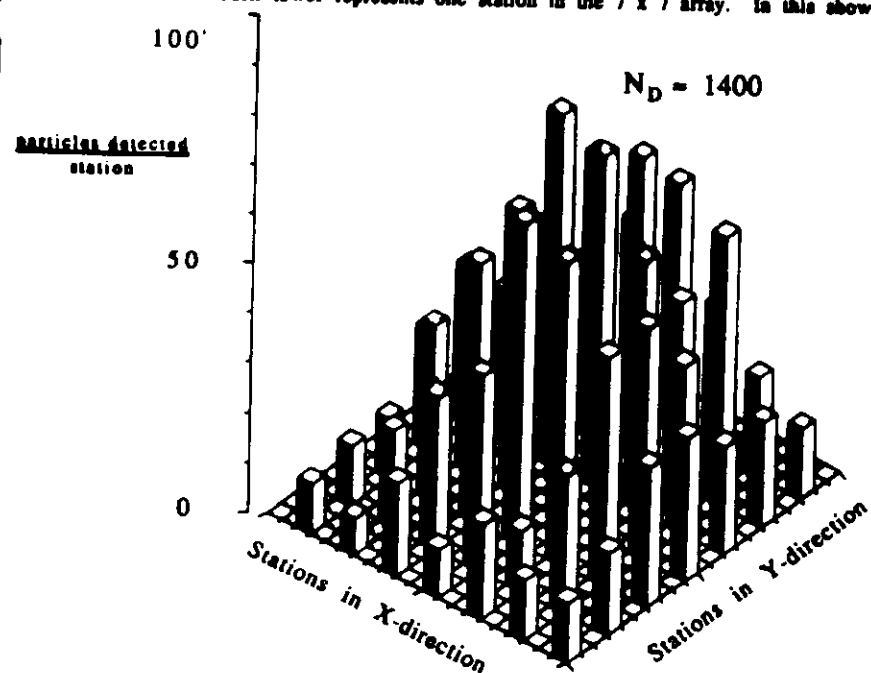


Figure 39. a) Number of particles detected per station in an EAS as recorded by the 7 x 7 CASA. Each tower represents one station in the 7 x 7 array. In this shower, $N_D = 250$.



b) Same as (a), but $N_D = 1400$.

Radial bin of r_1 (m)	$\bar{\rho}(r_1)$ ($\frac{\text{particles}}{\text{m}^2}$)	$\sigma_{\bar{\rho}}$	NumEvents	Mean δ M Counters firing
16.00	39.00	24.02	590.00	3.70
21.21	26.16	15.79	500.00	3.72
26.00	20.00	15.30	500.00	3.73
30.00	19.01	15.10	610.00	3.72
33.64	14.30	12.80	676.00	3.73
36.74	11.77	10.56	510.00	3.77
39.00	10.13	9.29	631.00	3.67
42.43	8.29	8.02	400.00	3.58
46.00	7.03	6.93	425.00	3.50
47.43	6.75	7.33	366.00	3.49
49.75	5.47	4.46	300.00	3.40
51.90	5.25	5.20	347.00	3.30
54.00	4.45	4.00	300.00	3.22
56.12	4.22	4.52	240.00	3.14
58.00	3.70	3.50	227.00	3.09
60.00	3.30	3.24	233.00	3.00
61.86	3.00	3.17	221.00	2.90
63.64	2.84	2.80	100.00	2.72
65.30	2.40	2.53	175.00	2.60
67.00	2.00	2.04	101.00	2.63
68.74	2.00	2.30	113.00	2.65
70.30	2.50	3.44	101.00	2.52
71.94	1.04	2.20	77.00	2.10
73.48	2.35	2.90	61.00	2.50
75.00	2.21	3.42	63.00	2.00
76.49	1.00	2.02	30.00	1.72
77.94	0.75	0.84	10.00	1.07
79.37	0.06	1.31	21.00	1.33
80.78	1.72	2.40	39.00	2.16
82.10	1.03	1.94	24.00	1.00
84.05	1.16	1.42	12.00	2.00

Figure 40. A sample of data from a composite shower. Here, $N_D = 800 \pm 25$.

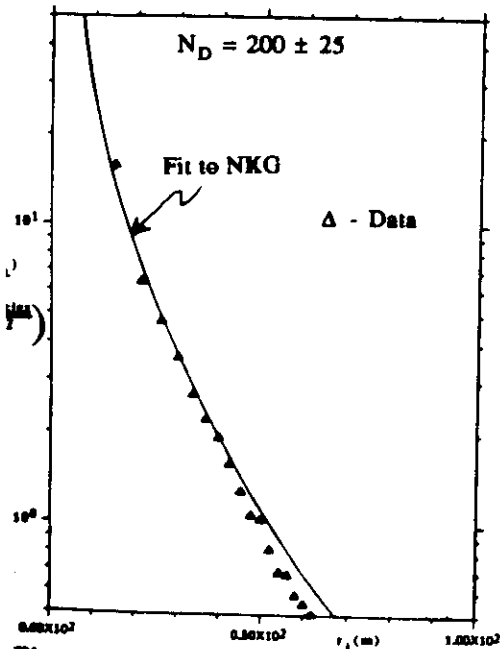
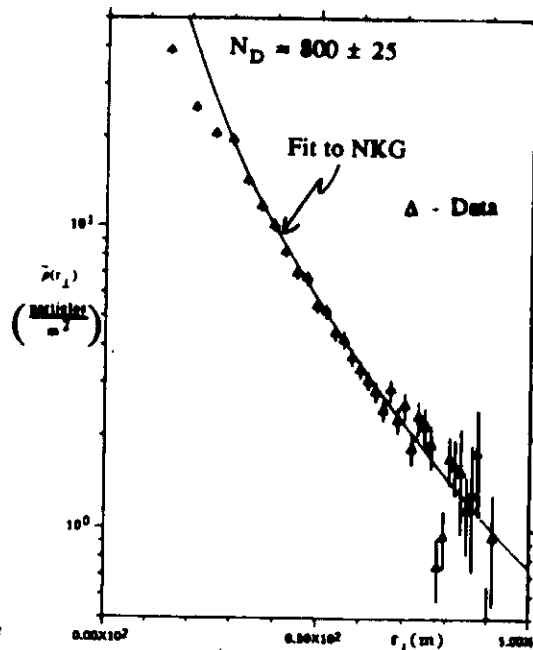


Figure 41a. Fit to a composite shower with $N_D = 200 \pm 25$. Only the r_1 between 30m and 45 m were used for the fit because of systematic error on either end of this range.



b) Same as (a), but with $N_D = 800 \pm 25$. Deviations from NKG can be seen for small r_1 due to large fluctuations near the core, and imperfect core reconstruction. Only r_1 between 30m and 77m were used for the fit.

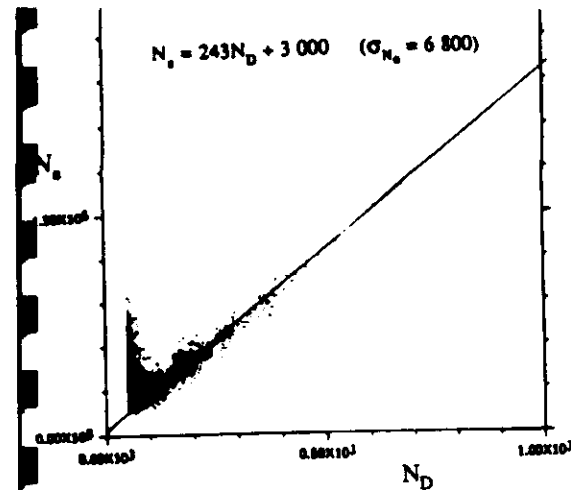


Figure 41a N_s vs N_D for fitting to both N_s and s . Note the difficulties in fitting N_s for small N_D . The probability of fit for these showers is $\geq .99$.

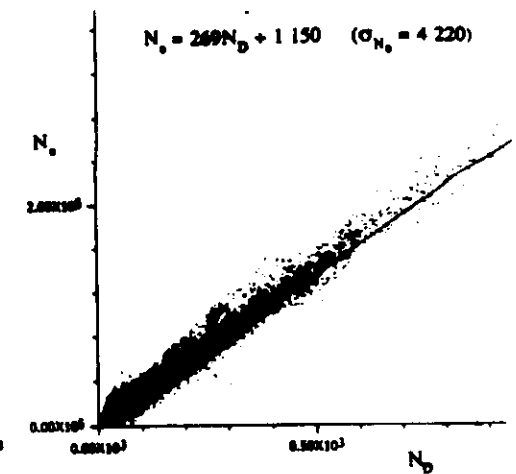


Figure 41b N_s vs N_D for fitting to N_s , with s fixed at 1.3. The probability of fit for these showers is ≥ 0.01 .

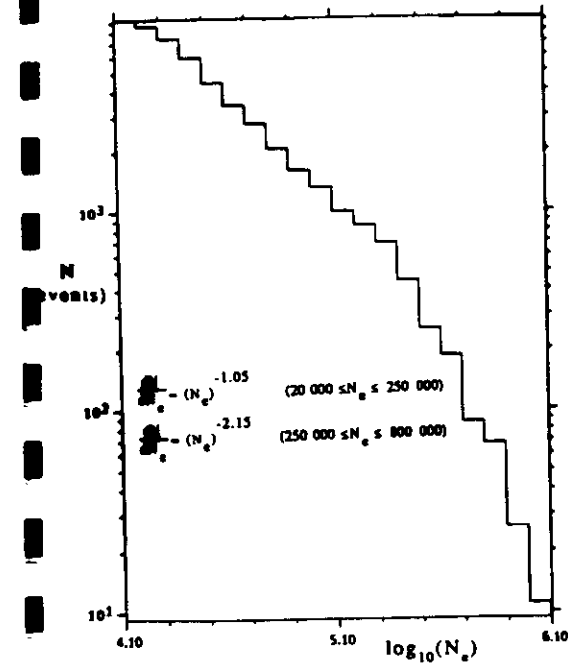


Figure 41c Differential spectrum of N_s using χ^2 minimization technique using fixed age of 1.3.

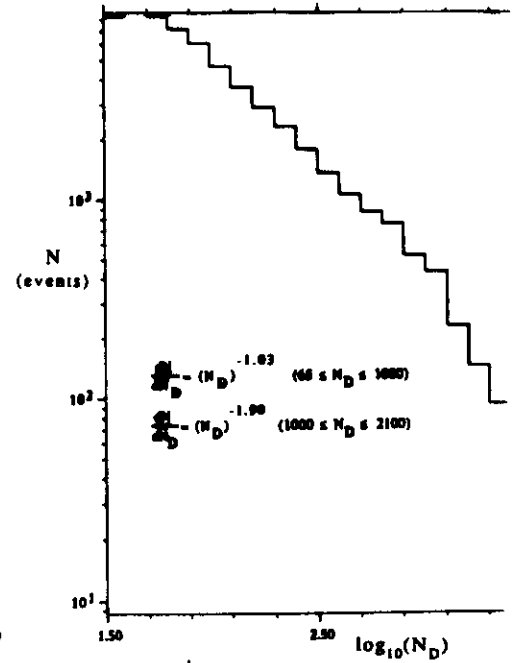


Figure 41d Differential spectrum of N_D using the similar power laws and regions of inflection to Figure 13.

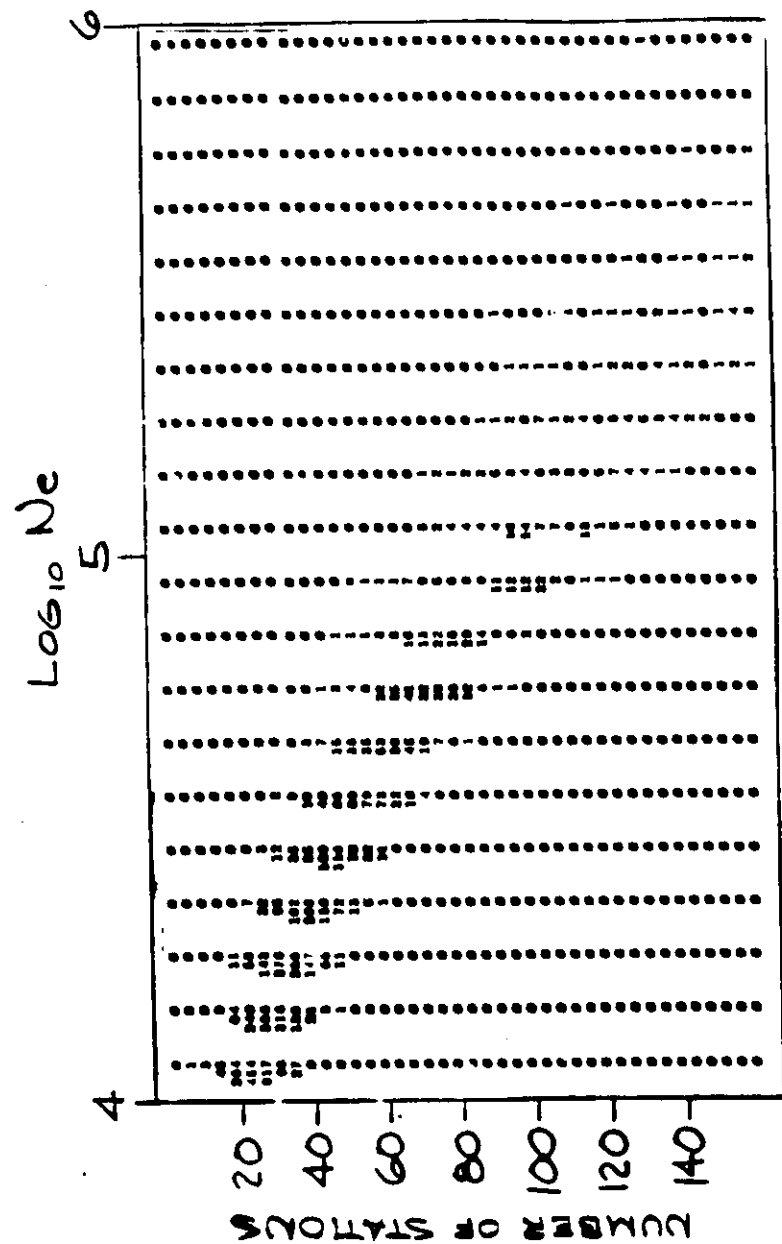


Figure 37a

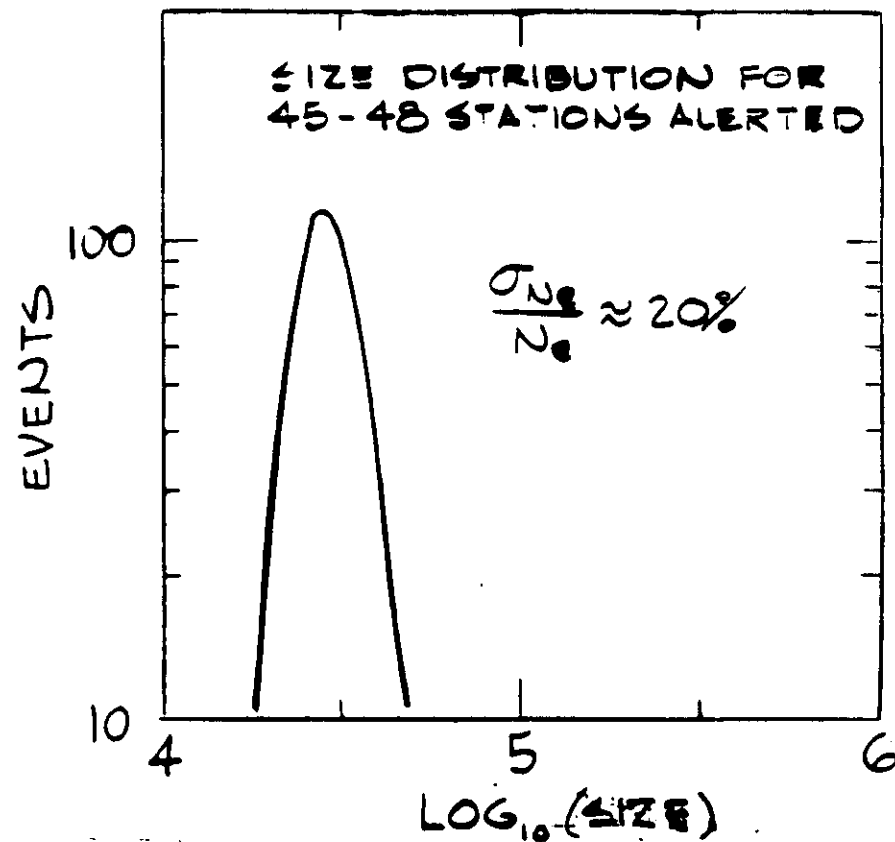
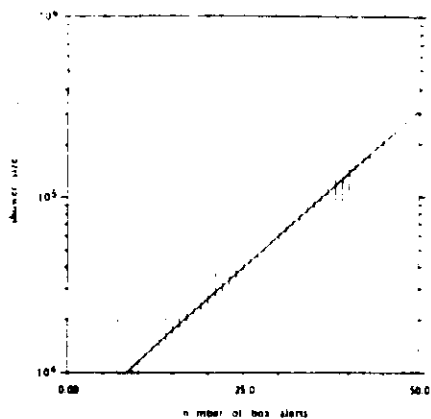
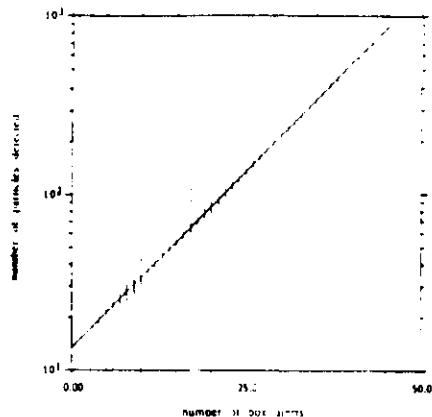


Figure 37b



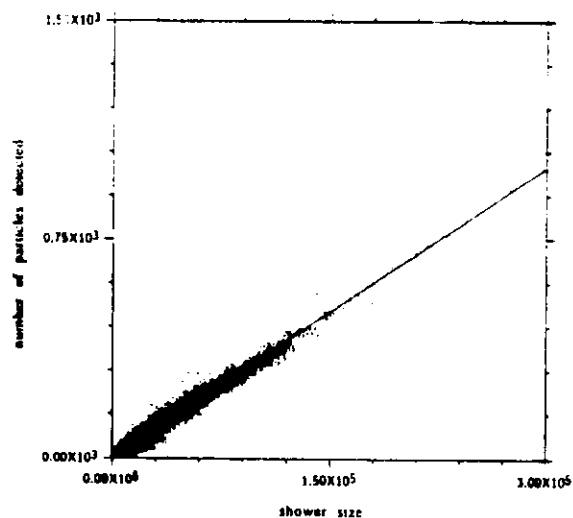
25000 POINTS IN PLOT 7480 POINTS OUT OF PLOT

Figure 38a: Shower Size vs.
Number of Box Alerts



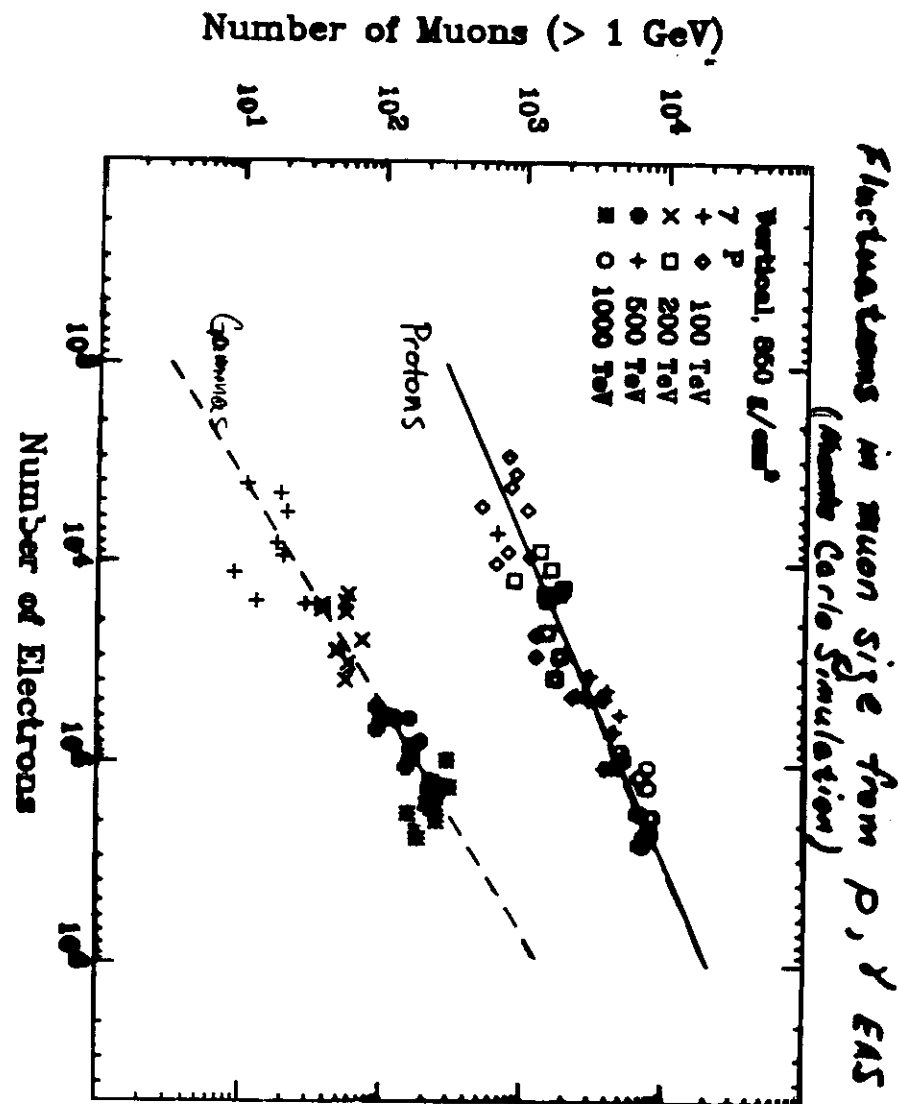
31900 POINTS IN PLOT 582 POINTS OUT OF PLOT

Figure 38b: Number of Particles Detected vs.
Number of Box Alerts



32405 POINTS IN PLOT 95 POINTS OUT OF PLOT

Figure 38c: Number of Particles Detected vs.
Shower Size



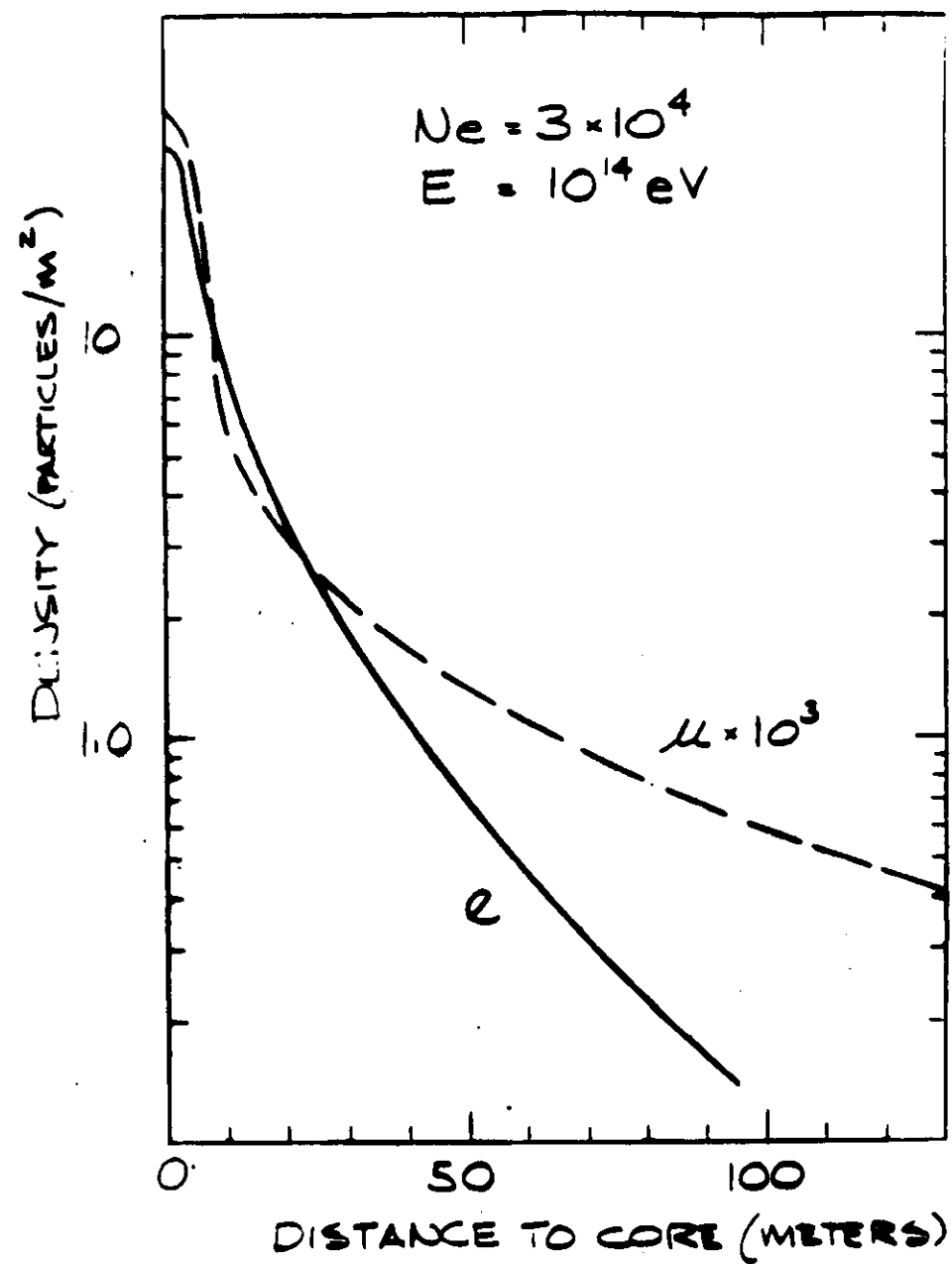
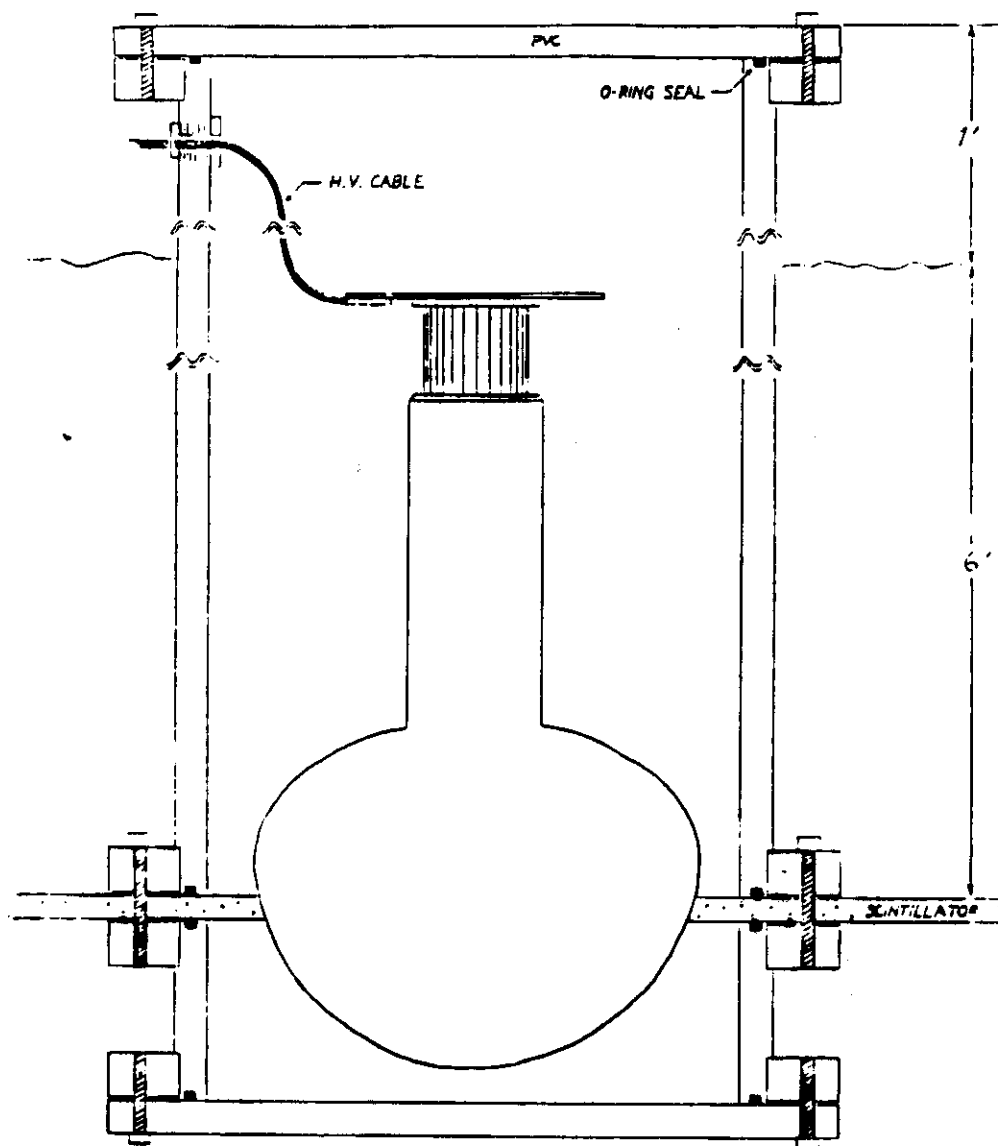
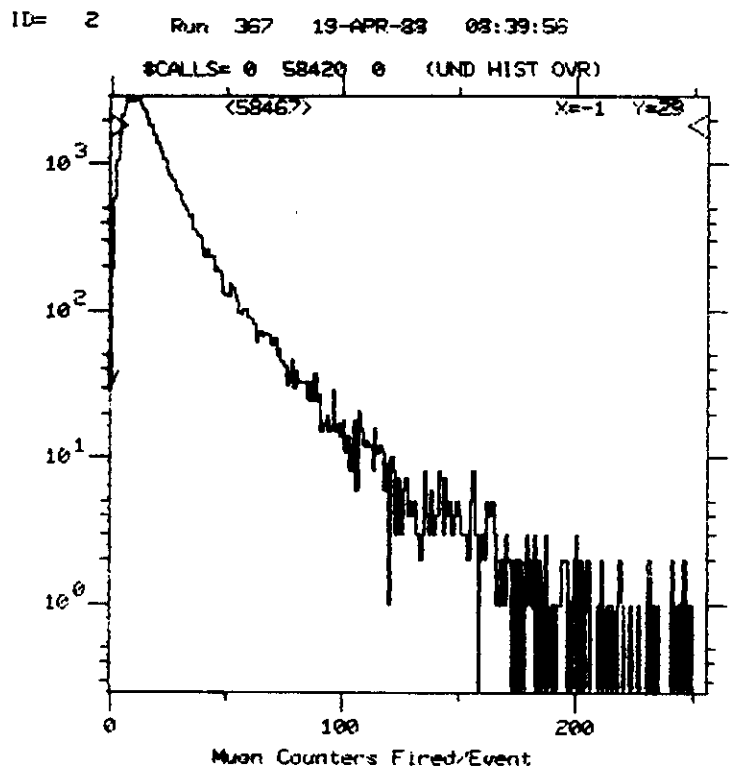


Figure 44

edraw Screen
 list. Select
 Window
 Full Screen
 Lot
 Lot All
 Inear
 Ugerithmic
 umber Across
 umber Down
 d Scatter
 d LeGgo
 d MESH
 ew Angle
 rror Bar opt.
 ile option
 int Style
 ile Size
 ight Point
 eft Marker
 ight Marker
 ottom Marker
 op Marker
 ped Input
 ommand File
 et Variable
 amine Var.
 Paun command
 Xit



Average μ /event ≈ 30 (4 patches)

Mean μ /event ≈ 11 (4 patches)
 22 (8 patches)

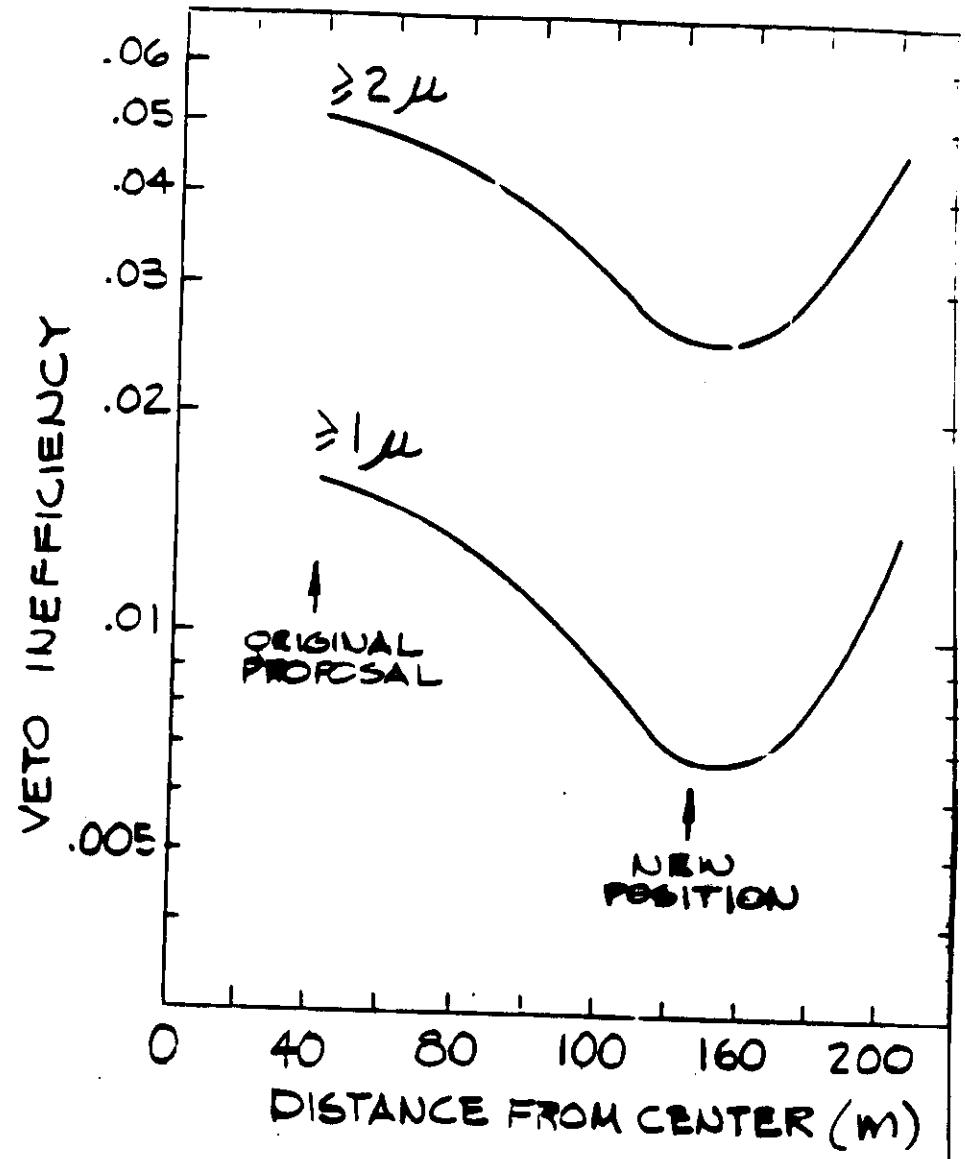
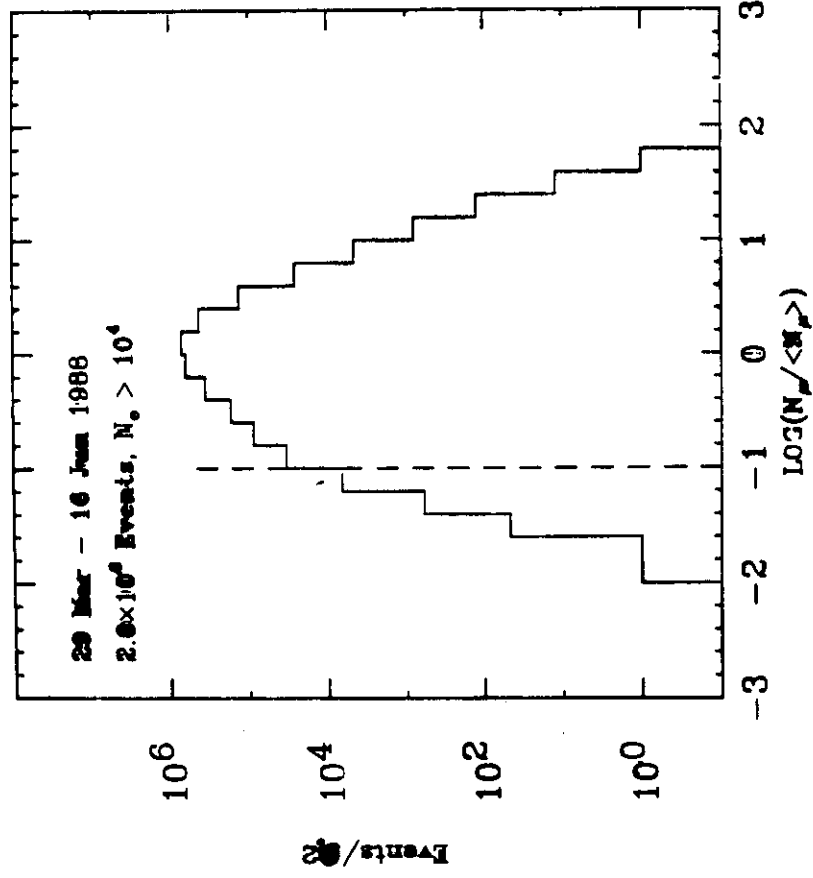
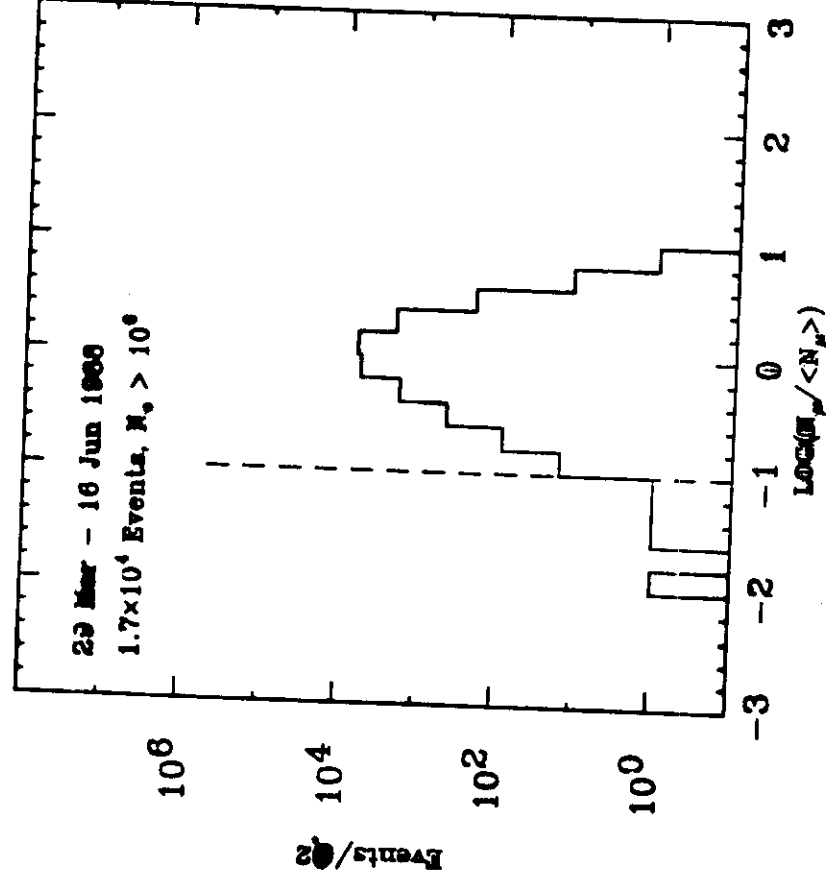


Figure 46

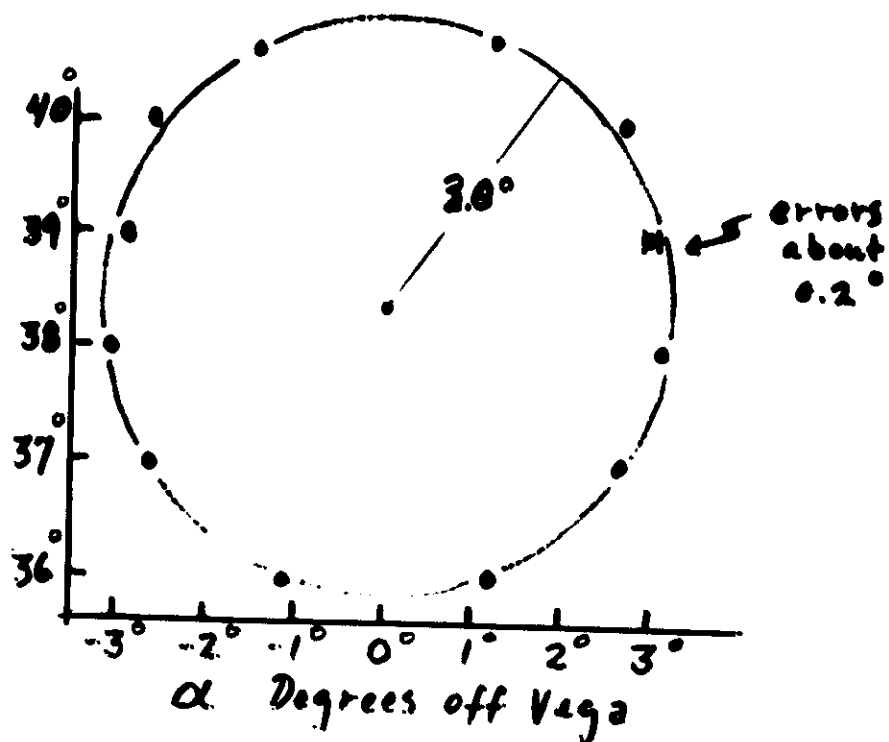
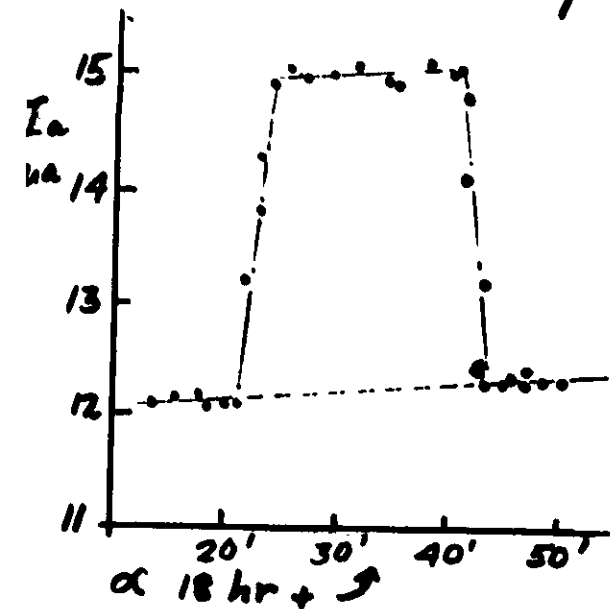
rejection
~ 1/100



rejection
~ 1/4000



DC Scan of Vega



Geometrical Reconstruction

- Like e^+ array - but Cherenkov photons more numerous ($\sim 10^3$) — more spread out
- Telescope radius ~ 120 m
separation ~ 170 m
- Need Light production model
 - em longitudinal development
 - distribution e^+ angles & energies
 - particle and photon delays
 - atmospheric attenuation of light
 Hillas
J. Phys. G
Nucl. Physics
2, 1461 (1982).
- Monte-Carlo Cherenkov light production
 - In 4 telescope events - fit to 3 - find
 $\text{rms } \delta t \sim 2.7$ ns and $\delta \phi \sim 17\%$
 - Adjust Monte-Carlo by above errors
 - Find: $\delta \theta_{\text{rms}} = \begin{cases} 0.66^\circ \text{ at } 10^{14} \text{ eV} \\ 0.45^\circ \text{ at } 3 \cdot 10^{14} \text{ eV} \end{cases}$
 $\delta E_{\text{rms}} \approx 15\%$
 $\delta R_{\text{core}} \approx 15 \text{ meters}$

Angular Resolution of Cherenkov Arrays

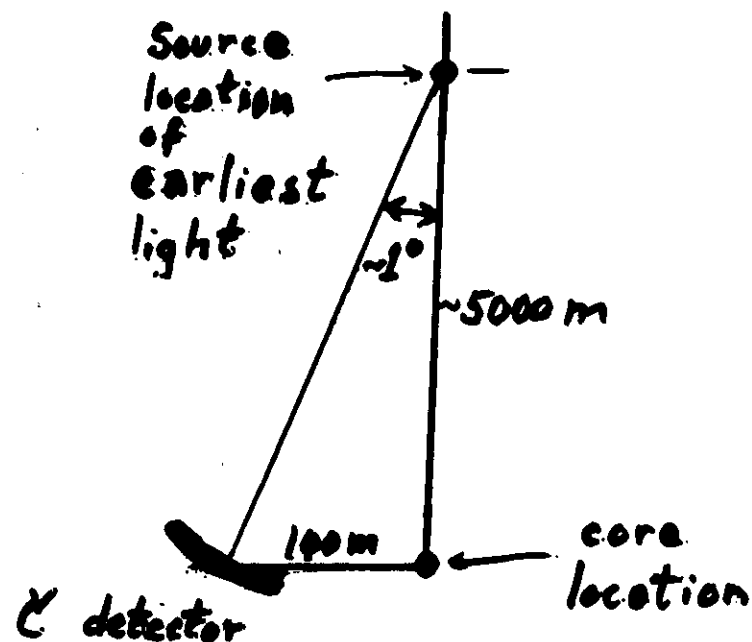
Light spreads over about 200 m at detectable levels.

Shower direction from fast timing of almost planar light.

Accuracy: $\Delta t / (d/c) = 3 \text{ ns} / 600 \text{ ns}$

Error ≈ 0.005 radians $\approx 1/4^\circ$. (1)

But this is for direction of flash, not of shower.



Core location fit to pulse amplitudes in telescopes.
Accuracy: $10\text{m} \leftrightarrow 0.1 \text{ degrees}$ (2)

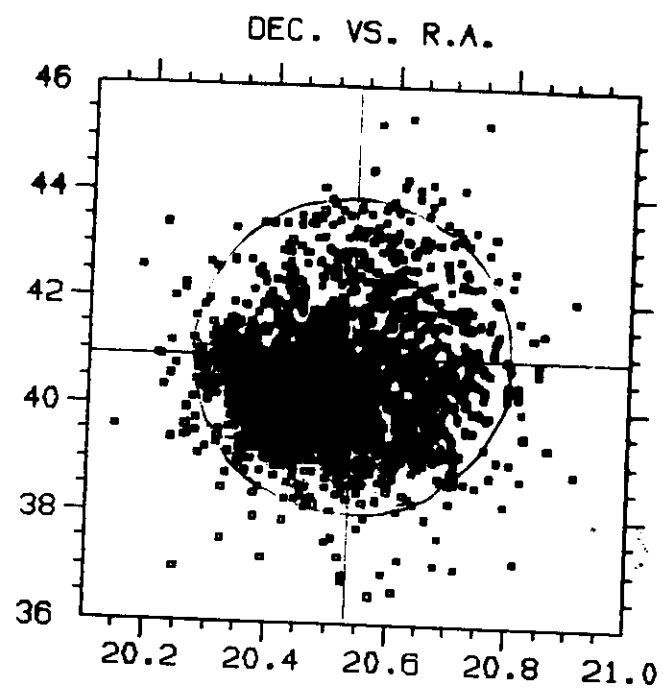
Light source altitude error:
 $50 \text{ g/cm}^2 \leftrightarrow 2/3 \text{ km} \leftrightarrow 1/6^\circ$

Monte Carlo gives $\Delta\theta \approx 1/3^\circ$. (3)

Overall Error $\approx \underline{\underline{1/2^\circ}}$

Reconstruction of Events Entered on C₇₉ 1-3

ID=SCT1



NAMEYPAK 10:02:04 13JUL80

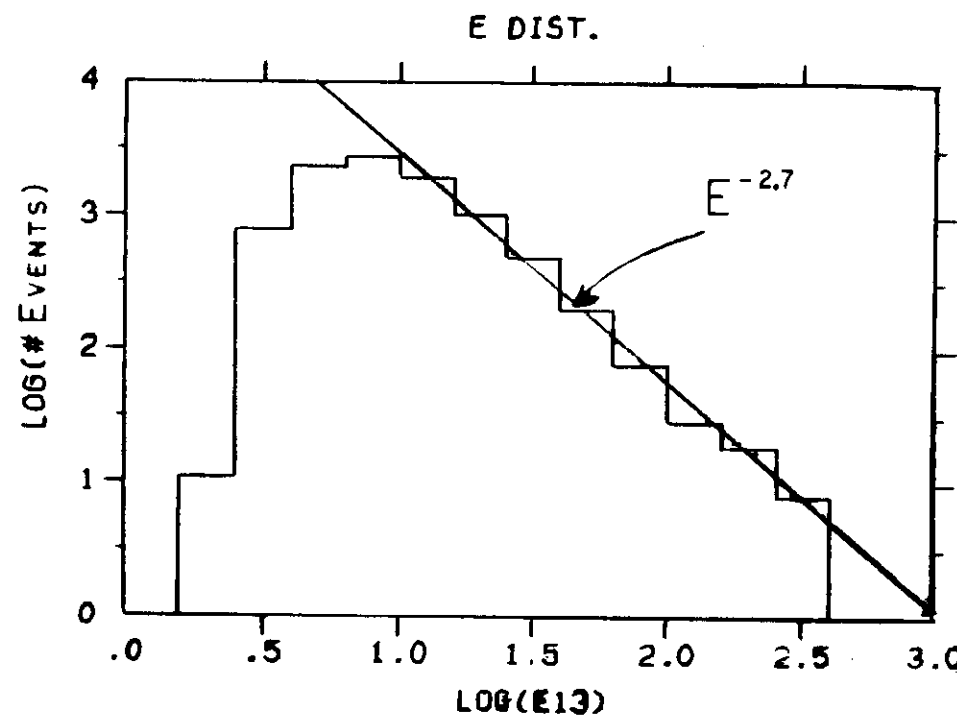


FIG 50

Expected Number of Events in Phase Bin

- Divide full angle four into 2 zones
events from target should reconstruct
from inner zone 1° radius - target zone
background events in $1.5^\circ - 3^\circ$ radius zone
- Find fraction π_b of outer zone which
occur within Cyg X-3 phase bin
- Multiply the total # events in target zone
by π_b is $N_b = \pi_b N_{\text{target}}$

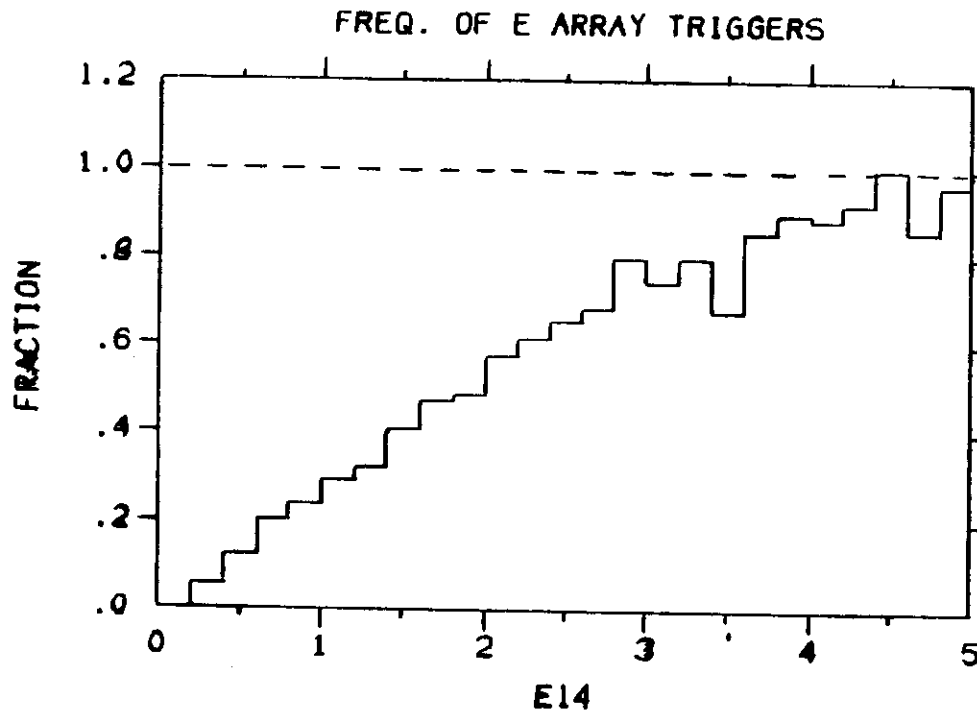
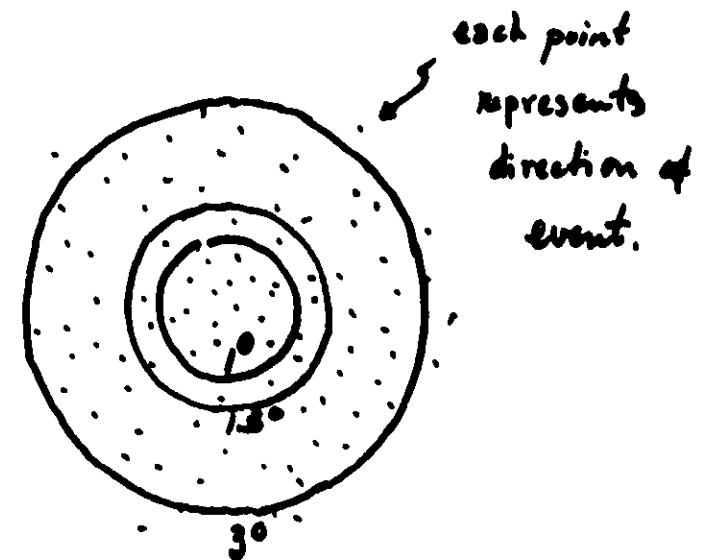


FIG 51



NO MUON CUT

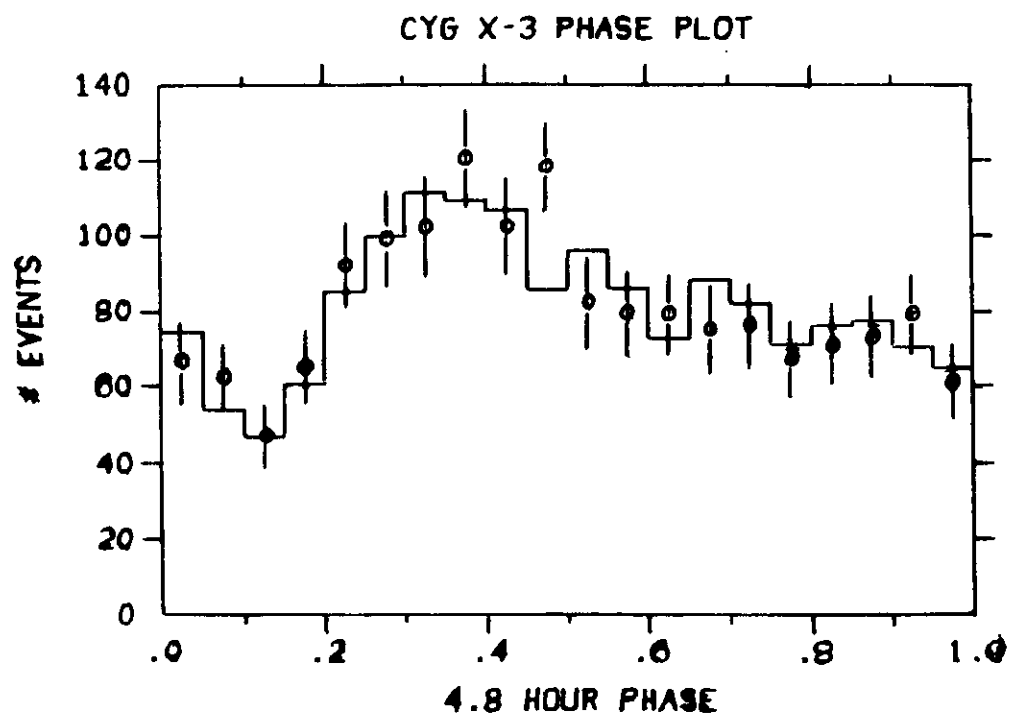


FIG 52a

$N_{\mu} < 0.1 \langle N_{\mu} \rangle$

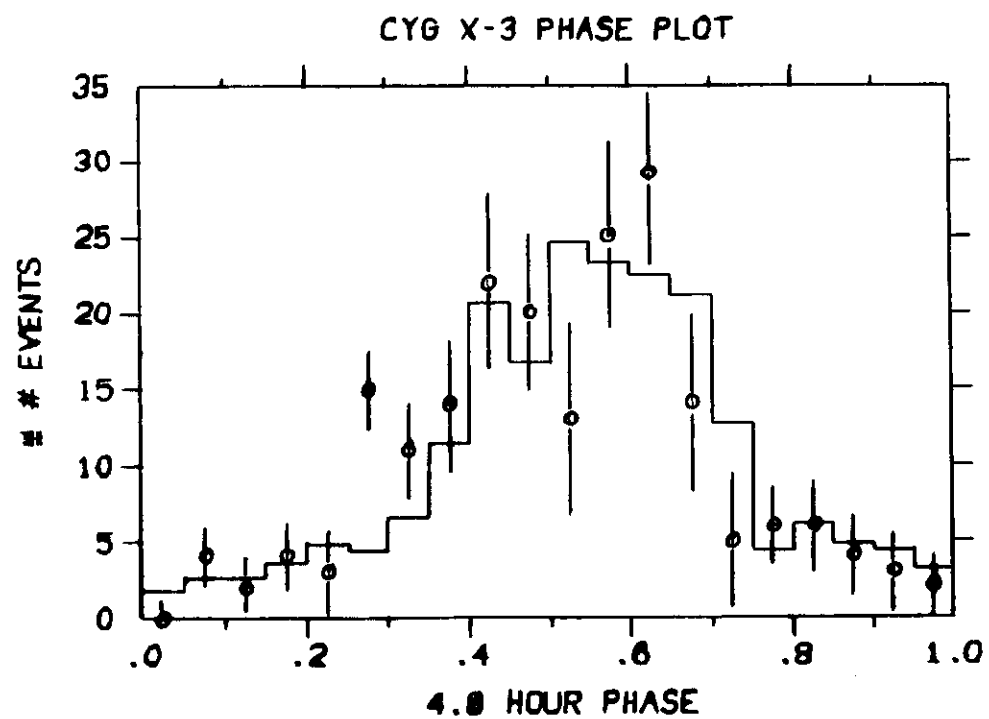


FIG 52b

Rough Flux

11

$$\frac{S}{B} = \frac{F A t}{I(N) A \Omega t} = \frac{F}{I \Omega}$$

$$F = \frac{S}{B} I \Omega$$

(6th bin)

- "Signal" came only in phase bin 0.25-0.30
- "Background" - number of background events in that phase bin $\times 20$

Assuming uniform exposure

$$S = 11 \quad B = 100 \text{ events in phase bin } 0.25-0.30 \text{ (no moon cut)}$$

$$B = 20 \text{ bins} \cdot B_6 = 2000$$

$$I = 5 \cdot 10^{-8} \text{ cm}^{-2} \text{ sr}^{-1} \text{ s}^{-1} \text{ and } \Omega = \pi (1^\circ)^2 = 9.6 \cdot 10^{-4} \text{ sr}$$

$$F = \frac{11}{2000} \cdot 10^{-8} \text{ cm}^{-2} \text{ sr}^{-1} \text{ s}^{-1} \cdot 9.6 \cdot 10^{-4} \text{ sr}$$

$$= 5.3 \cdot 10^{-14} \text{ cm}^{-2} \text{ s}^{-1}$$

$$\Sigma_i = E F = 10^{14} \text{ eV} \cdot 5.3 \cdot 10^{-14} \text{ cm}^{-2} \text{ s}^{-1}$$

$$= \underline{\underline{5.3 \text{ eV cm}^{-2} \text{ s}^{-1}}}$$

A very low flux indeed!

Energy Flux Sensitivities

- Assume 6 σ and 1 yr running time
- ~ 2160 hours for array
- ~ 180 hours for 6 Telescopes

	θ (deg)	A (cm ²)	Σ_i	Σ_r	S	B
FE _{blat}	5	$2 \cdot 10^8$	800	80	104	3000
Utah e ⁺	2	$2 \cdot 10^8$	94	9	140	5400
Utah 6 Tel	0.7	$4.8 \cdot 10^8$	74	7	22	1300
CASA	0.5	$2.5 \cdot 10^8$	7	0.7	137	5000
* Whipple	0.4	$\sim 10^8$	100	10	1163	$\sim 650,000$

* (conditions achieved for ERAB)

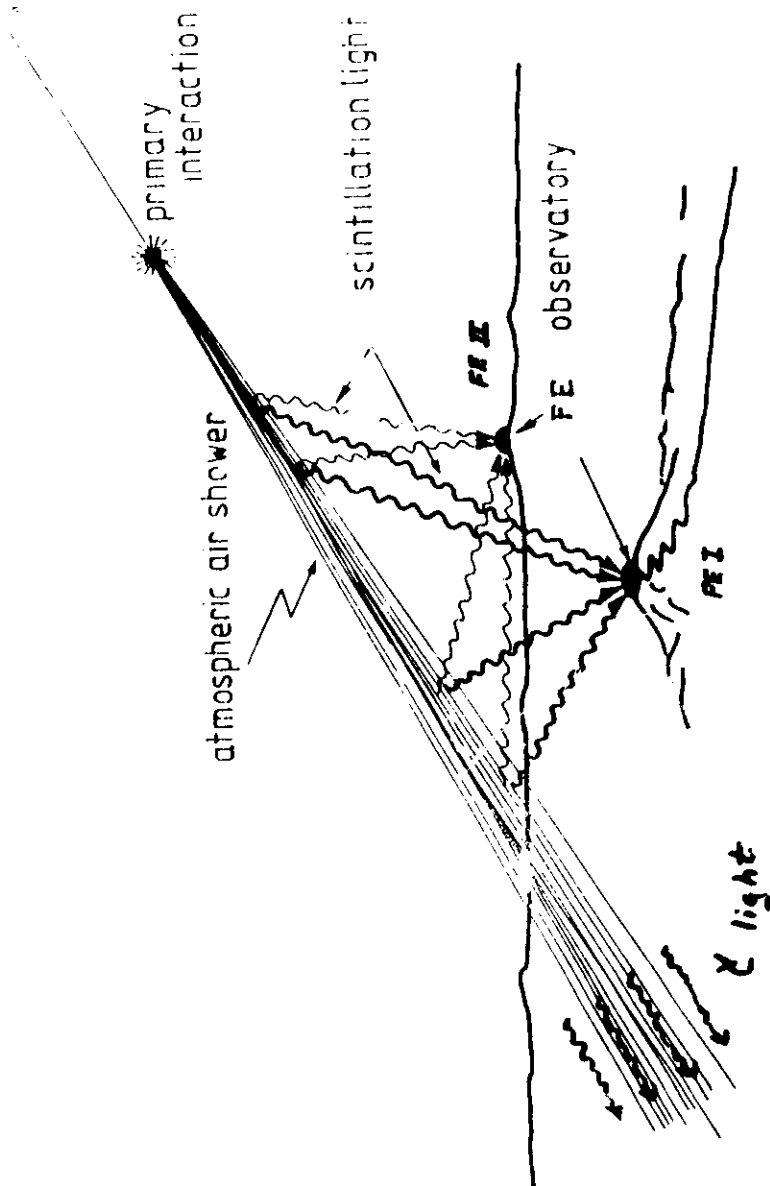


Fig. 53a Aerial view of the Fly's Eye I detector. The detector is located on top of Little Granite Mountain, elevation 860 g cm⁻², Dugway, Utah.

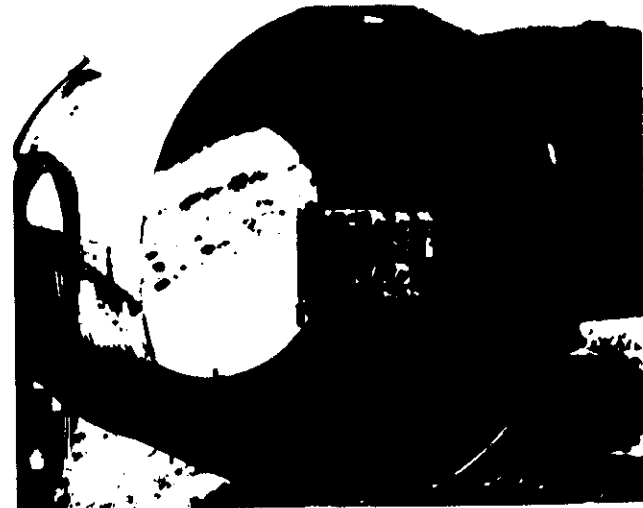
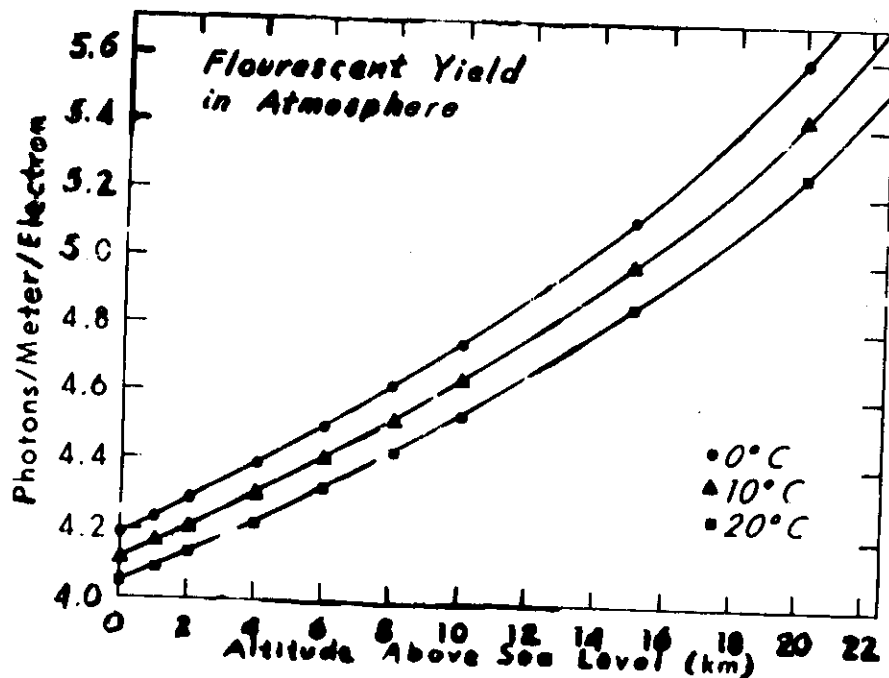
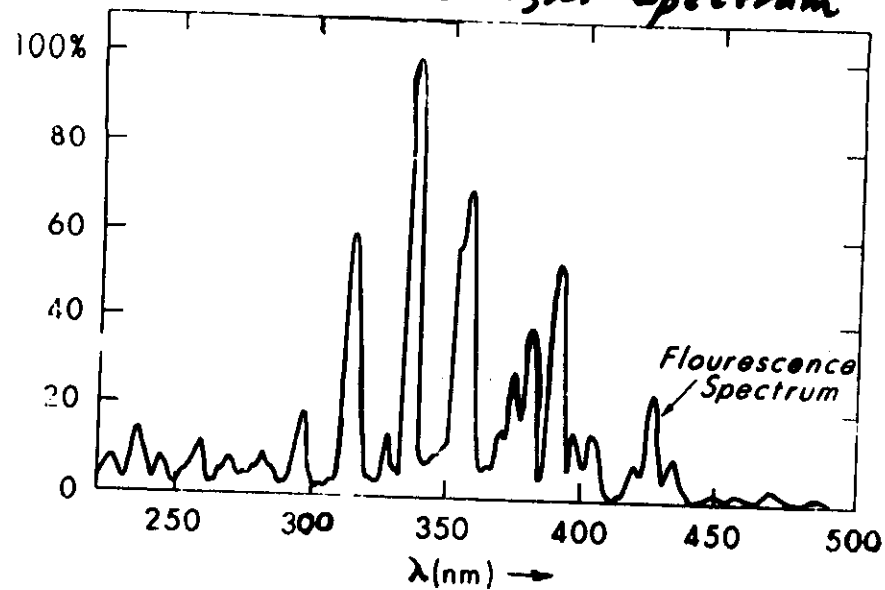


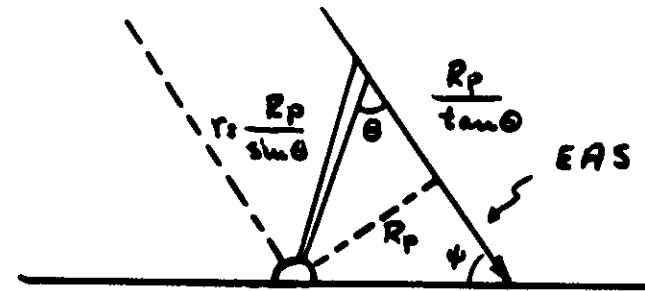
Fig. 53b

Scintillation Light Spectrum



93

Signal/Noise ... Again



- Signal - light generated in SL enters pmt where $SL: \delta\left(\frac{R_p}{\tan \theta}\right) = \frac{c \delta t (1 + \cos \theta)}{\sin^2 \theta}$

photons reaching detector

$$N_{ph} \approx \frac{N_e N_r SL A e^{-r/\lambda}}{4\pi r^2}$$

$$\approx N_e N_r \left(\frac{1 + \cos \theta}{\sin^2 \theta} \right) \frac{A}{4\pi r^2} e^{-r/\lambda} c \delta t$$

$$S = N_e N_r \left(\frac{1 + \cos \theta}{4\pi R_p^2} \right) e^{-r/\lambda} A c \delta t$$

- Noise $N \sim (4 \cdot B \cdot e_b \cdot A \cdot \Omega \cdot \delta t)^{1/2}$

- $S/N \sim E_s (A \cdot \delta t / e_b \Omega)^{1/2}$

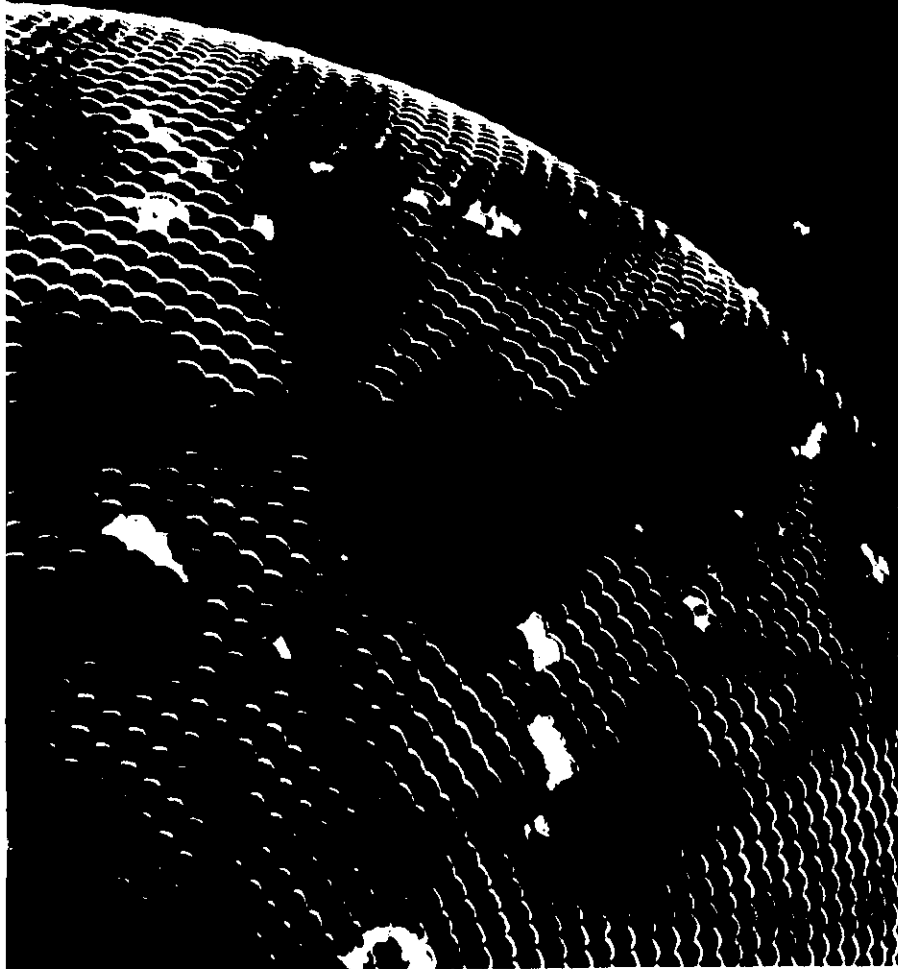
note $\delta t \sim \delta \theta$ and $\Omega \sim \pi \delta \theta^2$

$$S/N \sim E_s (A / e_b \cdot \delta \theta)^{1/2} \quad \text{but } N_{pmt} \sim \frac{1}{\Omega} \sim \frac{1}{\delta \theta^2}$$

$$S/N \sim \{E_s / (A / e_b)\}^{1/2} \cdot N_{pmt}^{1/4}$$

77

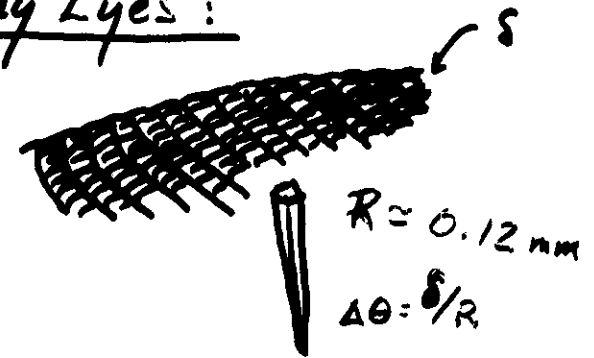
Eye of a housefly, 400 X



95

How Many Eyes?

96



$$N \approx \pi / \Delta\Omega$$

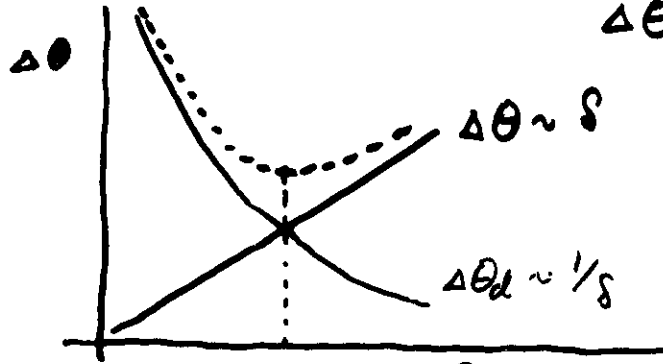
$$\Delta\Omega = \frac{\pi}{4} (\Delta\theta)^2$$

$$N = 4 / \Delta\theta^2$$

Resolution scales with s

But --- what about diffraction?

$$\Delta\theta_d \approx \lambda / s$$



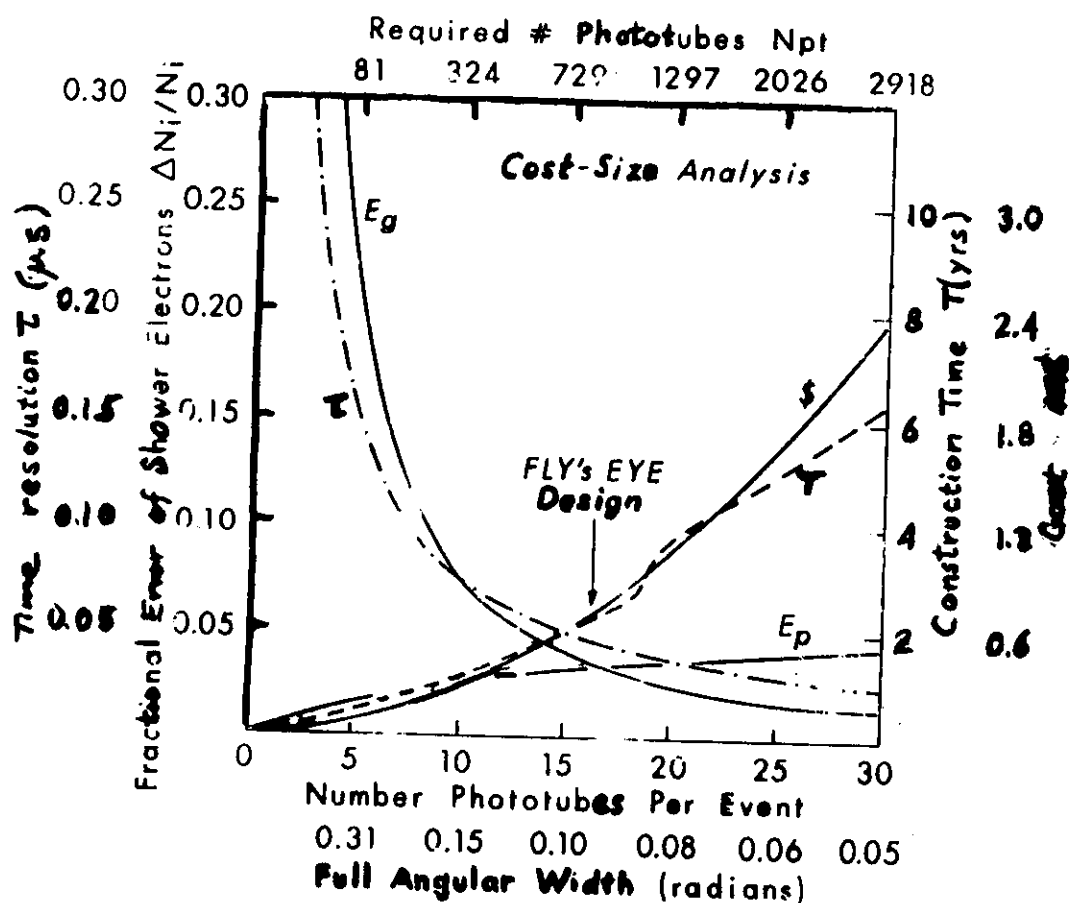
$$\lambda / s = s / R \quad \sim \quad s^2 = \lambda R \quad \Delta\theta^2 = \frac{s^2}{R^2}$$

$$\Delta\theta^2 = \lambda / R$$



$$N = 4R / \lambda = \boxed{1024}$$

Thought you might enjoy this - Gordy



Detector Characteristics

	FBI	II
# Mirrors	67	86
Diameter	1.575 m	
Focal Length	1.50 m	
# PMT (and Winston cones)	880	480
Mirror Obscuration	13%	
Mirror-cone ϵ	~ 70%	
PMT type	EMI 9861B Super 8-11	9793B bialkali
Peak Quantum ϵ at 360nm	20%	26%
Angular Aperture /pmt	91.5 mr	
Solid Angle /pmt	6.57 msr	
# Electronic Channels	2640	1440
Charge dynamic Range	2 - $2 \cdot 10^5$ pe	
Time Resolution	25 ns	

(The night sky is not benign!)

I. Major Problems

- Night sky light \Rightarrow DC background

$$B \times \in A \Delta \Omega \Delta t$$

Fluctuations in that background $\sim \sqrt{B}$

NOISE!

- Sun, Moon, Weather

E. Minor Irritants

Low energy junk ($E < 1 \text{ PeV}$)

Star, planets, milky way

Lightning, Auroras, satellites, glo-bugs

Airplanes, beacons, smokestack strobes

SLC, DPG, football stadium lites

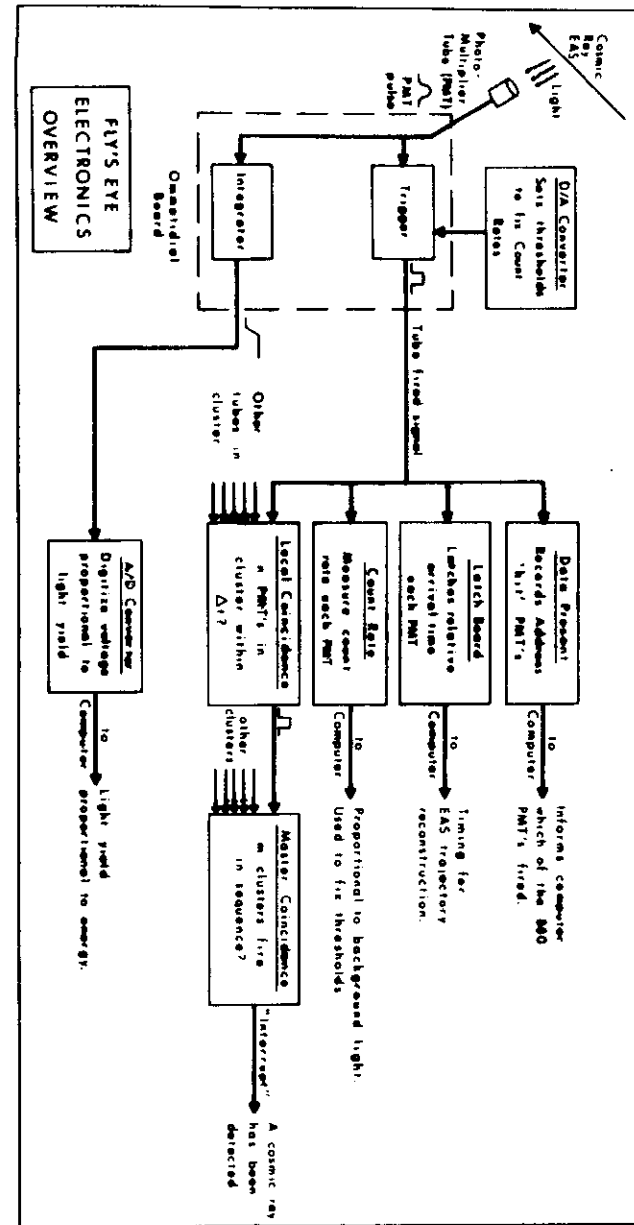
Nerve gas bunker lites

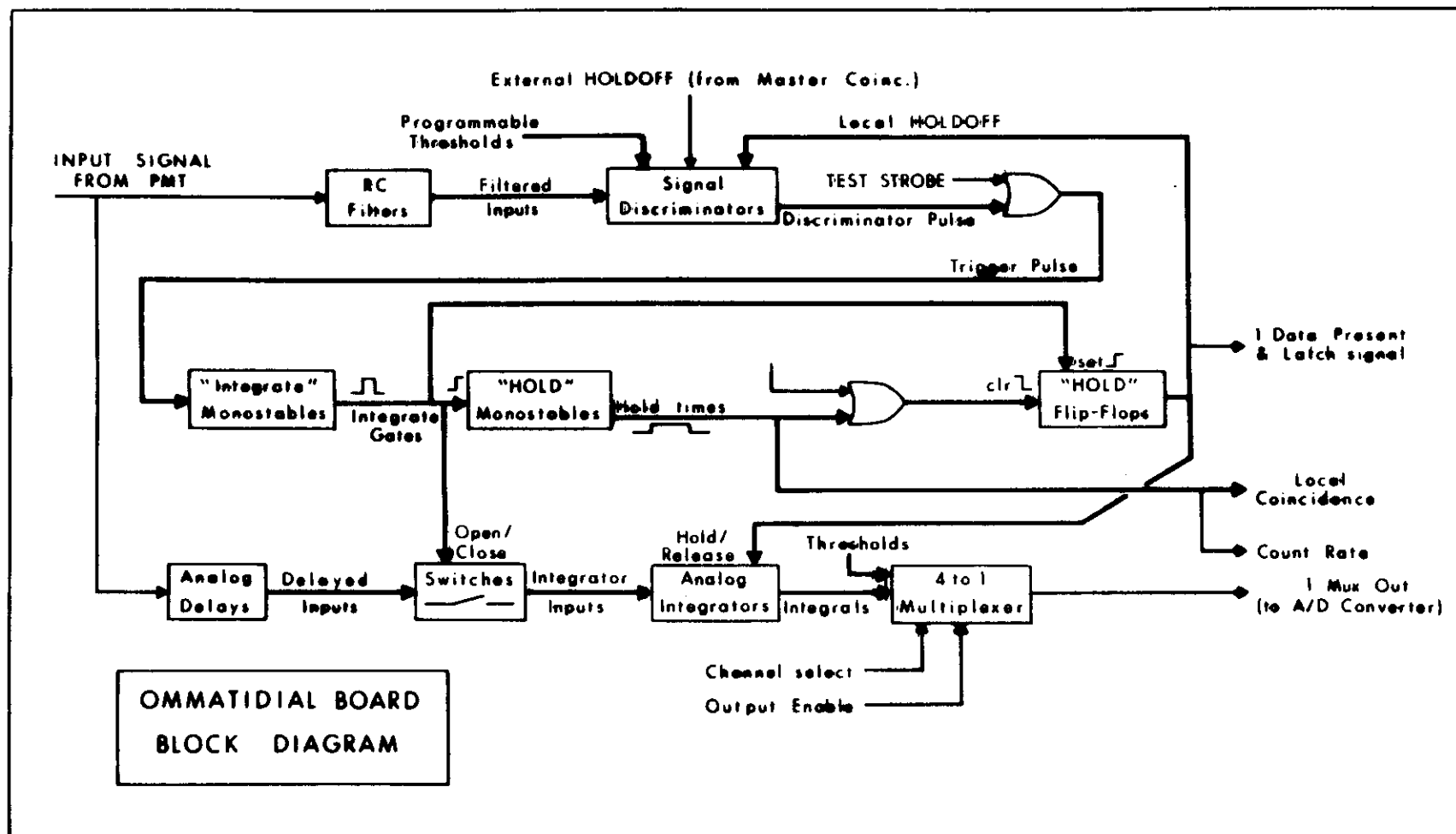
Meteors, Comets, re-entry satellites

II Sporadic (but catastrophic) Irritants

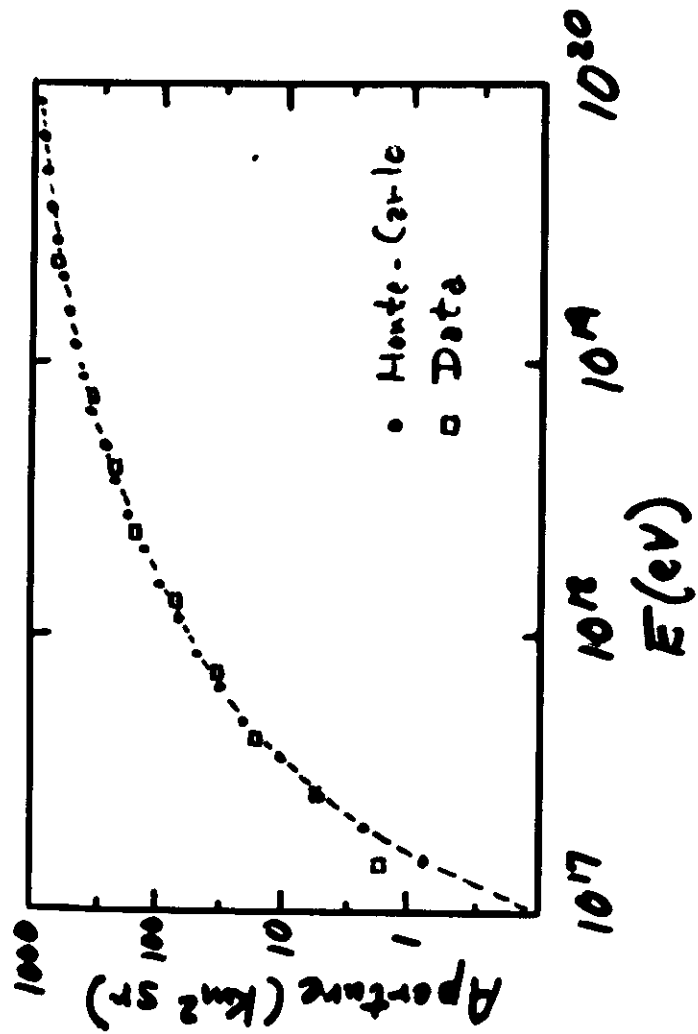
War games, helicopters, Tank traps

F-16¹⁵, Cruise Missiles





FLY'S EYE ACCEPTANCE



SHOWER GEOMETRY

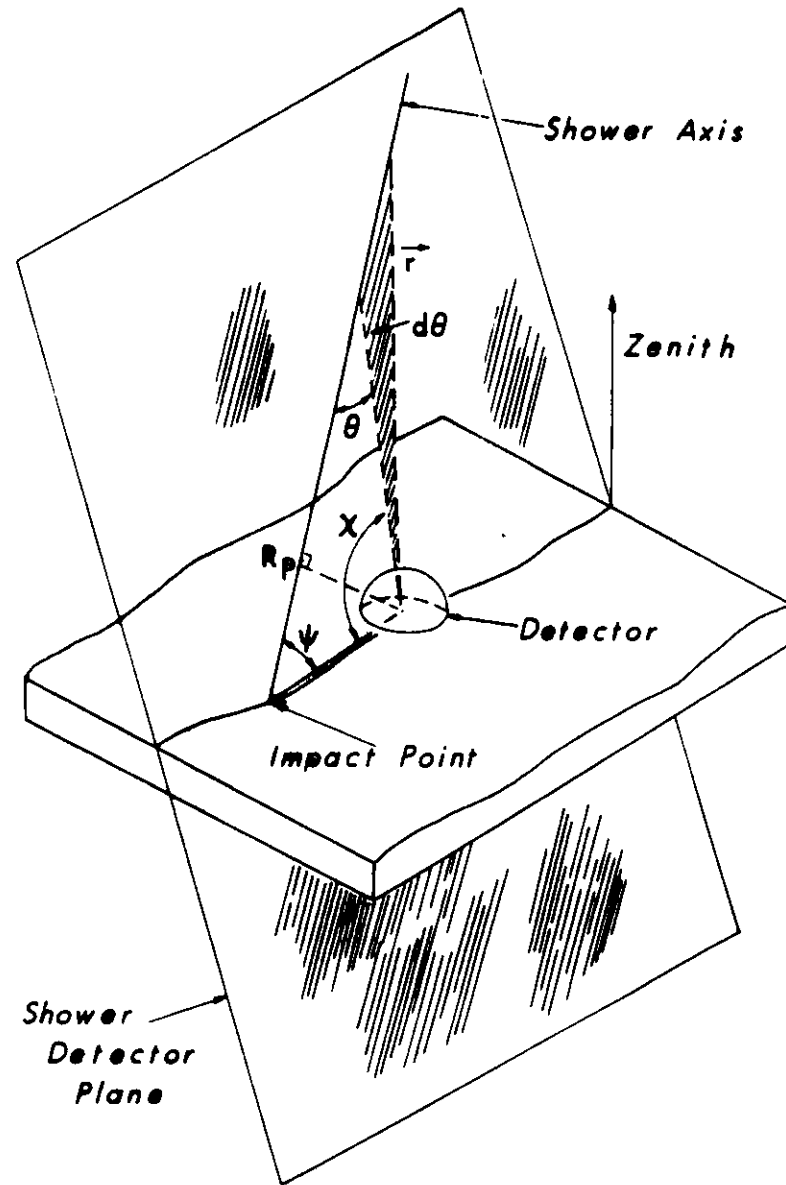
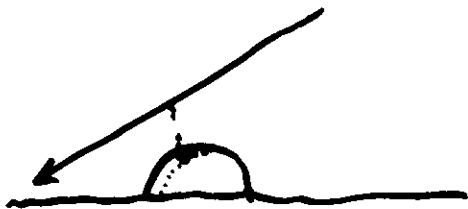
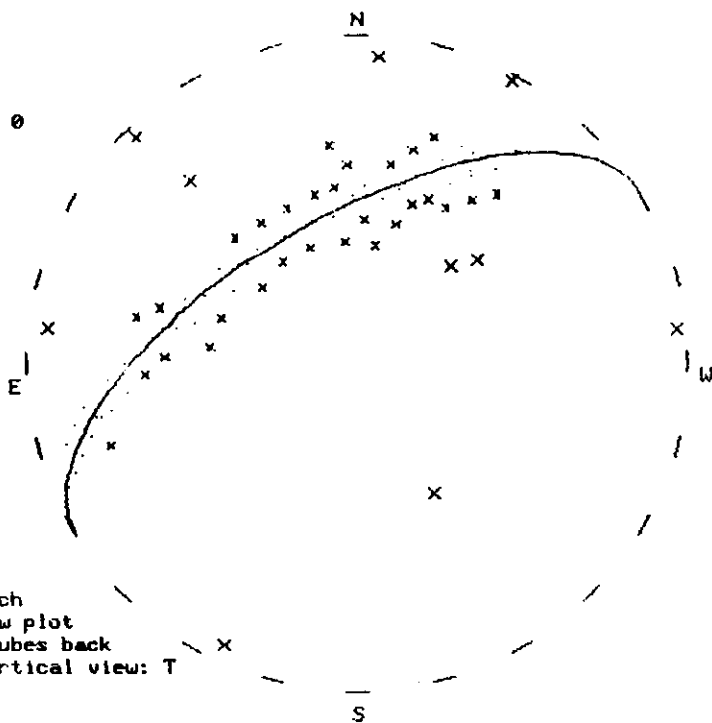


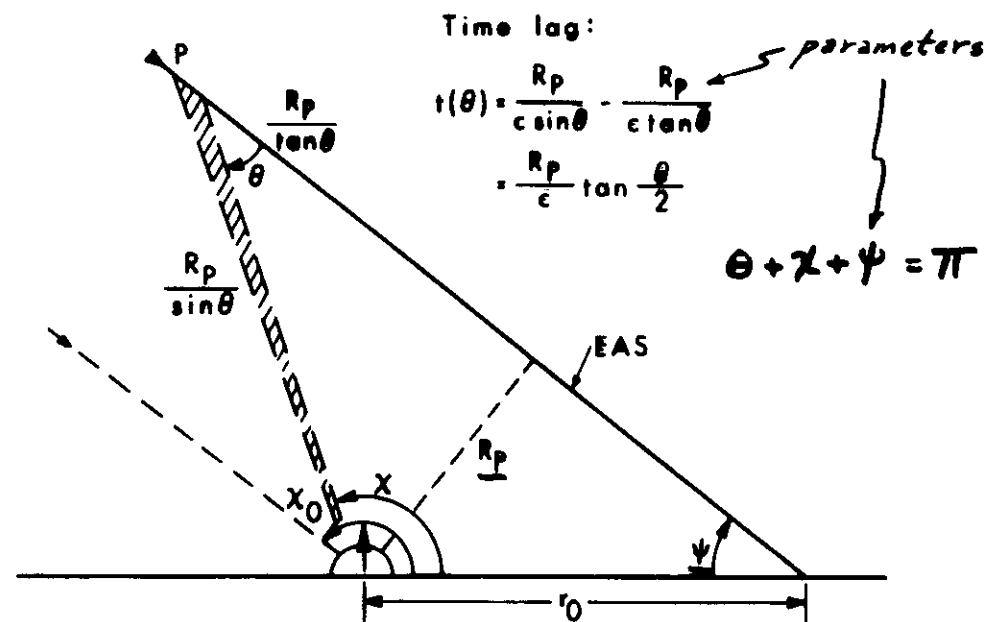
Fig. 55

FILE 4-22-1
EVENT 102
FEII TRIG STATUS= 0

M-Modify
T-Time fit
A-Accept event
R-Reject event
P-Print out/Chg latch
N/Q/S-Quick/Slow plot
U/B-Unslice/all tubes back
H/V-Horizontal/Vertical view: T

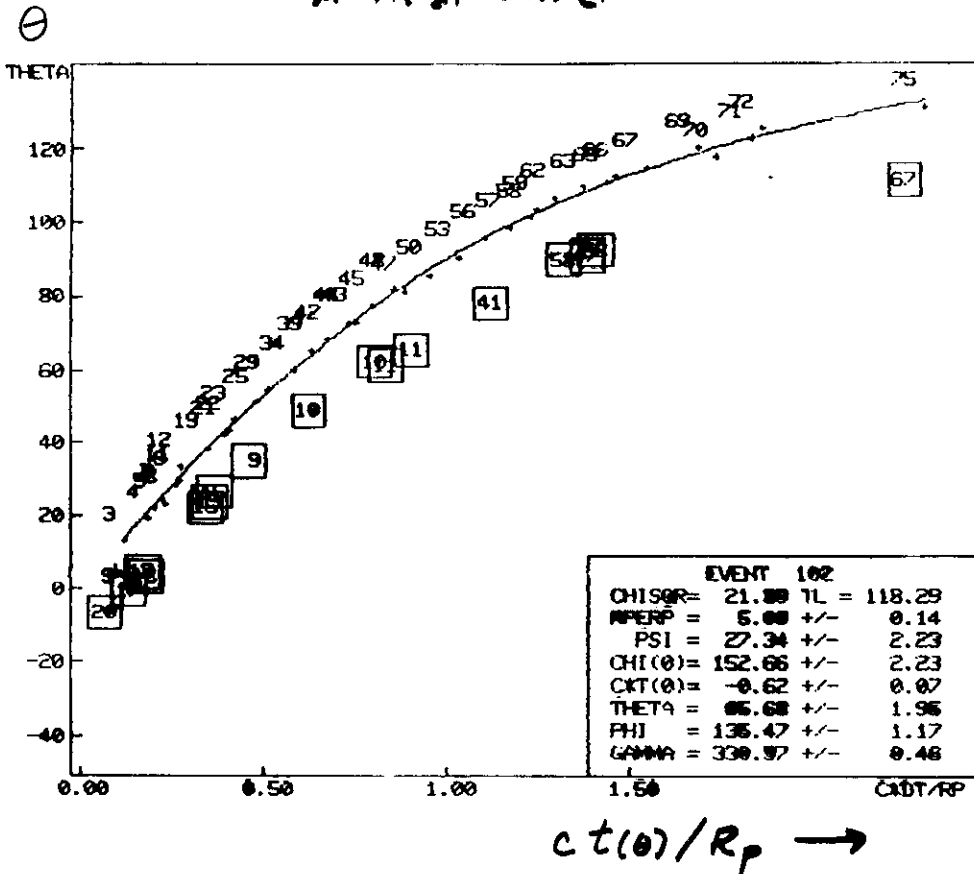


THE SHOWER DETECTOR PLANE



Emission Angle
vs
Arrival Time

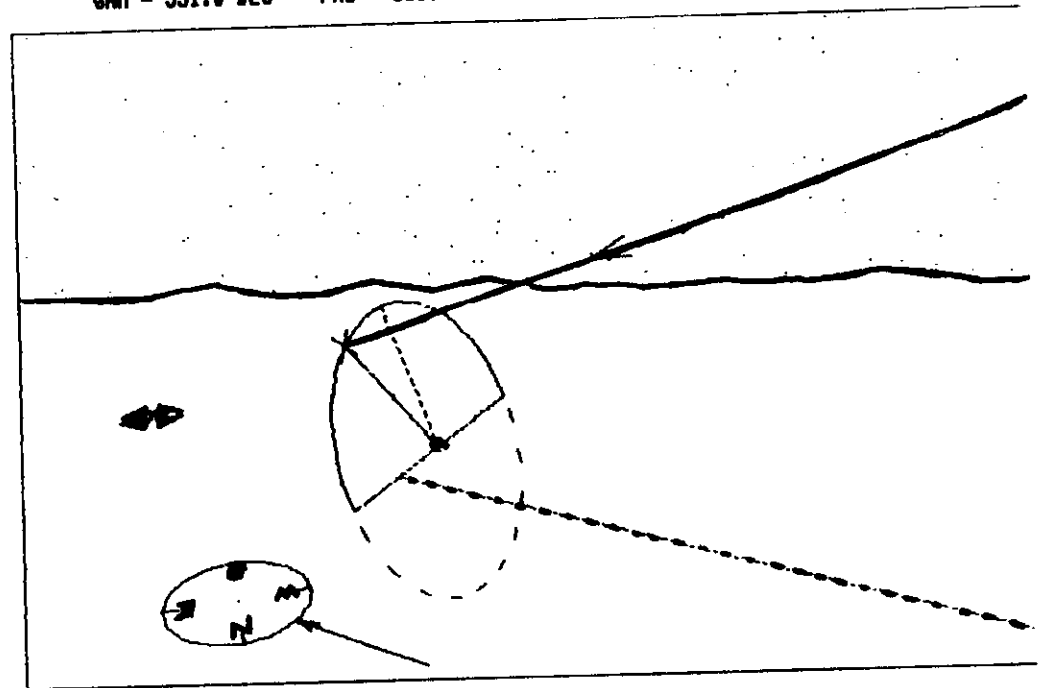
106



Event Coordinates

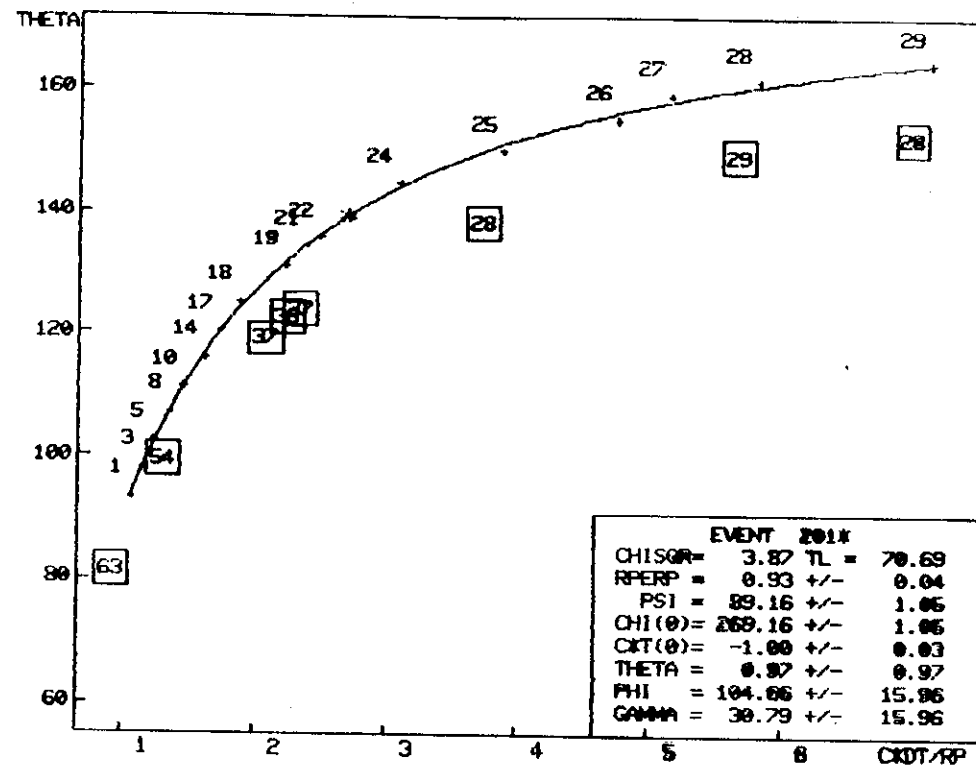
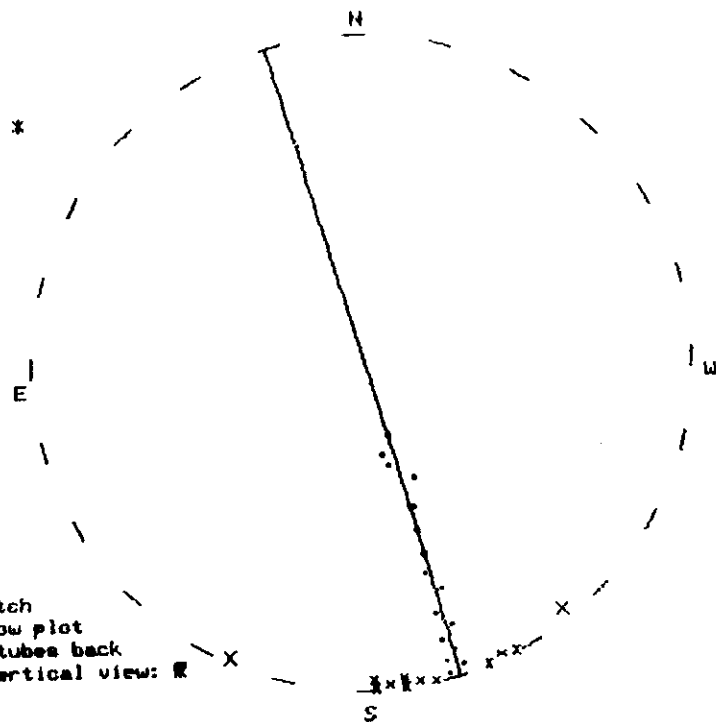
107

EVENT 4-22-1 (1982) # 102 TIME: 4/23/82 1:50: 9
 RP = 5.09 KM TME = 65.7 DEG RA = 0H 47M L = 170.5 DEG
 GAM = 331.0 DEG PHI = 135.5 DEG DEC = 49.1 DEG B = 39.3 DEG

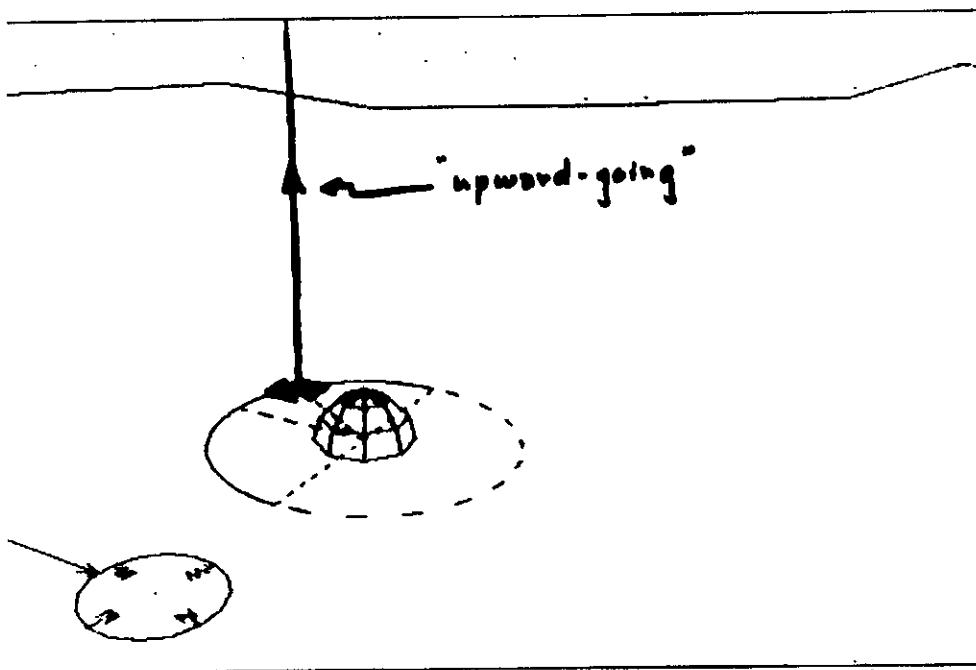


FILE 10-22-0
EVENT 201
FEII TRIG STATUS= *

M-Modify
T-Time fit
A-Accept event
R-Reject event
P-Prt evt/Chg latch
N/Q/S-S,Quick,Slow plot
U/B-Unslice,all tubes back
H/V-Horizontal,Vertical view: R



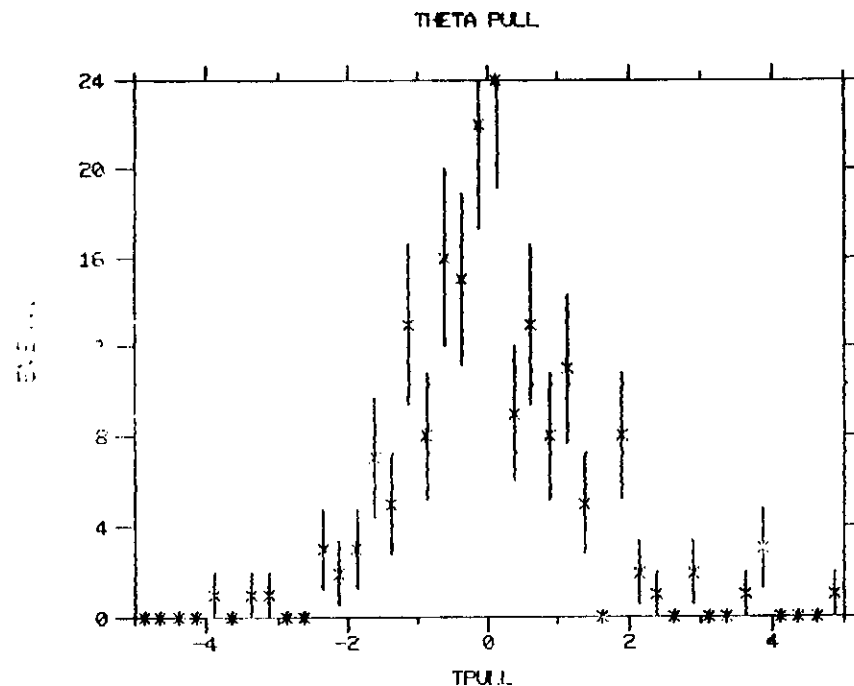
EVENT 10-22-0 (1982) # 201 TIME: 10/23/82 1:46:28
 RP = 0.93 KM THE = 1.0 DEG RA = 14H 17M L = 320.4 DEG
 CAM = 30.8 DEG PHI = 104.7 DEG DEC = -41.0 DEG B = 18.6 DEG



20 "fiducial" markers @ $\Delta\Phi = 18^\circ$
 20 vertical flashes @ hour
 trajectories reconstructed
 optical calibration from pulse heights
atmospheric monitor

Stereo
 vs
 Geo

ID= 17



***NDYPAK 16:07:06 19SEP84

$$T_{pull} = \frac{\delta(\theta)}{(\sigma_{Geo}^2 + \sigma_{Stereo}^2)^{1/2}}$$

$1\sigma \sim 2.5^\circ$

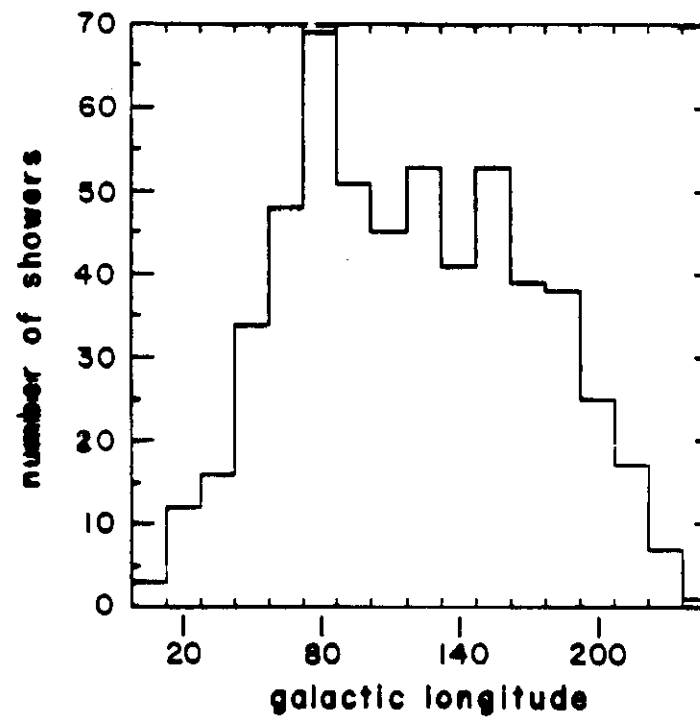
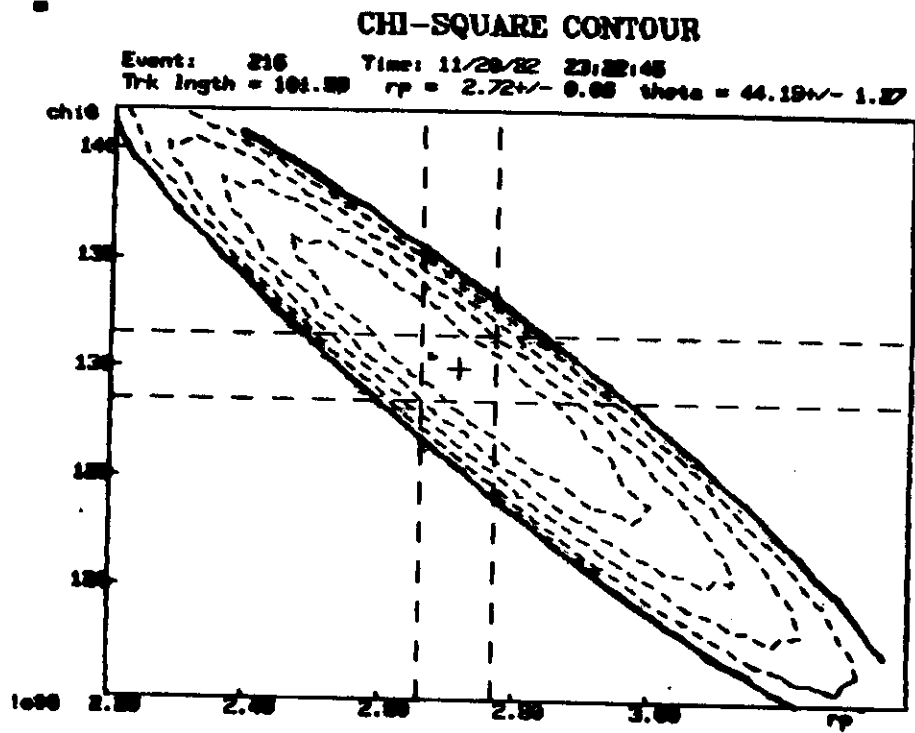
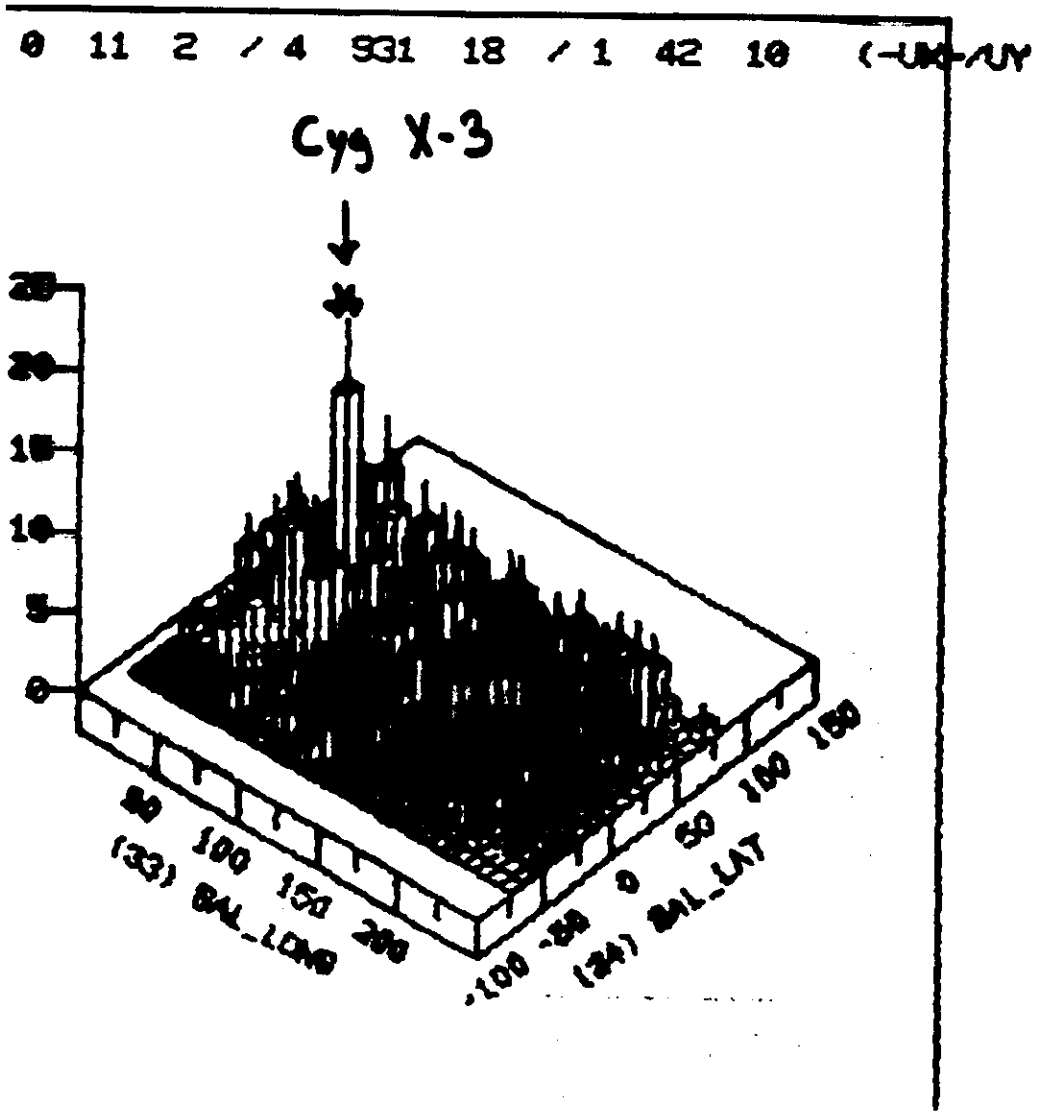


Figure 1

IN

112

SCATTER PLOT



SHOWER DENSITY FUNCTION

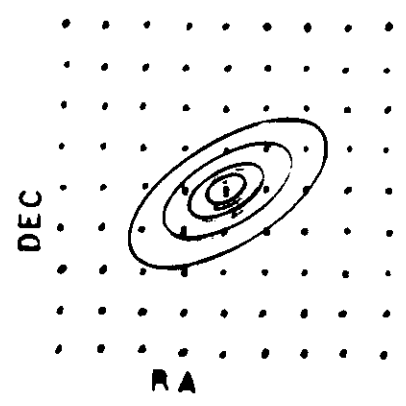
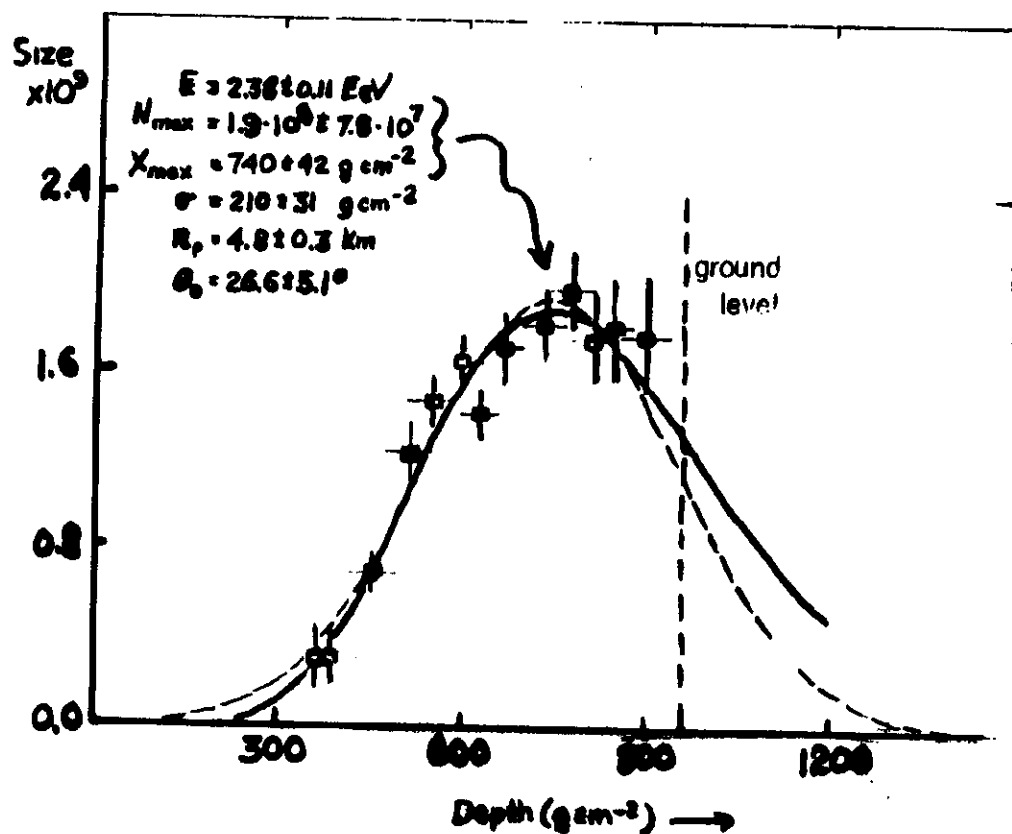


Fig. 61



Seen simultaneously by FEI and II

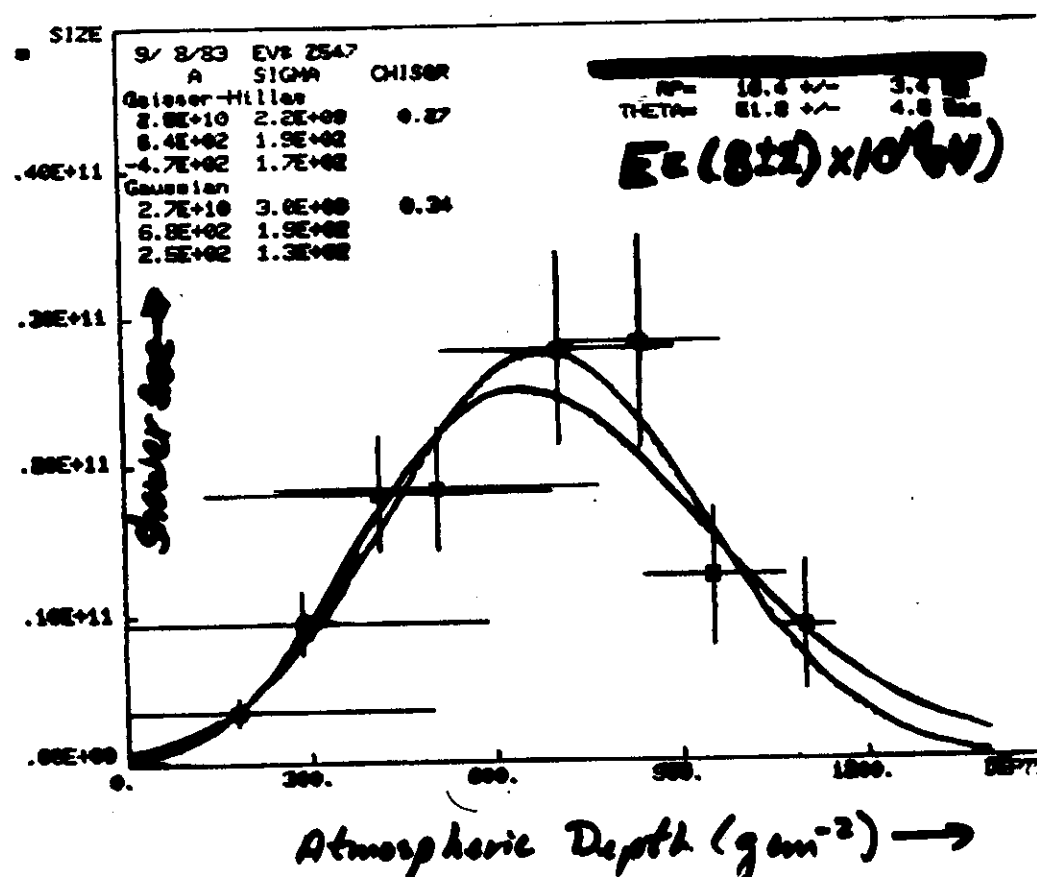
note: $E = \frac{E}{X_0} \int N_e(x) dx$ $\frac{E}{X_0} = 2.18 \text{ MeV/g cm}^{-2}$

(Dzhanukov - 1964)

Shower Size (N_e)

VS

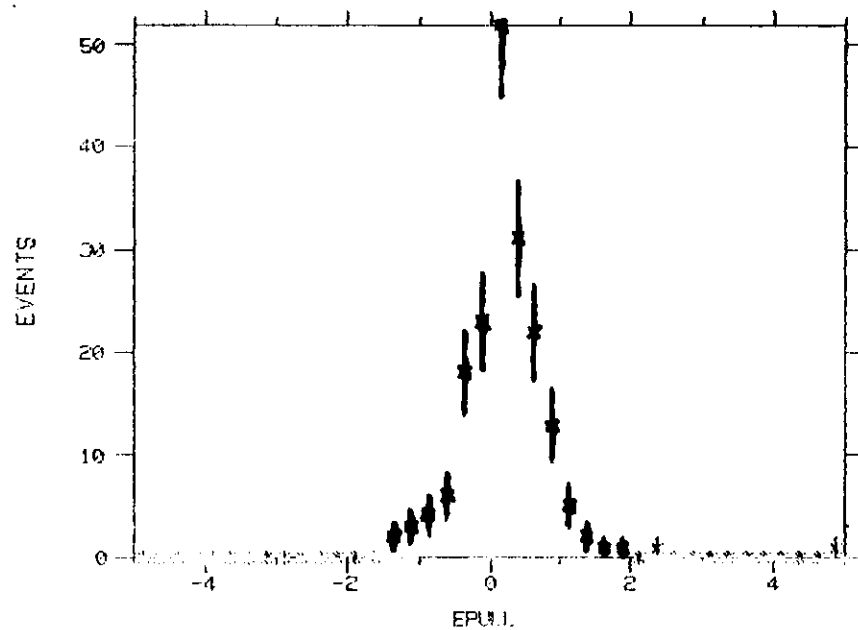
Atmospheric Slant Depth (g cm^{-2})



Stereo vs "Mono" Reconstruction

D= 33

Energy Pull



WDITYK 16:07:06 19SEP84

1σ-10%

$$E_{pull} = \frac{\delta E}{(\sigma_n^2 + \sigma_s^2)^{1/2}}$$

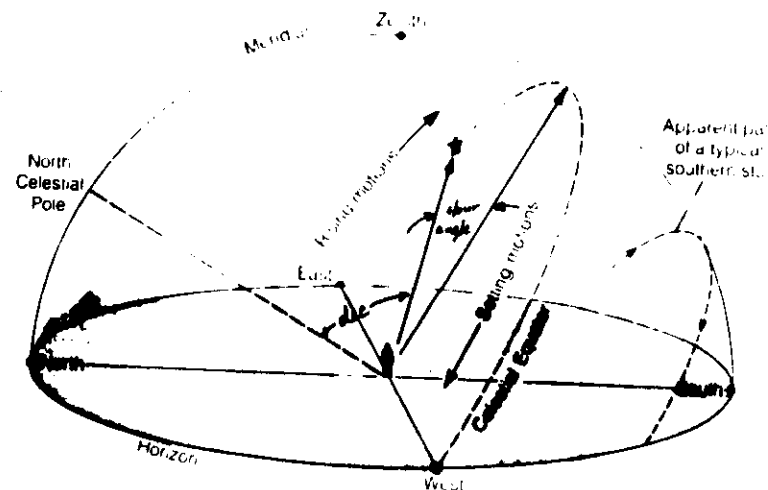
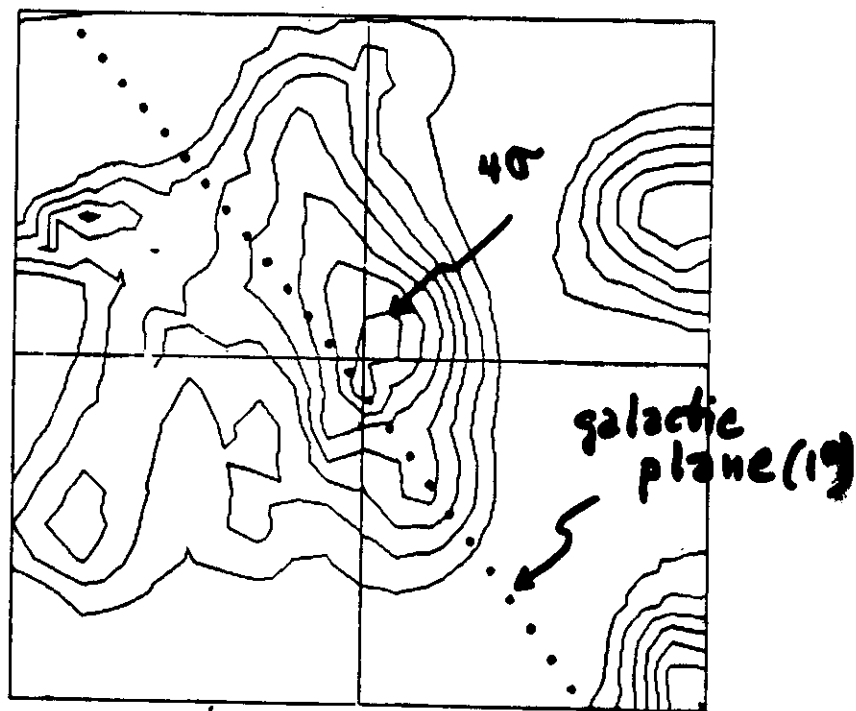


Figure 6.8 General properties of the sky as defined by the Earth's daily rotation. The sky is shown as seen by observers at midnorthern latitudes such as the United States.

Contour Map Cygnus X-3 on Center



20° x 20°

Figure 2

